

Diss. ETH No. 18162

Complexity Reduced Bearingless Pump Systems

A dissertation submitted to the
ETH ZURICH

for the degree of
DOCTOR OF SCIENCES

presented by
MARTIN THOMAS BARTHOLET
Dipl. El. Ing. ETH Zurich
born 26. January 1978
citizen of Flums, Switzerland

accepted on the recommendation of
Prof. Dr. Johann W. Kolar, examiner
Prof. Dr. Tore M. Undeland, co-examiner

2008

For Fabienne

For my parents

Acknowledgements

The following work evolved between 2005 and 2008 during my studies as a Ph.D. candidate at the Power Electronic Systems Laboratory at ETH Zurich and it would not have been possible without the support of various people to whom I would like express my sincere gratitude in the following.

A special thank you goes to my supervisor Prof. Dr. Johann W. Kolar for believing in my capabilities and offering me the possibility to work on this thesis. I also have to thank him for the support he gave and is still giving to the project that started after the Ph.D.

Special thanks go to Prof. Dr. Tore M. Undeland for co-referring this thesis and his interest in this work.

I am particularly grateful to Dr. Thomas Nussbaumer for never being too busy to explain things, for giving me feedback on my papers and for his guidance and the many useful discussions.

I was lucky to be able to work on my Ph.D. in a great research and social environment and would like to mention Klaus Raggl, who has shared the office with me during the Ph.D., Philipp Karutz, Thomas Schneeberger and Franz Zürcher for accompanying me during my time in the Technopark, Bernhard Warberger for helping me with the measurements and the whole team of Levitronix, especially Dr. Natale Barletta and Dr. Pascal Bösch, for their support and help.

Furthermore, Christof Zwysig also deserves many thanks for always having a helping hand and great ideas.

I am also indebted to Dr. Siegfried Silber from JKU Linz, Austria, for his contributions to the modeling of the motor topologies. I enjoyed each of my visits to Linz with the objective of gaining more in-depth

knowledge in the area of magnetic levitation.

I also wish to thank the Semester- and Master-Theses students who worked with me on various projects and are responsible for some of the content of this thesis.

Finally, I would like to thank Fabienne for her love and understanding when only a part of me was home while the rest was still at work. Without her, my dissertation would not have been possible. My whole-hearted gratitude also goes to my parents, who have unstintingly supported my education and constantly encouraged me, and last but not least to my godmother Elisabeth for her moral support.

Martin Bartholet

Abstract

In recent years, the bearingless slice motor pump has become well accepted in the semiconductor industry as well as for blood pumps in medical applications. Due to its unique design and the absence of mechanical friction and wear it has gained significant market share in these application areas. Following this development, new markets with higher cost pressure will be targeted in the upcoming years. To do so, the complexity of the overall system including the power electronics and the bearingless slice motor of a next generation bearingless pump system must be reduced and as a consequence of that it has to become economically more attractive. Thereby, the goal is to reduce the number of components and thus the volume of the configuration.

In this work, a novel inverter topology for the control of a two-phase bearingless slice motor pump. This topology has a reduced number of semiconductor devices compared to conventional topologies for bearingless slice motors.

In **chapter 1** a short introduction on magnetic bearing technology in general and more specifically on the bearingless slice motor concept is given. Also, the market potential for complexity reduced next generation bearingless pump systems is shown in this chapter along with the specific requirements arising in the different markets.

Chapter 2 deals with the topology selection for the control of the two-phase bearingless slice motor with the aim of reducing the number of semiconductor switches. Based on this analysis the current and voltage stresses of the semiconductors in the chosen topology are evaluated. Furthermore, an integrated power module is analysed and with the thereby obtained switching loss data the design and thermal analysis of the heat

sink is accomplished.

A major cost driver in today's bearingless pump systems are the sensors for the measurement of the drive and bearing currents. In **chapter 3** an alternative concept is investigated which employs current sensors with lower bandwidth at an economically more attractive price. The influence of the lower bandwidth along with the delay times in the system on the current control is analysed in this chapter. Based on that, the selection of the switching frequencies for the power semiconductors is shown.

In **chapter 4** different modulation methods and their applicability for the control of the two-phase bearingless slice motor pump are derived in order to achieve full performance when employing today's pumps with the novel converter topology. Furthermore, an analysis of the maximum achievable phase voltage as well as drive power based on the applied modulation scheme is carried out. In addition to that, investigations are carried out whether the higher harmonics in the drive current influence the stable operation of the pump or not.

In order to attract new markets, not only the power electronics but also alternative concepts of the bearingless slice motor itself must be taken into consideration. Thus, in a comprehensive comparison five slice-motor configurations are comparatively evaluated to each other in conjunction with the presented power electronics converter in **chapter 5**. The analysis is carried out based on the losses arising in each system, the power electronics requirements, manufacturability and hardware effort.

The influence on the size of the input filter in the case that long power cables are used for the connection of the converter and the bearingless slice motor is analysed in **chapter 6**. The design of the common mode input filter is shown based on a model of the common mode noise emission of the slice motor pump system. The input filter is designed so that it ensures full compliance with the standards concerning common mode and differential mode conducted emissions. It is shown that a volume optimised filter design can be performed based on this model.

Finally, in **chapter 7** the experimental analysis of the system is carried out on a laboratory prototype of the investigated power electronics converter. The modulation methods shown in chapter 4 are implemented on a digital signal processor and their feasibility is verified with a bearingless pump. It is shown that the presented modulation methods allow full performance of the bearingless pump system.

Kurzfassung

In den letzten Jahren wurden lagerlose Scheibenläufermotoren immer häufiger zum Pumpen von Prozessflüssigkeiten in der Halbleiterindustrie, wie auch als Blutpumpen in der Medizinaltechnik eingesetzt. Vor allem der reibungsfreie Betrieb, der keine Partikelbildung verursacht, ist eine herausragende Eigenschaft des lagerlosen Pumpenkonzeptes, welches zu einer stetigen Vergrößerung des Marktanteils in den genannten Gebieten geführt hat.

Damit in den kommenden Jahren auch Märkte mit einem erhöhten Kostendruck erschlossen werden können, ist es notwendig die Gesamtkomplexität bestehender Systeme, einschliesslich der Leistungselektronik und dem lagerlosen Motor zu reduzieren, um ein betreffend Material- und Herstellungskosten attraktiveres System realisieren zu können. Das Ziel dabei ist es, die Anzahl der Komponenten zu reduzieren, um damit ein geringeres Volumen des Systems zu erhalten.

Der Hauptfokus dieser Arbeit liegt auf einer neuartigen Schaltungstopologie für den Betrieb zweiphasiger lagerloser Scheibenläuferpumpen. Diese Topologie weist im Vergleich zur herkömmlichen Variante eine verminderte Anzahl von Leistungshalbleitern auf.

Nach einer kurzen Einführung in die Theorie der Magnetlagertechnik wird in **Kapitel 1** spezifisch auf die Topologie der lagerlosen Scheibenläuferpumpe eingegangen. Im weiteren Verlauf wird dann das Marktpotenzial für zukünftige volumen- und kostenoptimierte Pumpsysteme in Verbindung mit den spezifischen Anforderungen in den jeweiligen Märkten gezeigt.

Kapitel 2 beinhaltet die Untersuchung möglicher Konvertertopologien mit einer reduzierten Anzahl von Halbleiterelementen für den Be-

trieb zweiphaser lagerloser Motoren. Basierend auf dieser Analyse erfolgt anschliessend die Untersuchung der Strom- und Spannungsbelastungen der einzelnen Leistungshalbleiter. Als Grundlage zur Ermittlung der Schalt- und Leitverluste im System wird das gewählte Halbleitermodul nachfolgend mit Hilfe von Schaltverlustmessungen analysiert. Im Anschluss daran wird basierend auf diesen Verlustbetrachtungen die Auslegung und Verifikation des Kühlkörpers gezeigt.

Ein grosses Potential zur Kostenreduktion heutiger Systeme liegt im Bereich der Stromsensoren zur Erfassung der Lager- und Antriebsströme. Auf diese Thematik wird im **Kapitel 3** mit der Untersuchung eines alternativen Strommesskonzeptes eingegangen. Hierzu wird der Einfluss der verringerten Messbandbreite dieser alternativen Stromsensoren und die zusätzlich auftretenden Verzögerungszeiten auf die Stabilität der Regelung analysiert. Basierend auf diesen Überlegungen werden die Schaltfrequenzen der Leistungshalbleiter definiert.

Im **Kapitel 4** werden verschiedene Modulationsverfahren hergeleitet die es ermöglichen, die Leistungsfähigkeit der lagerlosen Pumpe beim Betrieb mit der in dieser Arbeit vorgestellten Leistungselektronik zu steigern. Weiter wird die Analyse der maximal zur Verfügung stehenden Klemmenspannung und der damit verbundenen Antriebsleitung in Abhängigkeit des gewählten Modulationsverfahrens gezeigt. Anschliessend wird der Einfluss höherer Stromharmonischer auf das Betriebsverhalten der Pumpe untersucht.

Damit mit dem Konzept der lagerlosen Pumpe neue Märkte erschlossen werden können, müssen neben der Leistungselektronik auch die Möglichkeiten der Komplexitätsreduktion des Scheibenläufermotors an sich untersucht werden. Im **Kapitel 5** wird eine Analyse von fünf möglichen Motorkonzepten durchgeführt. Die Topologien werden dabei hinsichtlich der Verluste im Motor und der Leistungselektronik, der erreichbaren Drehzahl des Motors, den Anforderungen an die Leistungselektronik betreffend maximal benötigter Spannung bzw. Strom, sowie dem Materialaufwand, Herstellbarkeit und Anwendbarkeit in spezifischen Anwendungsgebieten untersucht.

Der Einfluss der Länge des Leistungskabels zwischen dem Motor und der Leistungselektronik auf die Dimensionierung des Eingangsfilters wird in **Kapitel 6** untersucht. Basierend auf einem Gleichtaktstörmodell des leistungselektronischen Systems wird ein Eingangsfiler entworfen, welches die Einhaltung der Vorschriften bezüglich der leitungsgebundenen Gleich-

und Gegentaktstöraussendung im Bereich 150 kHz bis 30 MHz sicherstellt. Es wird gezeigt, dass basierend auf diesem Modell ein volumenoptimiertes Eingangsfiler ausgelegt werden kann.

Abschliessend wird in **Kapitel 7** die Realisierung eines hochkompakten Hardware-Prototypen des Systems gezeigt. Die Implementierung der in Kapitel 4 gezeigten Modulationsverfahren erfolgt auf einem digitalen Signalprozessor. Es wird gezeigt, dass mit Hilfe dieser Verfahren die volle Leistungsfähigkeit zweiphasiger lagerloser Pumpen erreicht werden kann.

Notation

Symbols

A	surface area
A_{Cu}	copper wire cross area
B	flux density
B_i	bearing phase
B_{PM}	permanent magnet flux density
C_{dc}	dc-link capacitor
d	impeller diameter
d_{Fe}	thickness of iron sheets
D_k	diode
D_i	drive phase
f_e	electrical frequency
f_m	mechanical frequency
E_{off}	turn-off loss energy
E_{on}	turn-on loss energy
E_{rr}	reverse recovery loss energy
E_{Sw}	switching loss energy
f_c	cut-off frequency
f_I	interrupt frequency
F_{res}	resulting force
F_r	force acting on the rotor
f_s	switching frequency
F_s	force acting on the rotor by the stator field

H	magnetic field intensity
I_{avg}	average current
i_{CB}	current in the common bridge-leg
i_d	control current
i_{in}	input current of a power module
I_L	inductor current
I_{rms}	rms current
i_{rr}	reverse recovery current
J_s	current density distribution on the stator surface
k_F	force-current constant
k_M	current-torque constant
k_p	proportional gain
$k_{R,B}$	radial bearing stiffness
$k_{U,ind}$	drive winding constant
$k_{0,k}, k_{1,k}, k_{2,k}$	switching loss coefficients
k_1	linear loss factor
k_2	square loss factor
L_c	cable inductance
L_m	motor inductance
L	inductor
l_w	average winding length
l_r	rotor length
m	number of phases
m_{Fe}	iron mass
m_I	impeller mass
M	modulation index
n	rotor speed
T_r	torque acting on the rotor
T_s	torque acting on the stator
t_{sample}	sampling time
n_c	number of coils per phase
N	number of windings
N_P	neutral point

p	number of pole pairs
P_{Cu}	copper losses
P_D	drive power
P_{DR}	rated drive power
P_e	electrical power
P_{Ed}	eddy current losses
P_{Fe}	iron losses
P_{Hy}	hysteresis losses
$P_{L,B,tot}$	total losses in the bearing module
$P_{L,D,tot}$	total losses in the drive module
P_m	mechanical power
P_{Fw}	forward losses
P_{PE}	power electronics losses
P_{Sw}	switching losses
$P_{Sw,off}$	turn-off switching losses
$P_{Sw,on}$	turn-on switching losses
P_{hydr}	hydraulic power
p_1	number of pole pairs drive system
p_2	number of pole pairs bearing system
Q	output flow of centrifugal pump
R	resistor
R_c	cable resistance
R_m	motor resistance
$R_{th,J-C,IGBT}$	thermal resistance per IGBT
$R_{th,J-C,Diode}$	thermal resistance per Diode
$R_{th,C-HS}$	thermal resistance module case – heat sink
r_r	rotor radius
T	torque
T_A	ambient temperature
τ_M	mechanical time constant
τ_E	electrical time constant
τ_{CS}	rise time current sensor
T_{HS}	heat sink temperature
T_k	transistor

T_I	interrupt time
T_J	junction temperature
T_M	maxwell stress tensor
T_P	pulse interval
t_μ	pulse interval
T_{offset}	temperature offset
T_R	rated torque
t_{rise}	rise time
\bar{u}	average voltage
u_{CE}	collector–emitter voltage
u_{CM}	common–mode voltage
$U_{cl,max}$	maximum clamp voltage at the drive or bearing phase
U_{dc}	dc–link voltage
$U_{max,SC}$	maximum output voltage of the SC-topology
U_{ind}	induced voltage
u_L	voltage across an inductor
u_{tri}	triangular voltage signal
Y	output pressure of centrifugal pump
α	rotor angle
δ	duty cycle
λ_{Cu}	specific resistance of copper
μ	permeability
ξ	winding factor
φ	phase angle
Φ_{PM}	magnetising flux

Abbreviations

<i>AUX</i>	Auxiliary Task Controller Software Routine
<i>BNG</i>	Bearing Controller Software Routine
<i>BSM</i>	Bearingless Slice Motor
<i>BW</i>	Bandwidth
<i>CB</i>	Common Bridge

<i>CBL</i>	Common Bridge–Leg
<i>CC</i>	Current Controller
<i>CS</i>	Current Sensor
<i>CCM</i>	Constant Common Bridge–Leg Modulation
<i>CM</i>	Common Mode
<i>DM</i>	Differential Mode
<i>DRV</i>	Drive Controller Software Routine
<i>EMC</i>	Electromagnetic Compatibility
<i>EMF</i>	Electromagnetic Force
<i>EUT</i>	Equipment Under Test
<i>FB</i>	Full–Bridge
<i>FBM</i>	Full–Bridge Modulation
<i>HS</i>	Heat Sink
<i>IGBT</i>	Insulated Gate Bipolar Transistor
<i>IHB</i>	Interleaved Half–Bridge Topology
<i>LISN</i>	Line Impedance Stabilisation Network
<i>LVAD</i>	Left Ventricular Assist Device
<i>MTTF</i>	Mean Time to Failure
<i>PM</i>	Permanent Magnet
<i>RPM</i>	Speed Controller Software Routine
<i>SCM</i>	Sinusoidal Common Bridge–Leg Modulation
<i>THM</i>	Third Harmonic Modulation
<i>TQM</i>	Third Harmonic and Square Common Bridge– Leg Modulation
<i>QCM</i>	Square Common Bridge–Leg Modulation
<i>SBL</i>	Separate Bridge–Leg
<i>SC</i>	Split–Capacitor Topology
<i>VA</i>	Volt Ampere requirement

Contents

Acknowledgements	i
Abstract	v
Notation	ix
1 Introduction	1
1.1 Motivation	2
1.1.1 State-of-the-art Bearingless Slice Motor Pump . .	2
1.1.2 Principle of Magnetic Levitation	6
1.1.3 Challenges for Next Generation Bearingless Pump Systems	8
1.1.4 Cost Reduction Approach	13
2 Power Electronics	17
2.1 Introduction	17
2.2 Inverter Topology Selection	17
2.2.1 Full-Bridge Topology	18
2.2.2 Split-Capacitor Topology	19
2.2.3 Interleaved Half-Bridge Topology	21
2.2.4 Comparison of the Topologies	22
2.3 Inverter Design	24
2.3.1 Semiconductor Stresses	25

2.3.2	Power Module IRAM136-3063B	30
2.3.3	Switching Loss Measurements	31
2.3.4	Calculation of the Losses in the Power Module . .	34
2.3.5	Loss Distribution	38
2.3.6	Thermal Analysis	41
2.3.7	DC-Link Capacitor	45
2.4	Summary	47
3	Sensor and Control System	49
3.1	Introduction	49
3.2	Current Sensor	49
3.3	Drive System	51
3.4	Bearing System	54
3.5	Software	61
4	Modulation Methods	65
4.1	Introduction	65
4.2	Constant Common Bridge Leg Modulation (CCM)	67
4.3	Sinusoidal Common Bridge Leg Modulation (SCM)	69
4.4	Harmonic Injection	71
4.4.1	Third Harmonic Modulation (THM)	72
4.4.2	Square Common Bridge Leg Modulation (QCM) .	74
4.4.3	Third Harmonic and Square Common Bridge Leg Modulation (TQM)	75
4.5	Comparison	77
4.5.1	Fundamental Drive Voltage	78
4.5.2	Maximum Achievable Drive Power	80
4.5.3	Variation of Drive Windings	82
4.5.4	Summary	84
5	Motor Configurations	85
5.1	Force and Torque Calculation	86

5.2	Investigated Configurations	90
5.2.1	Two-Phase Motor Configuration (a)	91
5.2.2	Three-Phase Pitched Drive Configuration (b) . . .	92
5.2.3	Three-Phase Concentrated Drive Configuration (c)	95
5.2.4	Three-Phase Pitch Winding Configuration (d) . .	97
5.2.5	Four-Phase Combined Configuration (e)	100
5.3	Comparison	101
5.3.1	Loss Calculations	102
5.3.2	Losses in the Power Electronics	106
5.3.3	Loss Distribution in Bearingless Motor System . .	108
5.3.4	Power Electronics Requirements	108
5.3.5	Cost Related Factors	112
5.4	Summary	115
6	Conducted Emissions	117
6.1	Introduction	117
6.2	Line Impedance Stabilisation Network	119
6.3	DM Filter Design	120
6.4	CM Filter Design	121
6.4.1	Modeling of the Inverter	121
6.4.2	Estimation of Model Parameters	121
6.4.3	Modeling of Motor Cable	123
6.4.4	Modeling of Bearingless Slice Motor	126
6.4.5	Modeling of CM Source	127
6.5	Filter Design	130
7	Realisation and Results	135
7.1	Power Electronics	135
7.1.1	DSP Board	135
7.1.2	Power Stage	136
7.1.3	Efficiency	137

7.1.4	Verification of Modulation Methods	138
	Conclusion	139
	Outlook	144
	Bibliography	146
	Curriculum Vitæ	157

Chapter 1

Introduction

This chapter addresses the research field in which this work is inserted and gives an overview about the motivation of this work. In recent years, bearingless slice motor (BSM) pumps have become well accepted in the semiconductor industry as well as for medical applications. The therein employed temple motor design provides a means of levitating an impeller completely without any physical contact. Due to its unique design and absence of mechanical friction and wear this motor concept has gained significant market share in the area of the delivery of process fluids in the semiconductor industry as well as in medical applications. There it is used specifically as a Left Ventricular Assist Device (LVAD) to assist a weak heart during the time until the heart transplantation can take place (bridge to transplant).

This introduction chapter does not enter deeply into the theory of magnetic bearing technology. The purpose of the following sections within this chapter is to give an overview of the magnetic levitation technology to the reader and to briefly outline the achievements gained in the area of the bearingless slice motor so far. The subsequent chapters of this theses along with the referenced literature will then provide the reader a more detailed insight into the topic of bearingless slice motors.

1.1 Motivation

Currently, the main application fields for bearingless slice motors lie in centrifugal pumps in the medical and semiconductor industry, where on the one hand high requirements for purity and reliability must be met and on the other hand system prices are not of major priority. However, a similar trend as for automotive applications, where highly cost competitive designs are demanded, is expected to arise in the area of bearingless pumps in the near future, where new markets are currently targeted. In order to be competitive in these markets, bearingless pump systems must become economically more attractive. This mainly means that the volume of the power electronics must be reduced significantly. But not only this, also the motor concept itself has to be taken into consideration regarding the required number of components for a stable operation of the impeller and the thereby arising potential for a complexity reduction. Trends in the semiconductor industry indicate that relatively long distances of up to 30 m between the controller (including the power electronics) and the motor, respectively the pump, have to be considered in the future as it is explained later on in this chapter. This implies that the power electronics must be able to handle the thereby arising electromagnetic compatibility (EMC) issues. In addition to the beforehand mentioned points also considerations are carried out in this theses that tackle this problem. A more detailed insight into the specific demands of these future markets and their peculiarities are outlined in section 1.1.3.

1.1.1 State-of-the-art Bearingless Slice Motor Pump

An electric motor is called a bearingless motor if, without the help of additional equipment, the torque as well as radial forces with a defined direction and amplitude can be generated on the same iron circuit. This term was introduced in [1]. It does by all means not stand for the absence of any bearing forces, but is shall indicate that there are no bearings present outside the electric motor.

The concept of the bearingless slice motor was developed by [2]. This temple motor design provides a means of levitating an impeller completely without any mechanical contact. The schematic of this motor configuration in a centrifugal pump setup is depicted in Fig. 1.1. As it is the case for any rotor which has has to be completely magnetically

levitated, also the rotor in this configuration has six spatial degrees of freedom that have to be stabilised magnetically through the wall between the stator and the rotor. Three of them are stabilized passively, i.e. the axial displacement (in z -direction) and the angular displacement (tilting in x - and y -direction) [2]. The three remaining degrees of freedom are controlled actively, i.e. the radial displacement (in x - and y -direction) and the rotation around the z -axis. The magnetic levitation of the rotor is facilitated with rotors that have a small height to diameter ratio as it is described in [2]. The interactions of the Maxwell- and Lorentz-forces in a bearingless slice motor are described there as well. More information on the origin of these forces is provided in chapter 5 in the course of the comparison of feasible motor concepts for next generation bearingless pump systems.

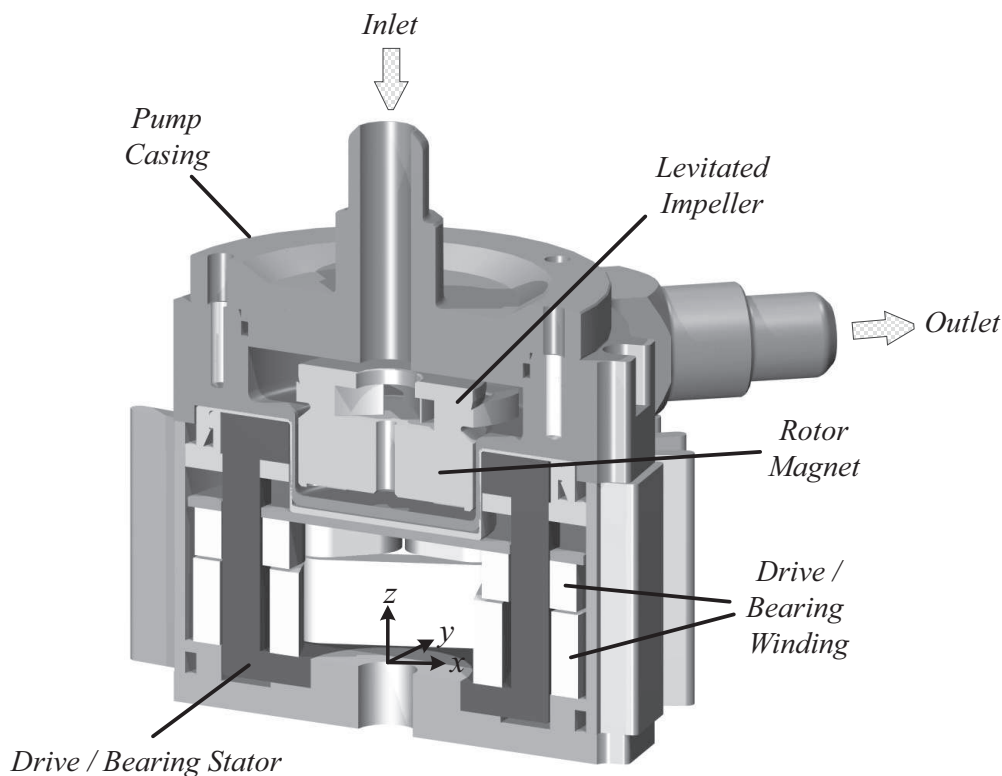


Figure 1.1: Cut view of the bearingless slice motor in a centrifugal pump setup.

Besides the levitating forces, the active motor part also generates the driving torque. Both bearing and drive windings are placed around stator claws, which are jointly carrying the bearing and drive flux. In its conventional configuration, the bearingless slice motor features two

orthogonally placed drive phases (D_1, D_2) and two likewise placed bearing phases (B_1, B_2) in a symmetrical winding configuration, where each phase is independently driven by a full-bridge circuit (cf. Fig. 1.2). The orthogonal placement of the coils in the motor yields a $\pi/2$ phase shift of the currents in the drive windings. Due to the winding arrangement of the separated coils, the flux phase difference between two neighboured bearing coils has to be $\pi/2$ to ensure levitation [2]. When the bearingless slice motor is employed in a centrifugal pump, a constant asymmetric force is acting on the rotor which is directed to the hydraulic outlet of the pump head. The origin of this force lies in the pressure loss at the outlet. Depending on the position of the pump outlet in respect to the bearing phases a load angle φ is occurring between the drive and bearing flux, respectively. This circumstance is analytically explained and verified by measurements in [3] and will therefore not be further discussed in this work. In the hereafter carried out analysis, φ is chosen in a way that a $\pi/2$ phase shift arises between the currents in the drive and bearing windings. This leads to maximum stresses in the power semiconductors and the motor windings and guarantees that the components can be selected based on a worst case analysis (see chapter 2.1).

The control of a bearingless motor is significantly more complex than that of a conventional magnetic bearing. In this concept, the currents which are required to generate a defined radial force are dependent on the angle of the drive field. Thus, the field angle of the drive has to be considered as an additional control input in field oriented control. The whole control structure of a bearingless motor is described in [4]. There, also the fundamentals for the calculation of the Lorentz- and Maxwell-shear-forces in a bearingless induction machine are presented. The therein described principles also serve as a base for the design of bearingless slice motors as they are described in [2]. The specific control structure of a bearingless slice motor is also derived in this work. In [5], the optimisation potential on the control part without any design modifications is analysed based on the results obtained in [2]. These results are generally applicable for any bearingless slice motor configuration.

Taking all these points into account reveals that the bearingless slice motor offers the best compromise between a reduction of the system complexity in machines with magnetically levitated rotors and a stable operation of the rotor since the same iron circuit is employed for the drive and bearing system. The compact form offers the potential for miniatur-

isation as well as certain freedom in the design of the pump head. Since only three of the six degrees of freedom have to be controlled actively the component effort is reduced compared to conventional magnetically levitated pumps [6]. However, the passive stabilisation results in a lower stiffness and damping compared to the three degrees of freedom that are controlled actively. This demands certain arrangements depending on the medium that is pumped. For example, the low stiffness limits the maximum tolerable axial force that occurs as a result of the delivery of fluids in rotating conveying systems. This issue is contemplated in [7] and it is furthermore shown how these disadvantages can be overcome with hydrodynamic or hydrostatic measures.

Linear amplifiers have been applied for the generation of the bearing and drive currents in the beginning of the development of bearingless motor systems. However, compared to switched amplifiers these systems face large power losses [8]. With the recent fast moving developments in the area of power electronics, switched amplifiers are the core of today's power electronics in bearingless pump systems. The control of the currents in each drive and bearing winding, and thus the flux, is conventionally performed by one separate full-bridge (FB) converter per phase (cf. Fig. 1.2). This results in totally 16 transistor/diode combinations for the drive and the bearing system of the bearingless slice motor, which means a considerable power electronics effort and also volume contribution to the overall system. Therefore, in this theses, alternative topologies with reduced complexity and number of semiconductors shall be comparatively evaluated considering their suitability to drive two-phase bearingless slice motors.

The full-bridges are operated with unipolar control as described in [9]. For the sake of simplicity, the modulation method is described here in its simplest form. The switches in the two bridge-legs are controlled separately by comparing the triangular signal u_{tri} with the control signals δ_{Tj} ($j = 1, 3$). E.g., for the control of the phase current $i_i(t)$ (cf. Fig. 1.2) the comparison of the relative duty cycle δ_{Tj} of the transistors T_1 and T_3 with the triangular waveform results in the modulation depth M_i given by

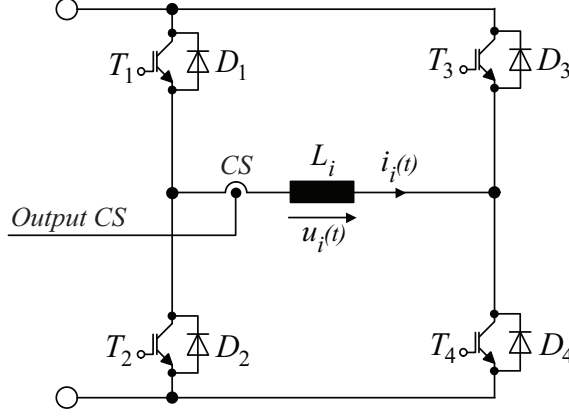


Figure 1.2: Full-bridge topology for the control of the drive and bearing windings ($i = D_1, D_2, B_1, B_2$). A current sensor (CS) is placed in each phase to measure the respective phase current.

$$\begin{aligned} M_i &= \delta_{T1} - \delta_{T3} \quad \text{for} \quad -\pi/2 < \varphi < \pi/2 \\ M_i &= \delta_{T3} - \delta_{T1} \quad \text{for} \quad \pi/2 < \varphi < 3\pi/2, \end{aligned} \quad (1.1)$$

where $\varphi = \omega t$ is the phase angle of the current $i_i(t)$. This easiest realisation of that modulation method results if the duty cycles δ_{T_j} are kept constant during a half cycle of the current sine wave. As depicted in Fig. 1.3 this results in a triangular current shape. A larger current ripple and higher *rms* components occur for this modulation method compared to a pure sinusoidal current which can be obtained by sinusoidal control signals δ_{T_j} . For the loss calculation carried out later on in this work, sinusoidal duty cycles are applied.

1.1.2 Principle of Magnetic Levitation

The working principle of the hereafter presented bearingless slice-motor is based on the theory of magnetic levitation. For the sake of brevity, only a short introduction on this topic is given here. A more deeper analysis of magnetic levitation and the respective theory can be found in [10].

If a ferromagnetic body shall be magnetically levitated in one direction without any additional mechanical bearings, a setup as shown in Fig. 1.4 is needed. It mainly consists of two electromagnets and the necessary

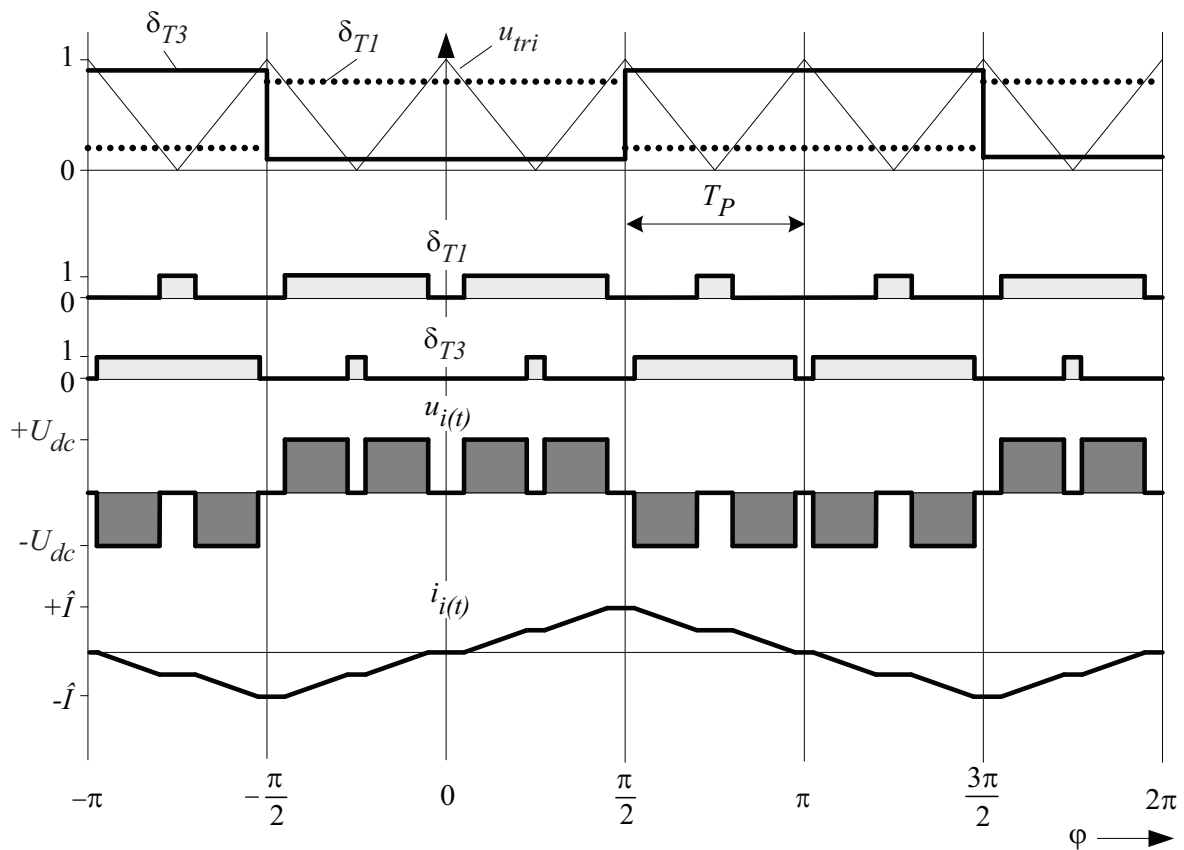


Figure 1.3: Switching pattern of the bridge leg of a full-bridge. For terms of easier explanation a very low switching frequency $f_s = 1/T_P = (2\omega)/\pi$ has been chosen, i.e. only one switching pattern occurs during a quarter current period.

control electronics, position and current sensors. Both electromagnets are biased with the current i_0 and as a result of this each of them generates an attracting magnetic force (F_{s1}, F_{s2}). A control current i_d is added to the bias current in winding 1 and subtracted from the respective bias current in windings 2. The attracting magnetic force F_{s1} of winding 1 is therefore increased because of the higher magnetic flux in the air gap. As a result of the subtraction of the control current i_d from the bias current i_0 , the magnetic force of magnet 2 is lower than the one of magnet 1. The interaction of these two forces yields to a resulting force F_{res} , which points into the direction of magnet 1. This setup needs to be extended if additional degrees of freedom must be controlled.

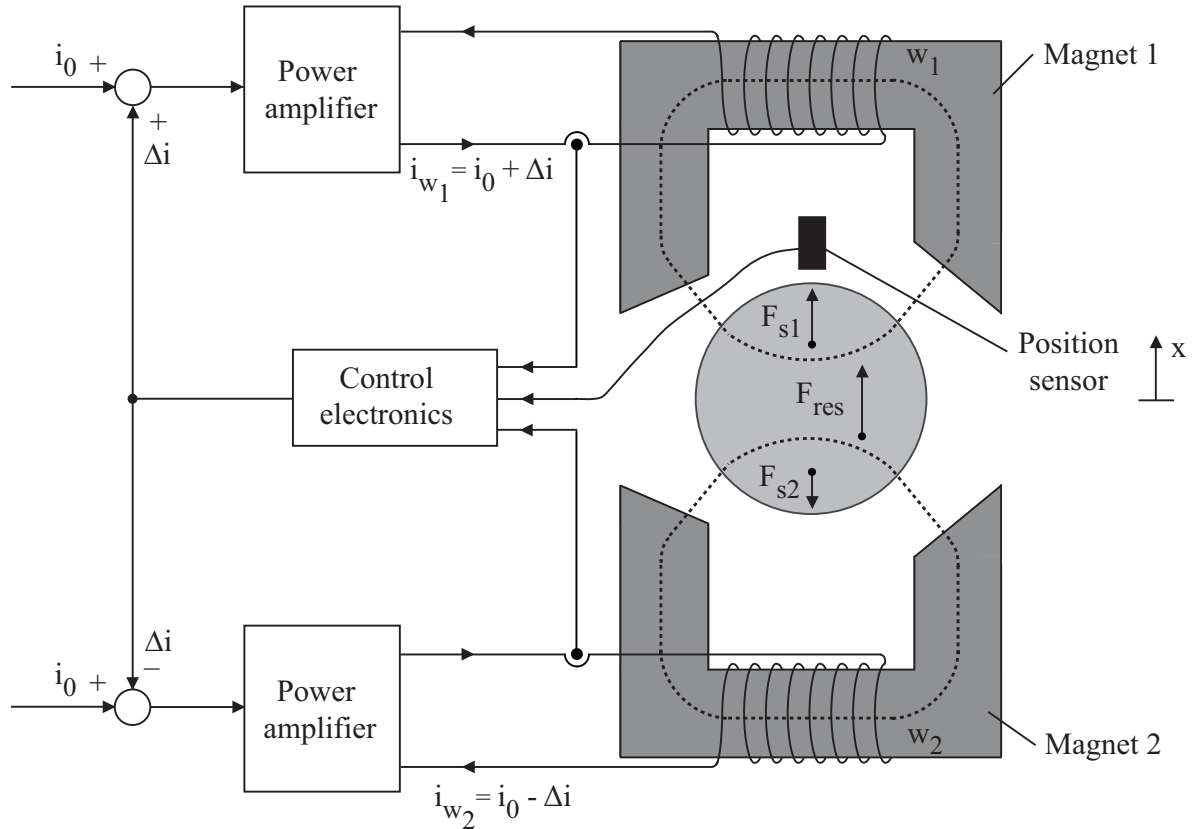


Figure 1.4: Principle of active magnetic bearing.

1.1.3 Challenges for Next Generation Bearingless Pump Systems

Already at the moment, the bearingless slice motor serves as a basis for a host of industrial applications. As mentioned earlier on, bearingless pump systems are widely accepted as fluid pumps in various applications in the semiconductor industry and as blood pumps in medical applications. A far bigger potential for this pump concept, however, lies in other markets such as the chemical and pharmaceutical industry, for food processing and in biotechnology applications when it is employed as a sanitary pump. Additionally, a huge market with a strong focus on long lifetime and reliability is the pump market for cooling and heating. However, cost pressure and the demanded production volumes are very high in this market so that it is not a first priority market for next generation bearingless pump systems. Similar circumstances also arise in the plating industry. In Fig. 1.5 an overview is given of potential application areas for next generation bearingless pump systems.

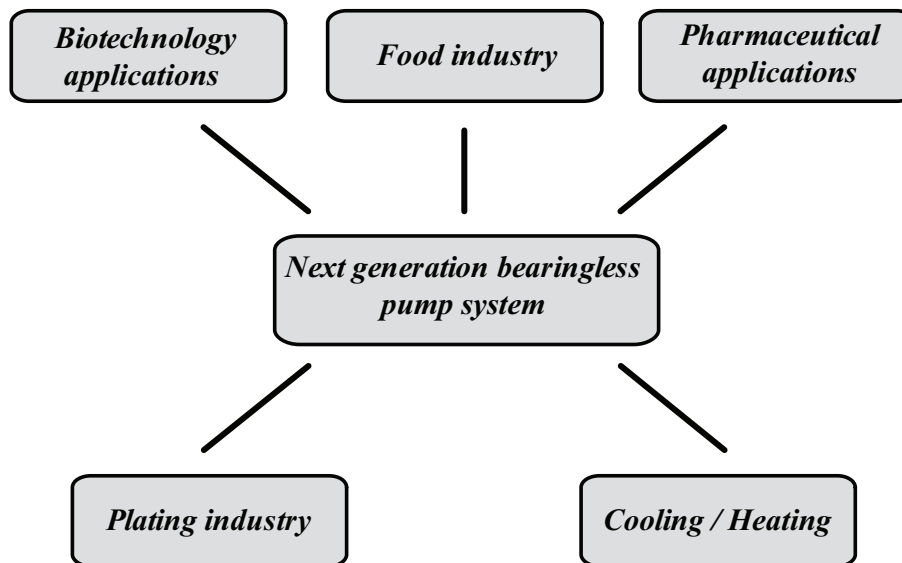


Figure 1.5: Overview of next generation application areas for bearingless pump systems.

Food–/Pharmaceutical–Industry

Sanitary pumps are used to transport and meter solutions, slurries and agricultural materials in operations where cleanliness is desired or mandated (e.g. in food processing plants). These pumps can be classified into the following groups:

- Centrifugal
- Positive displacement
- Jet
- Airlift

The dominating concept in food processing installations are stainless steel centrifugal pumps. They are employed to deliver fats and oils, flavorings and sweeteners in bakeries, as well as beverages such as soft drinks, wine and beer. And in dairies, whey, cream and milk are transported with these pumps.

Positive displacement pumps have an expanding cavity on the suction side of the pump and a decreasing cavity on the discharge side. The liquid flows into the pump as the cavity on the suction side expands and

is forced out of the discharge side when the cavity collapses. A positive displacement pump cannot be completely throttled because it is operated against a closed valve on the discharge side. If complete throttling is attempted, it will continue to produce flow, increasing the pressure in the discharge line until either the line bursts, the pump is severely damaged, or both. Positive displacement pumps are generally applied for the delivery of mediums with higher viscosity than those mentioned in the context with the centrifugal pump.

Airlift and jet pumps are not as common in sanitary applications as centrifugal and positive displacement pumps. In Fig. 1.6(a) an airlift pump is shown. It is not a pump in the strictest sense because it does not significantly alter the pressure or velocity head of the fluid in any practical degree. Air or other gas is delivered at the bottom of the lift pipe and mixes with the liquid. The air-liquid mixture, with lower specific weight than the liquid, rises in the pipe and is discharged at the point above the level of the liquid. This device can be used for elevating liquids that contain foreign materials or are corrosive. Twenty to 40% of the energy used to compress the gas is effective in elevating the liquid. The jet pump (Fig. 1.6(b)) operates on the velocity energy of a fluid jet. The fluid is forced through a jet or nozzle so that all or nearly all of its energy is converted into velocity energy. The energy is directly applied to the fluid to be moved. Jet pumps are frequently used for pumping sumps or process residues that contain solid matter or chemically active materials. When the jet is produced by a recirculated stream, the centrifugal pump must be protected from damage by solid particles in the fluid stream [11].

Protection of the sanitary pump is imperative since these pumps are expensive and a pump failure results in costly downtime. Protection schemes for sanitary pumps include over-pressure, bearing-wear, dry-run and contaminant protection. Dry-run conditions occur when the pump is operated without any medium. Conventionally, protection from dry-running is achieved with a downstream pressure sensor. This, however, requires additional equipment located next to the pump which leads to higher system cost. In this aspect, the bearingless slice motor pump has a clear advantage since dry-running can be detected by means of the bearing and drive currents and no harm to the impeller is caused in this operating stage without the necessity of additional equipment.

Expense is also a major criterion in the selection of a sanitary pump. Costly, corrosion-resistant materials (such as stainless steel) are spec-

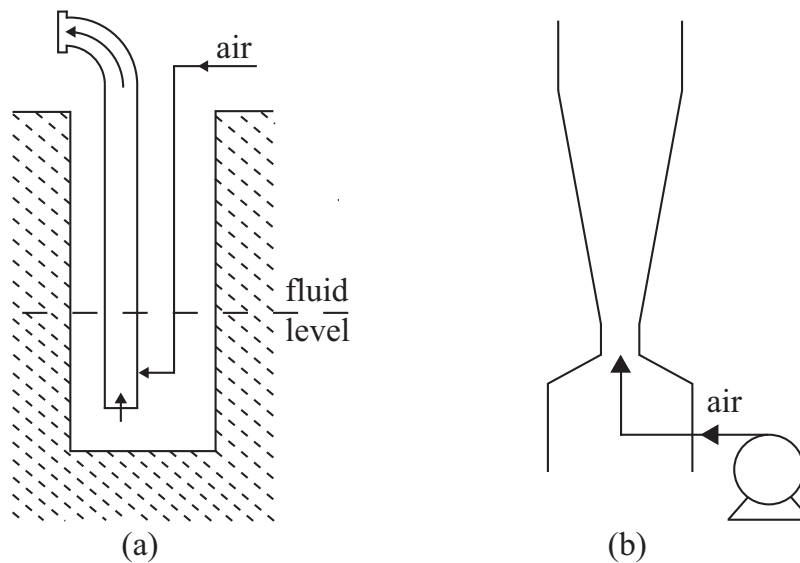


Figure 1.6: Principle of operation of (a) air lift and (b) jet pump.

ified for product contact areas. Surfaces that are in contact with the product must be cleanable and smoothly polished. In order to facilitate disassembly for cleanup quick-change fasteners, flanges, and gaskets are incorporated. Components are usually simple and designed to be extremely rugged to withstand constant disassembly for the cleanup procedure. Finally, sanitary pumps must be reliable because pump downtime translates to costly production downtime. Looking at all these requirements for sanitary pumps reveals that the bearingless slice motor pump is perfectly suited for these applications. Due to its pump design that only consists of the pump case and the impeller without any additional mechanical bearings the disassembly for cleanup procedure is very easy to obtain. This results in major cost savings during operation and justifies the higher initial price of this pump concept compared to standard pumps that are driven by three-phase AC motors. These AC motors also account for a major part of the volume of such a standard sanitary pump. Since the drive part of a bearingless slice motor pump is integrated in the housing as shown in Fig. 1.1, the overall volume is significantly reduced compared to standard pumps. The application of bearingless pump systems in these cost-sensitive applications involves the necessity of power electronic systems with reduced complexity and costs.

The market for fluid handling equipment is dominated by one major player that holds 40 to 50% market share. Behind that, several smaller players account for 5 to 10% market share, each. The rest of this market

is occupied by a large number of small companies whose products serve several niches. Taking all the beforehand mentioned benefits of a bearingless slice motor pump into consideration reveals that there is a realistic chance for this product to enter the fluid handling market. Especially for pharmaceutical applications, which is the biggest segment in this market. There, cost pressure is only slightly higher as in the semiconductor industry and similar to that industry high requirements for cleanness and reliability are demanded. Thus, these preconditions are ideal for a new product to enter a market.

Wet Semiconductor Processing

Besides the beforehand mentioned markets, also the semiconductor industry demands bearingless pump systems with a reduced volume compared to today's systems. In this market, the bearingless slice motor pump has already gained significant market share and it is therefore important to put even more research effort into these systems in order to keep the current market share or even increase it. The various benefits of the bearingless pump for the handling of very pure and aggressive fluids in the semiconductor industry are described in [12]. The trend towards constantly increasing miniaturisation in this industry [13], [14] demands new solutions in the production process. This goes along with ever increasing cleanroom requirements. In effect, cleanroom space is the major cost driver in this industry.

Due to ever decreasing semiconductor prices, also economy of scale is of major interest. As a consequence of this, the number of semiconductor production machines has to be increased or the throughput of the machines needs to be expanded while at the same time the available cleanroom space stays the same or is even lowered. As a matter of fact, the volume of the components assembled in these machines must be lowered. This directly affects the bearingless pump system that is employed to deliver the process fluids in these facilities. A trend can be seen that the control and power electronics of these systems must be placed outside the cabinets. This implies that relatively long power and sensor cables (up to 20 m) between the motor and the controller, respectively the power electronics, must be handled. However, reducing the volume itself is not sufficient. Also the complexity of these systems must be targeted as a point for cost reduction. Therefore, besides focusing on lowering the

volume and thus increasing the power density of the power electronics the focus is also put on reducing the complexity of the bearingless slice motor itself in this work.

1.1.4 Cost Reduction Approach

A bearingless pump system is a mechatronics system in a classical way that consists of several components which interact and thereby influence each other. The main components of such a system are listed in Fig. 1.7. Namely, a controller including the power electronics, current sensors and the digital control, the bearingless motor with a specific winding arrangement and position sensors as well as the pump head including the impeller. In the following, the highlighted parts are tackled in this work, whereas the dashed boxes will only shortly be described in this section. They will not be further investigated hereafter since their impact in terms of cost and volume reduction on a next generation pump system is only low.

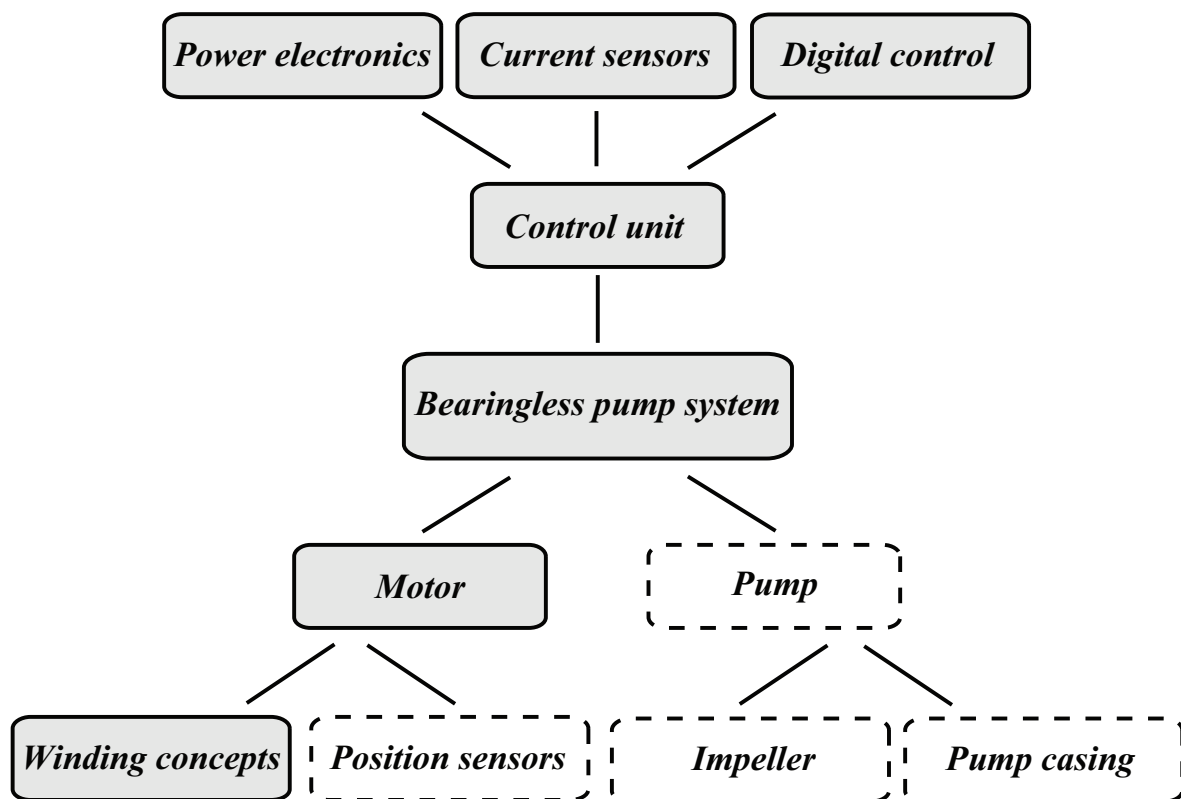


Figure 1.7: Overview of the main components of a bearingless slice motor system.

Position Sensors

The axial and radial position sensing of a magnetically levitated rotor can be accomplished with different sensor principles. In the following, a brief introduction is given about different sensor concepts and their basic operation principle. In applications where a magnetically conductive rotor is present inductive sensors are the appropriate choice. They consist of a coil with an alternating current flowing through it. The impedance of the coil is changing depending on the distance between the sensor and the rotor.

Furthermore, eddy current sensors can be used for the position sensing. Similarly to inductive sensors they are built with a coil. However, the difference between the two sensors principles lies in the excitation frequency. In the case of the eddy current sensor the excitation frequency lies in the range of 100 kHz up to a few MHz. Due to the higher excitation frequency compared to the inductive sensor the bandwidth of an eddy current sensor is higher. The material of the rotor that is in interaction with the sensor via the electric field should ideally be nonmagnetic but with a high electrical conductivity so that it extracts energy from the electric field. This energy difference is a measure for the distance between the rotor and the stator.

A further alternative for the position sensing are magnetic sensors. There, a constant current in a ferromagnetic circuit with an air gap generates a magnetic field. The magnetic flux density in the air gap depends on the distance between the source of the field and the sensor that measures the field. Hall sensors are a suitable device for that. However, this sensor concept is by its nature very sensitive to magnetic stray fields and thus must be applied carefully.

The principle of a capacitive sensor is based on two electrodes that are placed next to each other along the stator. This sensor arrangement is driven by an alternating current. The respective voltage that occurs between the two electrodes is then proportional to the distance between the rotor and the electrodes.

A deeper discussion and evaluation of different sensor types and their applicability for the position measurements through certain media is given in [6]. All these sensor concepts have in common that their complexity is already minimised to a level where only very little achievements towards cost reduction can be achieved. Compared to the potential that

lies in the power stage a cut down of a single capacitor or resistor in the sensor electronics is negligible. Due to these reasons the sensor part of the bearingless motor will not be further analysed in this work and the existing concepts will be applied for the position measurement of the rotor.

Pump

The two main components of a centrifugal pump are the rotating impeller and the stationary pump casing. These pumps are well suited for applications involving variable flow rates. Their flow capacity can either be regulated by varying the speed of the impeller or by throttling the pump with an adjustable valve. Choosing the latter has several drawbacks such as that the system pressure is increased and also energy is wasted. The specific behavior of the impeller in a bearingless pump system was investigated in [7]. In all the beforehand described application areas, the flow and pressure parameters achievable with the hereafter employed pump are sufficient. Therefore, this part of the pump system will not be further investigated in the following.

Chapter 2

Power Electronics

2.1 Introduction

As outlined in the previous chapter the trends in the semiconductor industry as well as in upcoming markets for bearingless pump systems demand more compact and thus volume optimised pump systems. Especially a major volume decrease is demanded for the power electronics of such a system. Thus, this chapter deals with the design of the power stage of a next generation bearingless pump system. First, a comparison of possible voltage-source inverter topologies with a reduced number of semiconductor switches is carried out. Based on this evaluation, the topology for a next generation bearingless pump system as well as the power semiconductors are selected. Following this, the semiconductor stresses arising in the chosen topology are presented. The design of the heat sink is then shown based on switching loss measurements carried out on the selected semiconductors. Subsequent to the thermal analysis of the heat sink the emphasis is put on the calculation of the dc-link capacitor.

2.2 Inverter Topology Selection

In order to assist in the choice of the proper inverter topology to be used in this work this section gives an overview about possible converter

topologies with a reduced number of power semiconductor switches suitable for the control of a two-phase bearingless slice motor. In a first step, the standard full-bridge topology is introduced. The emphasis is then put on topologies with a lower number of semiconductor devices. This will provide the base for a volume optimised power electronics.

2.2.1 Full-Bridge Topology

In today's bearingless pump systems each phase of the drive and bearing system is controlled with a separate full-bridge (FB) voltage-source inverter. This results in a total number of eight power transistor/diode combinations for the drive system 2.1. Analogously, the same number of semiconductor devices is needed to operate the bearing system. So that in total 16 power transistors are required to operate the pump with this configuration. The maximum voltage applicable to the clamps of each winding $U_{cl,max}$ when operated with this topology is equal to the dc-link voltage U_{dc} :

$$U_{cl,max} = U_{dc}. \quad (2.1)$$

Similarly, this is also the case for the maximum voltage applicable to the bearing windings.

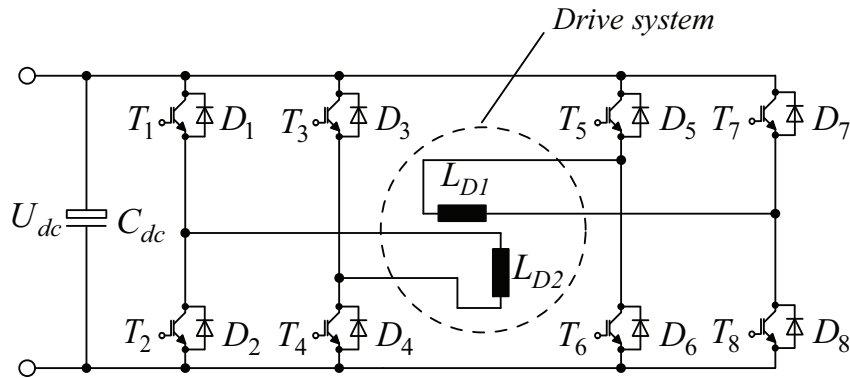


Figure 2.1: State-of-the-art full-bridge topology.

This structure, which is based on the control topology of conventional magnetic bearing systems, allows the independent control of the current in each drive and bearing phase. Due to the lack of integrated full-bridge power modules the realisation of this topology is carried out

with discrete components. On the one hand, this has the advantage that the power semiconductors can be purchased in higher numbers which reduces system costs, on the other hand the number of external components (eg. driver chips) also increases. This significantly influences the price of the power electronics. For this reason, the focus in the selection of the next generation voltage–source inverter topology is put on concepts which allow the employment of integrated power modules that do not require additional driver circuits for the switches. These would allow the reduction of the overall component costs.

2.2.2 Split–Capacitor Topology

The split-capacitor (SC) topology depicted in Fig. 2.2 has been first introduced in [15], where a two–phase induction motor is fed by a two–phase inverter for applications requiring constant or very little speed variations such as for heating, cooling and pumping. Its behaviour has then been further investigated for two–phase induction motors in various other applications [16], [17]. Due to the reduced number of semiconductor switches this structure is less expensive than the full–bridge topology and thus, its applicability has also been analysed for the control of three–phase induction machines [18].

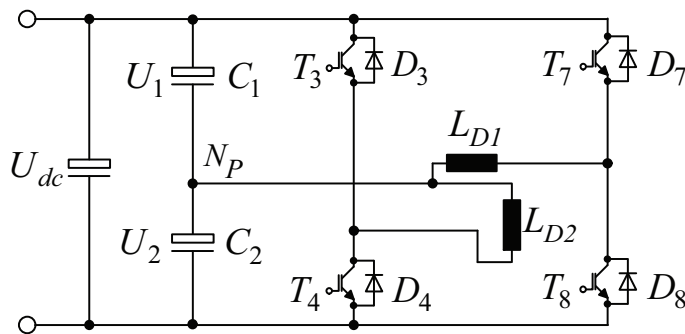


Figure 2.2: Split–capacitor topology.

It shall therefore be investigated in the following whether this concept is also practical for the control of two–phase bearingless slice motors. To do so, the two coils of each drive and bearing phase are connected to a neutral point N_P , which is then attached to the midpoint formed by two capacitors placed in the dc–link. The total number of semiconductors needed to operate the bearingless slice motor with this topology is reduced from 16 to 8 compared to the full–bridge topology. In recent

years, various control schemes have been proposed for inverter driven two-phase induction motors [19], [20], [16] operated with the SC topology. In [16], a square-wave modulation method is described in order to increase the available drive voltage. However, for the application at hand this would result in excessively high drive currents at low rotational speeds and thereby exceeding the maximum allowed currents of the IGBT's. Thus the duty-cycles of the switches in the two bridge-legs are sinusoidally modulated instead of employing square-wave modulation. This leads to a maximum output voltage of half the dc-link voltage for the SC-topology

$$U_{max,SC} = 0.5 \cdot U_{dc}. \quad (2.2)$$

Unlike a semiconductor switch-leg, the SC-leg obviously does not need additional gate drives or control circuits. Capacitors, however, limit the lifetime of the whole power electronics unit due to their low mean time to failure (MTTF). Especially, this drawback becomes aggravated by the hard operating conditions expected in pump applications such as high temperatures and high rms currents. In case of a breakdown of one capacitor the second one has to withstand the full dc-link voltage. For this reason, both capacitors have to be rated for the full dc-link voltage which will increase the cost. An additional drawback is that this topology suffers from unbalances due to uneven discharging of the capacitors arising from speed and torque variations. This implies that an appropriate control of the voltage across the capacitors is necessary. The voltages across the two capacitors can be balanced by placing two resistors in parallel to each of the two capacitors. This, however, results in additional circuitry and higher power losses [21].

An alternative concept is presented in [22], where a balancing circuit is placed across the two capacitors resulting in additional sensing and control effort which is contrary to the main approach of reducing the overall complexity. All these balancing efforts have in common that they increase the overall complexity and cost of the system and thus are contradicting the targeted cost reduction approach for the power electronics.

2.2.3 Interleaved Half-Bridge Topology

An alternative concept to overcome these problems is depicted in Fig. 2.3. The idea behind this configuration is to connect one or several motors with a number of phases that is uneven to three to a three phase converter. This configuration has been first proposed for the connection of two two-phase induction machines in [23] and is further investigated in [24], [25], [19], [26], [27], [28]. One leg of the five-leg inverter is simultaneously connected to both machines while the remaining inverter legs are connected to the two machines only. In a similar way it is also applicable for the control of a two-phase bearingless slice motor. Instead of connecting the two open ends of the drive windings to the junction of the dc-link capacitors as discussed in the previous section, they are connected to a third half-bridge that forms a common bridge leg for both windings. As a result of this, the converter comprises three interleaved half-bridges (IHB) for the drive system and another three IHB for the bearing system (not shown in Fig. 2.3). Still a major shortcoming of this topology is the need to increase the dc-link voltage in order to achieve similar performance results as with the state-of-the-art full-bridge topology. Analogue to the case for the before mentioned control of two induction machines by one multi-leg inverter [29], [30], [31] new modulation schemes must be developed in order to achieve an increased performance and better dynamical behaviour of the pump system as compared to the SC-topology. This issue is tackled in chapter 4 of this work.

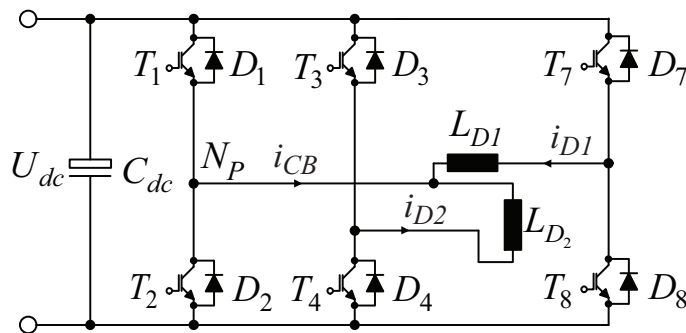


Figure 2.3: Interleaved half-bridge topology with three bridge-legs of which only the drive system is shown.

An important advantage of the interleaved-half-bridge topology is the possibility to employ integrated three-phase power modules, which is

advantageously in various aspects such as higher compactness, lower cost as well as integrated features like short-circuit protection and integrated gate drivers. These advantages are alleviated slightly by the fact that the switches in the common bridge-leg are involved in the switching of both phase currents and thus face higher current stresses compared to the ones in the separate bridge legs. In a worst case assumption the connection of the two phases to the neutral point N would result in twice the current stress for the power transistors in the common bridge leg. However, as a result of the fact that the drive windings are placed orthogonally to each other the respective currents show a phase shift of $\pi/2$ [2]. Assuming that under steady-state operation the currents in both drive phases show similar values the peak current in the common bridge-leg results in 1.4 times the drive current of one phase (cf. Fig. 2.4). The possible wiring concepts of the drive and bearing phases to the two modules and the thereby arising losses are investigated in section 2.3.5.

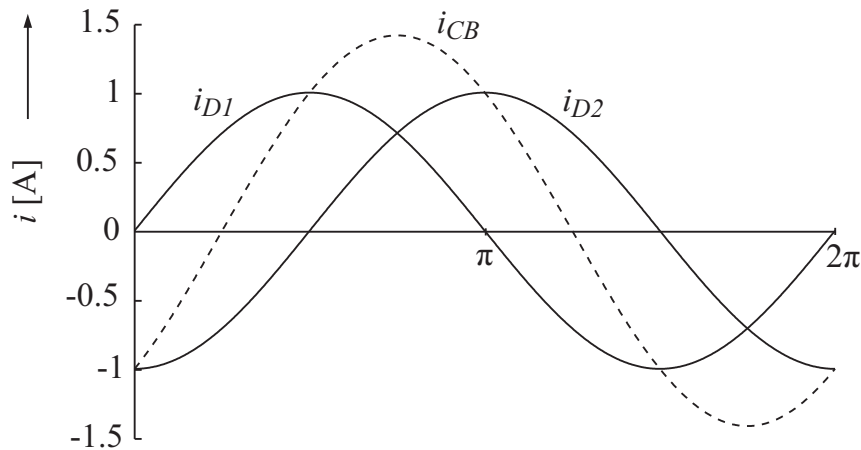


Figure 2.4: Phase shift between the drive currents I_{Di} ($i = 1,2$) and the common bridge-leg current i_{CB} . The resulting common bridge-leg current in the bearing system shows the same behaviour.

2.2.4 Comparison of the Topologies

Several system advantages of the proposed interleaved half-bridge topology have already been mentioned. Finally, the data of the overall volumes and the number of required switches is compiled in Fig. 2.5. For the volume calculation of the semiconductors of the full-bridge and the split-capacitor topology the same components in discrete form as they

are integrated in the three-phase power module presented in section 2.3.2 are used. The specific parameters of the IGBT's can be found in [32].

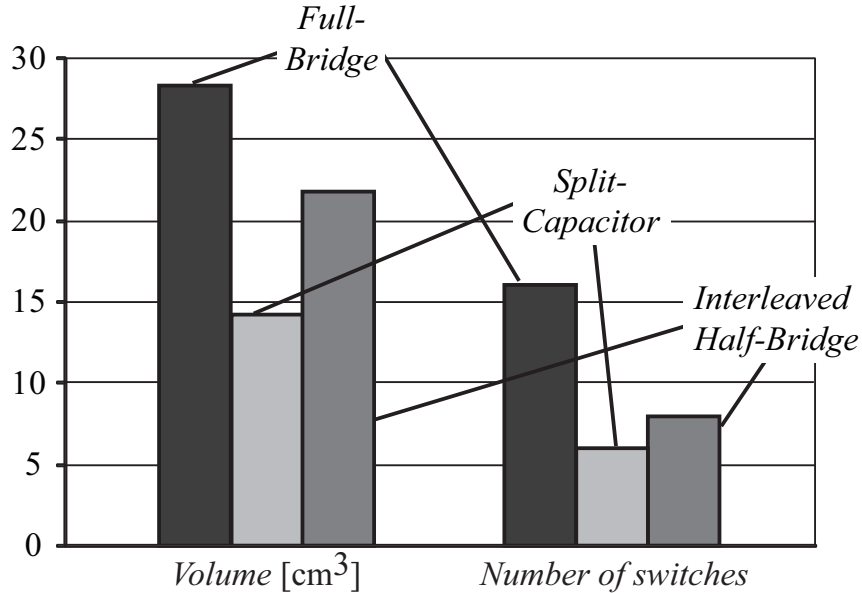


Figure 2.5: Semiconductor volume and number of switches of the discussed topologies.

For the volume comparison, only the package of the semiconductors without any space required by the leads is considered. In Table 2.1 a qualitative comparison of the discussed topologies is compiled. The comparison includes the available clamp voltage, the number of utilised components as well as practical system aspects. For the interleaved half-bridge topology the modulation method with maximum achievable clamp voltage (see section 4.4.3) is taken into account. The maximum applicable clamp voltage directly influences the achievable drive power of the the motor (see section 4.5.2).

The comparison shows that the split-capacitor topology cannot be used for bearingless pump applications due to significantly reduced clamp voltage and drawbacks such as reduced life-time due to more dc-link capacitors and the requirement for a balancing circuit. On the other hand, the interleaved half-bridge topology seems to be a very attractive alternative for driving bearingless pumps, since the available drive voltage and drive power, respectively, are only slightly reduced, while the number of semiconductors is decreased by 25%. A drawback is the higher current rating of the semiconductors (at least of the common bridge leg). However, the possibility of the employment of highly compact integrated

Topology	SC	IHB	FB
Maximum drive voltage	$0.5 \cdot U_{dc}$	$0.86 \cdot U_{dc}$	U_{dc}
Number of dc-link capacitors	2	1	1
Number of semiconductor switches	8	12	18
Number of bridge legs	4	6	9
Balancing circuit	yes	no	no
Employment of integrated three-phase power modules	no	yes	no
Maximum semiconductor current rating	\hat{I}_D	$1.4 \cdot \hat{I}_D$	\hat{I}_D

Table 2.1: Qualitative comparison of the different converter concepts.

three-phase power modules leads to a significant reduction potential in terms of power electronics volume in the range of 30% to 40%, which can also be very attractive for specific applications with a strong focus on highly compact converters (see section 1.1.3). Considering all these facts, the interleaved half-bridge topology emerges as the most suitable concept for the realisation of the power stage of a next generation bearingless pump controller.

2.3 Inverter Design

In the following section, the power semiconductors and the dc-link capacitors for the interleaved half-bridge are selected based on the requirements for next generation bearingless pump systems. The switching behaviour of the selected power transistors is analysed and based on this the calculation of the operating point dependent power losses in dependency of the wiring scheme of the drive and bearing windings is carried out. Before the calculation and selection of the required dc-link capacitor is shown, the design of the heat sink is presented based on these loss calculations.

2.3.1 Semiconductor Stresses

Prior to the selection of the power transistors the average current $I_{k,avg}$ and rms current $I_{k,rms}$ values in the semiconductor devices must be known. The respective power transistor or reverse diode is indicated with ($k = T, D$). In the following it is assumed that the drive and bearing currents are of sinusoidal shape as it is explained in section 1.1.1. For an analytical calculation of the global average current values the local current waveforms within each pulse interval t_μ have to be determined and averaged over a pulse interval T_p and then summed up over a mains period. This summation can be replaced by an integration of the local averaged values $i_k(\varphi)$ over the mains period under the assumption that the switching frequency is sufficiently higher than the fundamental frequency of the switched current [33]

$$I_{k,avg} = \frac{1}{2\pi} \int_0^{2\pi} i_k(\varphi) d\varphi = \frac{1}{2\pi} \int_0^{2\pi} \left(\frac{1}{T_p} \int_0^{T_p} i_k(\varphi, t_\mu) t_\mu \right) d\varphi, \quad (2.3)$$

where $\varphi = \omega t$ defines the actual position of a pulse interval within a mains period and t_μ the actual position within a pulse interval. Analogously, the square of the global rms value can be found by integration of the square local rms value

$$I_{k,rms}^2 = \frac{1}{2\pi} \int_0^{2\pi} i_k^2(\varphi) d\varphi = \frac{1}{2\pi} \int_0^{2\pi} \left(\frac{1}{T_p} \int_0^{T_p} i_k^2(\varphi, t_\mu) t_\mu \right) d\varphi. \quad (2.4)$$

The modulation index M_i is defined by the ratio between the peak voltage $U_{cl,i}$ at the clamps of a drive or bearing phase ($i = D, B$) and the maximum clamp voltage $U_{cl,max}$ that can be obtained with the voltage-source inverter for a specific modulation method (as will be shown in chapter 4). The definition of the modulation index M_i is thereby given by

$$M_i = \frac{\hat{U}_{cl,i}}{U_{cl,max}}. \quad (2.5)$$

According to Fig. 2.6 the clamp voltage $U_{cl,i}$ of a drive or bearing phase is defined as

$$\hat{U}_{cl,i} = \omega L \hat{I}_i + R \hat{I}_i + \hat{U}_{ind,i}. \quad (2.6)$$

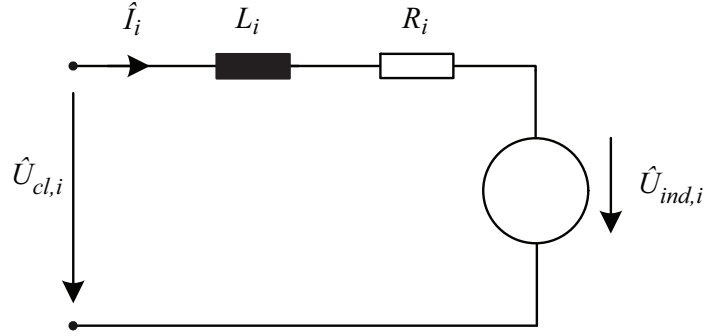


Figure 2.6: Equivalent circuit of one bearing or drive phase.

The resistive voltage drop $R \hat{I}$ in (2.6) is small compared to the voltage drop across the inductance and the induced voltage in typical bearingless motor configurations and can therefore be neglected for the calculation of the modulation index. Considering this, the combination of (2.5) with (2.6) leads to

$$M_i = \frac{\sqrt{(\omega L \hat{I}_i)^2 + (\hat{U}_{ind,i})^2}}{U_{cl,max}}. \quad (2.7)$$

For the calculation of the rms- and avg- current values in the semiconductors the switching patterns of the involved switches must be known. In Fig. 2.8 a sinusoidal current in the inductor L_i of Fig. 2.6 is considered. During the period 0 to $\pi/2$ of $i_i(\varphi)$ the transistor/diode combinations 1,2,3 and 4 of the interleaved half-bridge (cf. Fig. 2.3) are involved in the switching of this sinusoidal current. The respective switching pattern is shown in Fig. 2.7. This full-bridge is formed by the common bridge-leg consisting of the transistor/diode combination T_1/D_1 along with the separate bridge-leg realised with T_3/D_3 and T_4/D_4 of the involved half-bridge shown in Fig. 2.3. In this $\pi/2$ period the switching sequence is $1 \rightarrow 2 \rightarrow 3 \rightarrow 4$.

The local average current in each semiconductor that is involved in the switching of the current during a $\pi/2$ period is

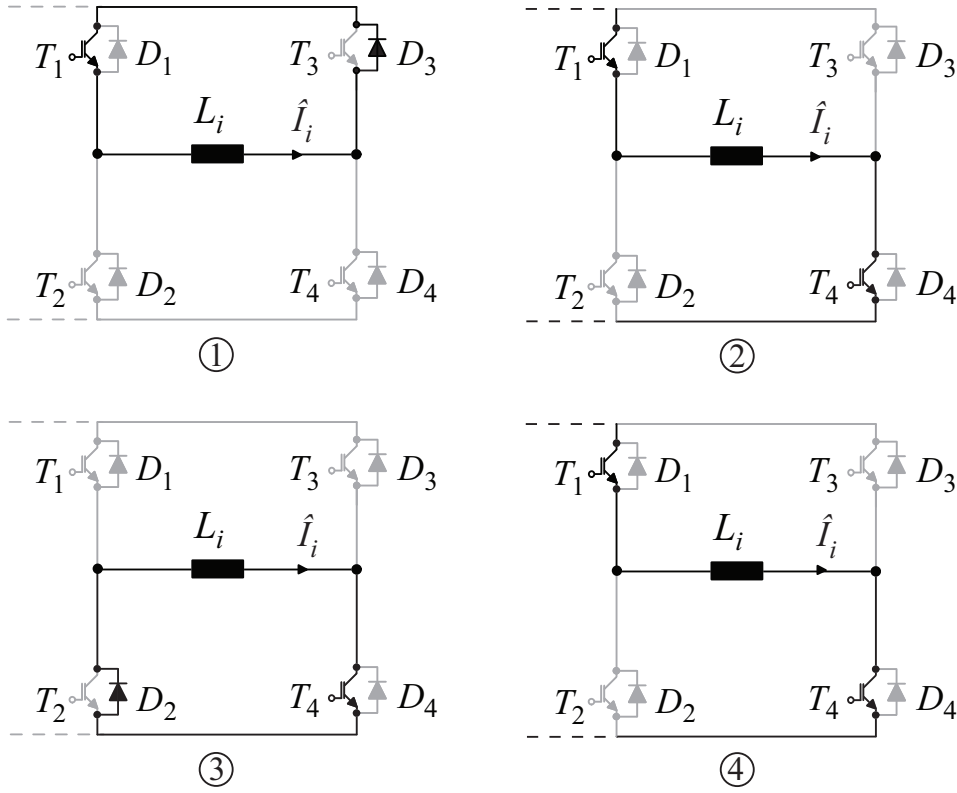


Figure 2.7: Switching pattern of the involved semiconductors T_1 , T_4 , D_2 and D_3 during 0 to $\pi/2$ of the current i_L in Fig. 2.8. Switching order $1 \rightarrow 2 \rightarrow 3 \rightarrow 4$.

$$i_k(\varphi) = \frac{1 - M \cos \varphi}{2} i_i(\varphi) \sin \varphi. \quad (2.8)$$

Exemplarily, with (2.3) and (2.8) the global average current of the transistor T_3 can now be calculated to

$$\begin{aligned} I_{T_3, avg} &= \frac{1}{2\pi} \int_0^\pi \frac{1 - M \cos(\varphi)}{2} i_i(\varphi) \sin \varphi d\varphi. \\ &= \frac{\hat{I}_i}{2\pi}. \end{aligned} \quad (2.9)$$

Here, \hat{I}_i is the peak current in the phase which is connected to the transistor T_3 . Due to the symmetry of the applied switching pattern, this value equals the one of the global average current in the corresponding

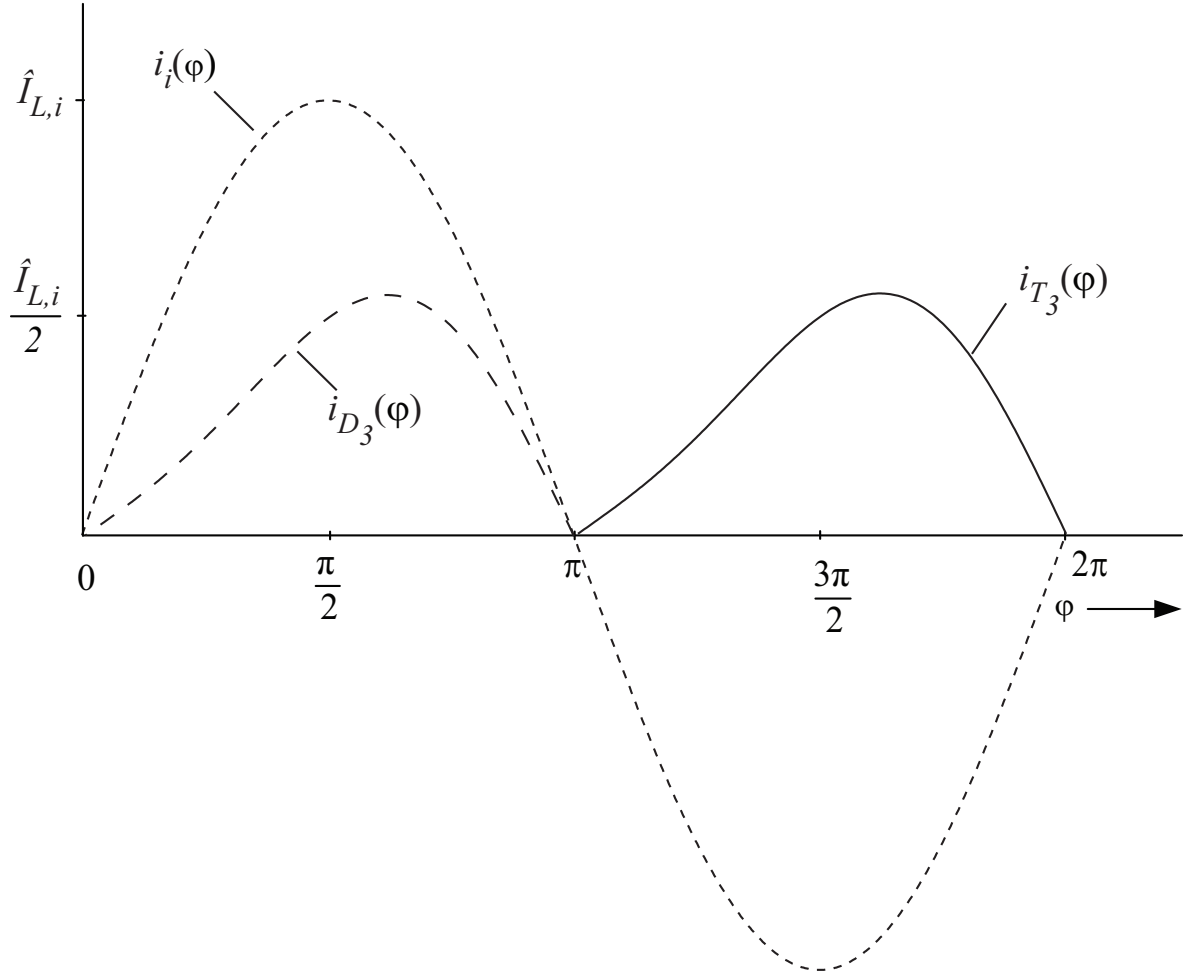


Figure 2.8: Time behaviour of the local average values of the currents in the power transistor T_3 ($i_{T_3}(\varphi)$) and the reverse diode D_3 ($i_{D_3}(\varphi)$) for a modulation index of $M = 0.5$. The local average current $i_i(\varphi)$ in the coil L (cf. Fig. 2.7) is also depicted.

diode. Thus, for all diodes and transistors in the separate bridge legs the average currents are equal ($I_{T_k,SB,avg} = I_{D_k,SB,avg}$). The current in the power semiconductors of the common bridge leg is $\sqrt{2}$ times the value of the one in the separate bridge legs due to the superposition of the two involved phase currents as outlined in section 2.2.3. Assuming sinusoidal currents with each having a peak value of \hat{I}_L in the two involved phases the global average current in the semiconductors of the common bridge leg is calculated to

$$I_{T_k,CB,avg} = I_{D_k,CB,avg} = \frac{\hat{I}_i}{\sqrt{2}\pi}. \quad (2.10)$$

Analogously to (2.9), the global rms current in the transistor T_3 is calculated with (2.4) to

$$\begin{aligned} I_{T_3,rms} &= \sqrt{\frac{1}{2\pi} \int_0^\pi \left[\frac{1 - M \cos(\varphi)}{2} \hat{i}_i(\varphi) \sin\varphi \right]^2 d\varphi} \\ &= \frac{\hat{I}_i}{4} \sqrt{\frac{1 + M^2}{4}}. \end{aligned} \quad (2.11)$$

Again, this rms value applies to all semiconductors in the separate bridge legs ($I_{T_k,SB,rms} = I_{D_k,SB,rms}$). Supposing that both phase currents \hat{I}_i show similar values, the rms current in the transistors/diodes of the common bridge leg results in

$$I_{T_k,CB,rms} = \frac{1}{4} \sqrt{\left(\sqrt{2} \hat{I}_i \right)^2 (1 + M^2)} = \frac{\hat{I}_i}{2\sqrt{2}} \sqrt{1 + \frac{M^2}{4}}. \quad (2.12)$$

The average and rms values for all devices are compiled in Fig. 2.9.

As described in section 1 bearingless motor systems are generally operated with unipolar control. Due to its simplicity and robustness this control scheme will also be applied for the interleaved half-bridge topology. This implicates that the maximum blocking voltage of all semiconductors equals the full dc-link voltage. When the converter is operated at the single phase mains, the maximum dc-link voltage is 325 V, whereas a three-phase mains yields to a voltage level of $\sqrt{2}\sqrt{3} \cdot 110 \text{ V} = 270 \text{ V}$ in the dc-link. Thus, the minimum blocking voltage is defined as:

$$U_{min,T,k} = U_{min,D,k} = \sqrt{2} \cdot 230\text{V} = 325\text{V}. \quad (2.13)$$

In the selection process of the power semiconductors the switching overvoltages that arise at the switching instant must also be considered. Experimental measurements have shown that a maximum overvoltage of $\Delta V = 50 \text{ V}$ is occurring. Thus selecting semiconductors with a blocking voltage capability of 600 V is sufficient.

The design requirement of a universally applicable bearingless motor controller implies that the power semiconductors must be selected for the

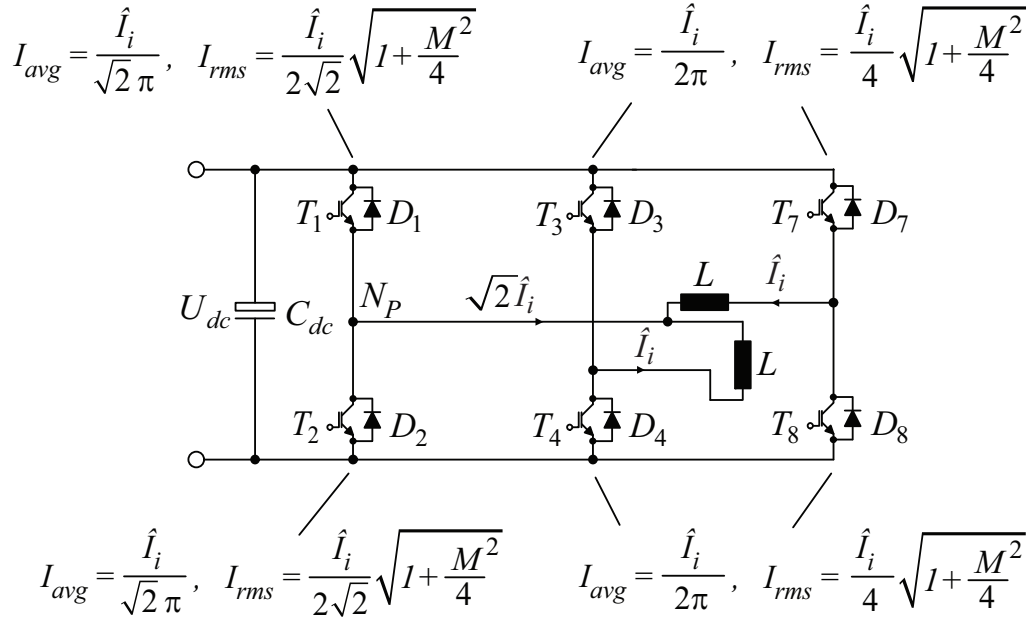


Figure 2.9: Analytical approximations of average and rms values of the component currents for the interleaved half-bridge topology in dependency of the current \hat{I}_L in the windings. This represents the case where one module is reserved for the drive and a second one for the bearing system (see section 2.2.3).

highest currents that occur in bearingless motors rated power of 2000 W. In the case that a bearingless hollow shaft drive [34] is operated with this converter, the phase currents can rise up to 18 Arms during acceleration. Thus, the selected power semiconductor must at least have a current capability of $\sqrt{2} \cdot 18A \approx 25 A$.

2.3.2 Power Module IRAM136-3063B

So far, the power stage of a bearingless slice motor controller is realised with discrete components. This offers the advantage that the latest semiconductor technology can be employed. In the case that customised power modules employing latest semiconductor technology are taken into consideration for a certain application the price competitiveness is low compared to a realisation of the power stage with discrete components due to the relatively low production volumes of bearingless pump systems. Integrated modules, however, that are available off-the-shelf and thus manufactured in high quantities offer a promising alternative to a realisation with discrete components.

Semiconductor manufacturers have put strong effort in the development of integrated three-phase power modules in recent years. Such components have originally been designed for air conditioning systems, compressor drives as well as for light industrial power applications. Lately, their utilisation in various other applications has continuously increased and they can now be found in large numbers in a lot of other applications. As a consequence of this trend, these modules are produced in high volumes and can therefore be offered at an attractive price for cost sensitive applications. Their integrated package offers a simplified design of the converter since the gate drivers and protection circuitry are integrated in the package as already mentioned in section 2.3. Also the assembly of the components is simplified when utilising power modules. Furthermore, the short inductive paths inside the modules provoke small overvoltages during switching transients. On the other hand, this realisation concept has the disadvantage that in case of a malfunction of one of the power transistors or diodes inside the module the whole device must be replaced. For the realisation of the hereafter discussed converter stage the power module IRAM136–3063B [35] has been chosen. The 600 V / 30 A IGBT's and reverse diodes in the module are of the type IRGP20B60KD-E [32].

Compared to a realisation of the interleaved half-bridge topology with the mentioned discrete components the concept with integrated power modules occupies 40% less space when the modules are placed horizontally on the board. Even more space can be saved when the modules are placed vertically as it is the case in the hereafter presented realisation. The IGBT's that are integrated in the modules are able to carry currents up to 30 A at a junction temperature of $T_J = 25^\circ\text{C}$. This is sufficient to handle the maximum currents of 25 A as described in the previous section. Furthermore, the pulsed current capability is 50 A per semiconductor device. The internal layout with the IGBT's and reverse diodes along with the package of the module is depicted in Fig. 2.10.

2.3.3 Switching Loss Measurements

For the dimensioning of the cooling part of the power stage it is crucial to know the switching behaviour and the thereby occurring losses of the employed power semiconductors. In order to gain these figures, switching loss measurements have been carried out. The most important part employed in these measurements is the current sensor utilised to measure

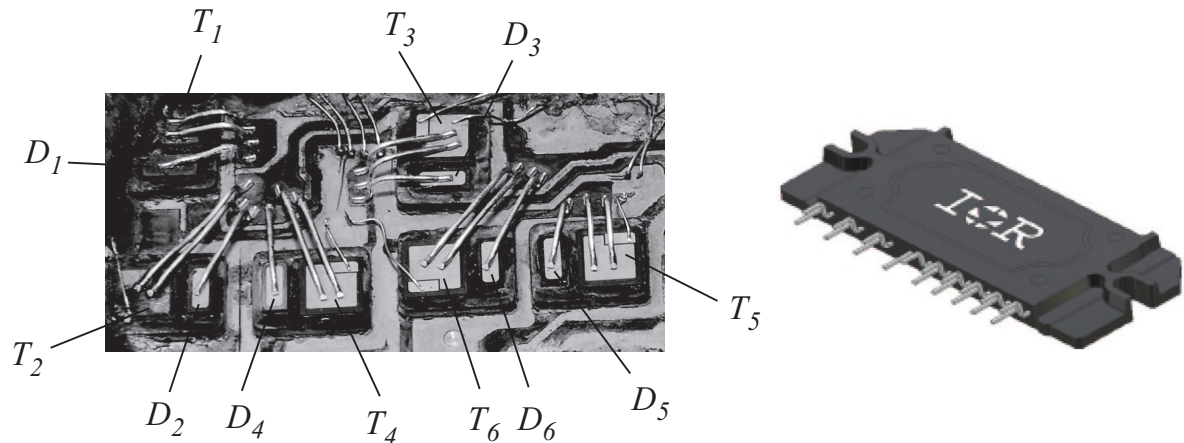


Figure 2.10: Internal layout (left) and package (right) of the power module IRAM136-3063B.

the switched current. An overview about different sensor principles suitable for the measurement of the current in switching loss measurements is given in [36]. Ideally, the sensor should have a very high frequency bandwidth. The requirements of the sensor are given by the pulse width and the slew rate of the measured current. For the hereafter presented current measurements a current transformer that is presented in [37] was used. The measurement setup is depicted in Fig. 2.11.

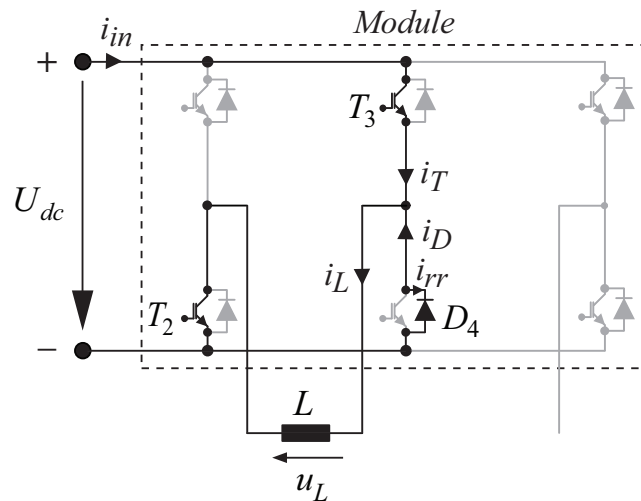


Figure 2.11: Measurement setup for the switching loss measurements. Due to symmetry reasons the loss measurements can be restricted to the transistor T_3 and the diode D_4 .

The input current i_{in} , the coil current i_L as well as the voltages

across the transistor T_3 and the diode D_4 can be measured directly at the terminals of the module, whereas the reverse recovery current i_{rr} cannot be measured directly since neither the anode nor the cathode of that device are accessible directly due to the packaging of the power module. However, for the switching loss calculations of the diode this current must be known. It is therefore calculated out of i_T and i_L according to $i_{rr} = i_T - i_L$. For the reproduction of the voltage and current relation that is occurring during operation of the converter a constant steady state current is applied to the inductor. This constant current is then switched according to the applied switching pattern to record the switching behaviour of the IGBT and the antiparallel diode. Due to symmetry reasons, the loss measurements are restricted to the transistor T_3 and the reverse diode D_4 (the grey coloured components are not involved in the switching loss measurements). These switches are always turned off while transistor T_2 is constantly turned on during the applied switching pattern. The switched current along with the relevant time instants is depicted in Fig. 2.12. During t_1 IGBT T_3 is turned on so that the full dc-link voltage of 325 V is applied to the coil L and as a result of this the current i_L is linearly increasing. The time instants t_1 and t_2 are set according to the requirement for a constant average coil current as mentioned beforehand. Care must also be taken that the oscillations in the switched current completely decay after turn on or turn off before the next switching instant occurs. At t_2 , the upper switch T_3 is turned off and as a result of this the current commutates to the diode D_4 . T_3 is turned on again at the time instant t_3 . The switching pattern is only applied twice to ensure that the power semiconductors do not heat up significantly and a junction temperature of $T_J = 25^\circ\text{C}$ can be guaranteed.

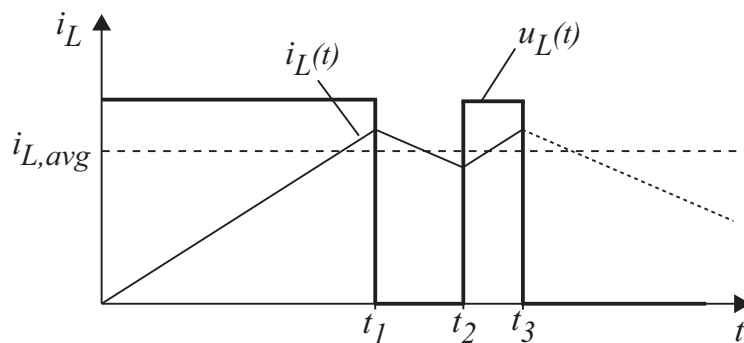


Figure 2.12: Inductor current for the evaluation of the switching losses.

The measurements for the evaluation of the switching losses have been carried out for discrete values of the switched current $i_T = [0 \ 5 \ 10 \ 15 \ 20]$ A at a junction temperature of $T_J = 25^\circ\text{C}$ and a constant dc-link voltage of $U_{dc} = 325$ V.

Switching Behaviour

The switching behaviours of the IGBT and the reverse diode in the power module Power Module IRAM136–3063B are depicted in the Figures 2.13 and 2.14.

At turn on (cf. Fig. 2.13(a)), the current commutates from the diode into the switch. The current transition occurs with 0.604 kA/ μs . During turn on, the voltage across the switch is reduced due to the voltage drop across the parasitic wiring inductances that start to carry the current. This voltage drop slightly decreases the switching stresses. From this voltage level on, the voltage u_{CE} decays during 110 ns to 0 V. After the IGBT current has reached the level of the load current, it further increases beyond that value owing to the charge in the reverse diode D_4 . After a depletion region is formed in this reverse diode, it starts to support the voltage and the charging disappears due to the recombination. This also causes the collector voltage to fall.

During the rise time of the voltage u_{CE} at turn off of the switch, the current diminishes about 4.1 A. After the voltage u_{CE} has reached the level of the dc-link voltage, the diode D_4 starts to conduct and the current impressed in the switch starts to commutate into the freewheeling diode D_4 . Thereby, the current decays almost linearly with 0.676 kA/ μs . Due to the fact that the gate resistors in the module cannot be changed, no influence can be taken on the rise time of the current and thus the losses occurring at turn on of the switch. In Fig. 2.14 the turn off behaviour of the diode D_4 is depicted. The reverse recovery peak current \hat{i}_{rr} arising during this switching instant is 13.5 A.

2.3.4 Calculation of the Losses in the Power Module

Switching Losses

The turn on and turn off loss energies E_{on} , E_{off} and E_{rr} that have been obtained with the previously described measurement setup are depicted

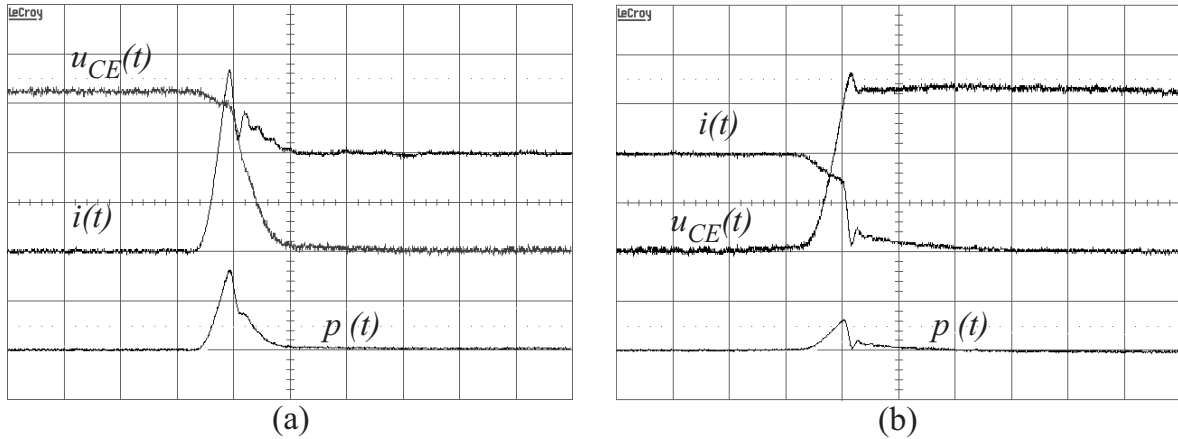


Figure 2.13: Switching behaviour of the IGBT T_3 at a junction temperature of $T_J = 25\text{ }^\circ\text{C}$, dc-link voltage $U_{dc} = 325\text{ V}$ and steady state coil current $i_L = 15\text{ A}$. (a) Turn-on and (b) turn-off of IGBT T_3 . Current scale: i : 7.5 A/div, voltage scale: u : 100 V/div, power scale p : 1 kW/div, time scale: 100 ns/div.

in Fig. 2.15. Approximating these curves with a second order polynomial function

$$E_{Sw} = k_{0,k} + k_{1,k} i_T + k_{2,k} i_T^2, \quad (2.14)$$

leads to the coefficients summarised in Table 2.2. Besides the switching coefficients of the transistors, the reverse recovery losses of the diode D_4 (cf. Fig. 2.11) have been evaluated by measurements as well and are shown in Fig. 2.15as well. For the diodes, a first order polynomial interpolation is chosen with parameters $k_{0,k}$ and $k_{1,k}$.

Due to the symmetry of the used switching pattern and the symmetrical current distribution in the semiconductors of the interleaved half-bridge (as explained in section 2.3.1) it is sufficient to integrate the loss energy of each loss term over a $\pi/2$ interval.

$$P_{Sw} = f_s \frac{2}{\pi} \int_0^{\pi/2} w(u, i) d\varphi, \quad (2.15)$$

with f_s as the switching frequency that is applied to the respective semiconductor and $w(u, i)$ the loss energy. Looking at the switching pattern in Fig. 2.7 one can see that during the $\pi/2$ -interval the following losses occur in the transistors:

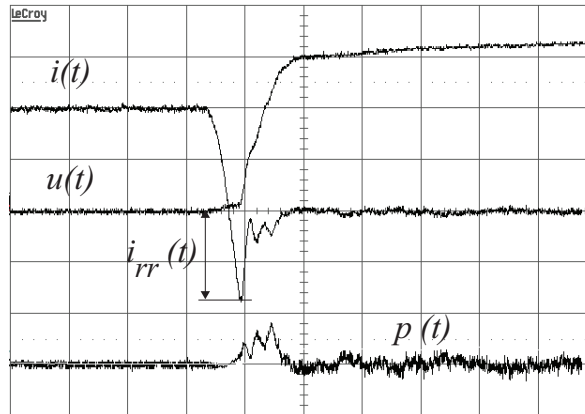


Figure 2.14: Switching behaviour of the reverse diode at a junction temperature of $T_J = 25\text{ }^\circ\text{C}$, dc-link voltage $U_{dc} = 325\text{ V}$ and steady state coil current $i_L = 15\text{ A}$. (a) Turn-on and (b) turn-off of IGBT T_3 . Current scale: i : 7.5 A/div, voltage scale: u : 100 V/div, power scale p : 1 kW/div, time scale: 100 ns/div.

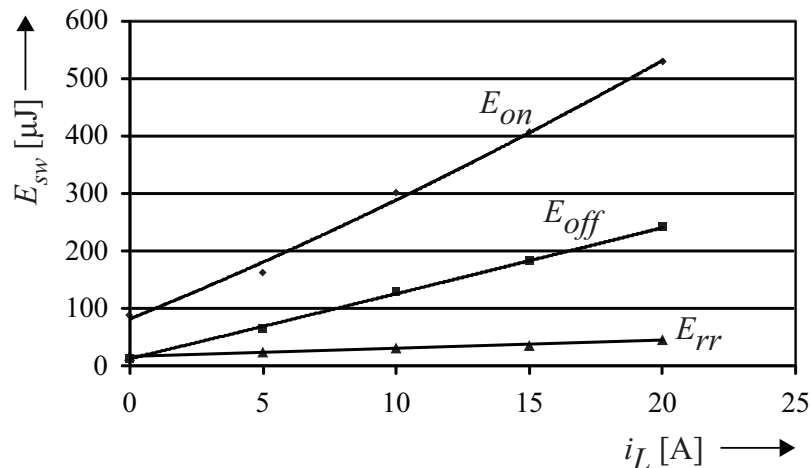


Figure 2.15: Switching loss energy of the transistor T_3 (cf. Fig. 2.11 at turn on (E_{on}) and turn off (E_{off})). And reverse recovery losses E_{rr} in the diode D_4 .

$$P_{Sw,IGBT's} = P_{sw,on,T_4} + P_{sw,off,T_1} + P_{sw,on,T_1} + P_{sw,off,T_4}. \quad (2.16)$$

This shows that turn on and turn off losses are evenly occurring in the transistors T_1 and T_4 . As explained in section 2.3.1, each transistor is involved in the switching of the phase current during two times a $\pi/2$ -interval of the phase current. Thus, the switching losses per transistor T_k

switching loss coefficients	$k_{0,k}$ [μJ]	$k_{1,k}$ [$\mu\text{J}/\text{A}$]	$k_{2,k}$ [$\mu\text{J}/\text{A}^2$]
turn on IGBT	80.8	18.9	0.180
turn off IGBT	12.5	11.3	0.007
reverse recovery Diode	17.2	1.35	-

Table 2.2: Coefficients for the loss measurements of the transistors T_k and the diodes D_k gained through switching loss measurements at a junction temperature of $T_J = 25^\circ\text{C}$.

during a full period are calculated to

$$\begin{aligned}
 P_{Sw,T_k} &= \frac{1}{2\pi} \left(\int_0^{\pi/2} (k_{on} + k_{off}) i_L(\varphi) \sin(\varphi) d\varphi \right. \\
 &\quad \left. + \int_{\pi}^{3\pi/2} (k_{on} + k_{off}) i_L(\varphi) \sin(\varphi) d\varphi \right) \\
 &= 2 f_s \frac{1}{2\pi} \int_0^{\pi/2} (k_{on} + k_{off}) i_L(\varphi) \sin(\varphi) d\varphi \\
 &= \frac{f_s}{\pi} (k_{on} + k_{off}) \hat{I}_L, \tag{2.17}
 \end{aligned}$$

where \hat{I}_L is the peak current in the phase that is connected to the respective switch. Similarly, the same losses occur in the other transistors of the separate bridge-legs while they are involved in the switching of the phase current during twice times a $\pi/2$ -interval.

For the diodes, the same loss distribution as for the transistors is valid. Also there, turn on and turn off losses occur evenly distributed over a $\pi/2$ -period of time.

$$P_{Sw,Diodes} = P_{Sw,off,D_3} + P_{Sw,on,D_2} + P_{Sw,off,D_2} + P_{Sw,on,D_3} \tag{2.18}$$

However, due to the fact that the turn on losses are insignificantly small, only the reverse recovery losses are considered hereafter. In analogy to (2.17) the switching losses per diode D_k over a full sine-period result in

$$\begin{aligned}
P_{Sw,D_k} &= 2f_s \frac{1}{2\pi} \int_0^{\pi/2} k_{rr} i_L(\varphi) \sin(\varphi) d\varphi \\
&= \frac{f_s}{\pi} k_{rr} \hat{I}_L.
\end{aligned} \tag{2.19}$$

Conduction Losses

Besides the beforehand discussed switching losses, also conduction losses occur in the semiconductors. For a profound calculation of the losses the component specific parameters $U_{CE,0}$ and r_{CE} of the IGBT and $U_{F,0}$ and r_F for the diode, respectively, have been evaluated. Their values are summarised in Table 2.3. The forward characteristics of the semiconductors can be approximated by a forward voltage drop and a forward resistance

$$P_{Fw,T_k} = U_{CE,0} I_{T_k,avg} + r_{CE,on} I_{T_k,rms}^2, \tag{2.20}$$

$$P_{Fw,D_k} = U_{F,0} I_{D_k,avg} + r_D I_{D_k,rms}^2. \tag{2.21}$$

Component	Specific parameters
Transistor T_k	$U_{CE,0} = 1.11 \text{ V}, r_{CE,on} = 0.077 \text{ m}\Omega$
Diode D_k	$U_{F,0} = 1.05 \text{ V}, r_F = 83 \text{ m}\Omega$

Table 2.3: Coefficients of the IGBT and the diode extracted from datasheets and verified by measurements at a junction temperature of $T_J = 25^\circ\text{C}$.

2.3.5 Loss Distribution

With the help of the equations 2.17, 2.19, 2.20 and 2.21 the total losses in the interleaved half-bridge topology can now be calculated. When doing this, the way of how the drive and bearing phases are connected to the bridge-legs of the modules plays an important role. The different configurations considered for the comparison of the occurring switching losses are depicted in Fig. 2.16. There, only the separate bridge-legs are shown, whereas the connection to the common bridge-leg is indicated with a dashed line. The currents in the two drive phases show a phase

shift of $\pi/2$ as outlined in 2.2.3. Illustration (a) in Fig. 2.16 shows the case where the drive system is operated by one three-phase module. This setup is referred as DD-configuration later on. The thereby resulting current in the common bridge-leg is $\sqrt{2}$ times the drive phase current as shown earlier on. Similarly, this is also the case for the bearing system (BB-configuration) (cf. Fig. 2.2.3(b)). In Schematic (c) the situation is shown, where a drive and a bearing phase with both having currents that are in phase to each other are connected to the same common bridge-leg (DB-configuration). In this case, the current in the common bridge-leg is the sum of the two phase currents.

In Fig. 2.17 the total losses in either of the discussed configurations is depicted for an impeller speed of the pump of 4,000 rpm. At this operating point, the rms drive and bearing currents are 2.5 A and 2.1 A, respectively. For a fair comparison, the duty cycles of the switches T_1 and T_2 in the common bridge leg are modulated with 50% and all switches are operated with a switching frequency of 18 kHz. The thereby achieved voltage magnitude is sufficient for a stable control of the impeller in the pump. However, the performance of the drive system suffers from this low modulation depth and only speeds up to 4,000 rpm and a resulting flow of 60 liters per minute can be obtained. This drawback can be overcome with modulation methods presented in chapter 4.

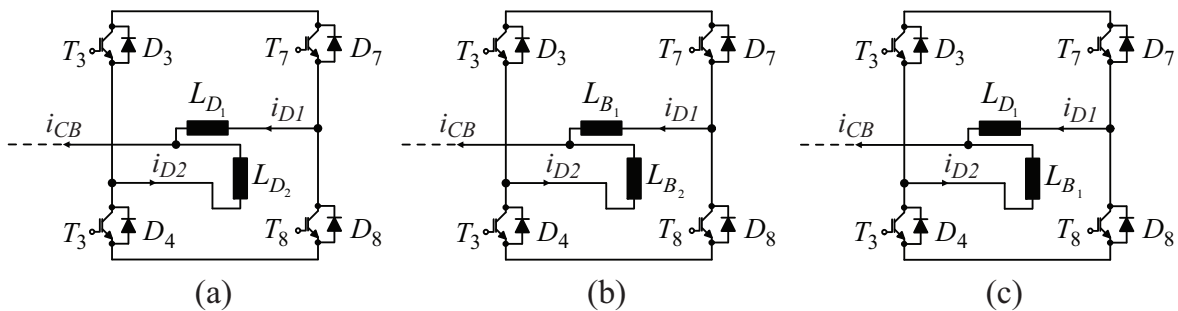


Figure 2.16: Configurations (a) drive–drive (DD), (b) bearing–bearing (BB), (c) drive–bearing (DB).

At this operating point, the losses that occur in each power module in the DB-configuration are 22.8 W. This results in a total of 45.8 W losses in both modules. The sum of the losses in the DD- (18.4 W) and BB- (15.4 W) configuration is 33.8 W. This shows that the switching losses are lowered for the same operating point of the pump by 26% when a module for the drive system and a second for the bearing phases is re-

served. A further advantage of this configuration is that a lower switching frequency for the semiconductors in the drive module can be chosen as for those involved in the control of the bearing currents. The connection of one drive and one bearing winding to the same common-bridge leg does not allow a lower switching frequency in the respective bridge legs since a switching frequency of 18 kHz is needed for a save operation of the bearing system 3.1. In case of the DD- and BB-configuration a switching frequency of 4.5 kHz for the drive system can be chosen while the bearing module is still operated with 18 kHz. Doing this results in power electronics losses caused by the drive system of 11.9 W at this operating point. This is 39.7% less than when the drive currents are switched with 18 kHz.

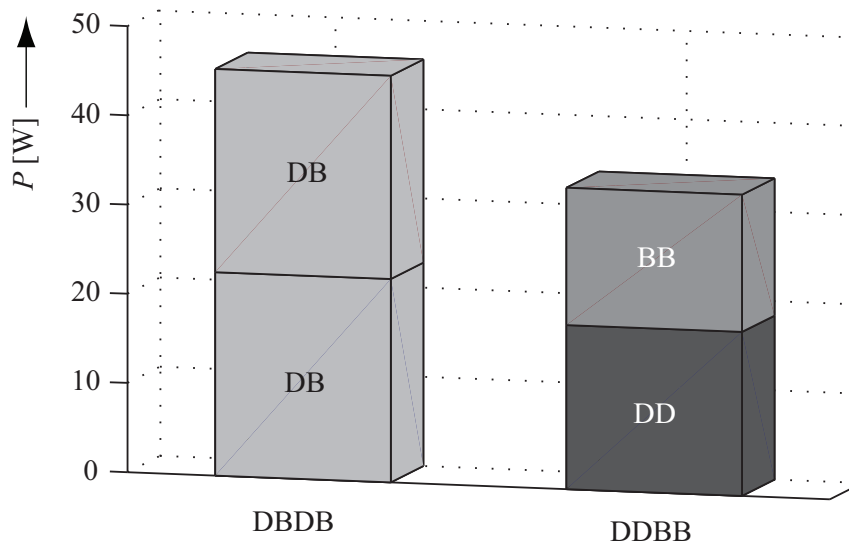


Figure 2.17: Losses in the DB and DD/BB configuration for a speed of 4000 rpm and a flow of 60 l/min at a switching frequency of 18 kHz in all switches.

In addition, the combination of the drive- and bearing- windings to a separate module offers the freedom of selection power modules with different current ratings for both systems. However, for the herein discussed quantities, the numbers are still in a range where the employment of two similar modules offers more cost advantage than combining two different modules. Furthermore, there exist two-phase bearingless motor configurations [34] with higher current ratings of the windings than those presented in this work. When connecting these drive windings to the same power module the peak current that occurs in the common-bridge leg is higher than the 30 A current rating of the modules. Thus,

a connection of the windings according to Fig. 2.16(c) has to be chosen. This implies that in order to make the hereafter presented inverter system universally applicable for various bearingless motor configurations power modules with similar current ratings must be chosen.

2.3.6 Thermal Analysis

Another aspect which is crucial for the design of the converter is the evaluation of the most suitable cooling concept. This requires the balancing of a number of conflicting parameters in order to maximise the performance of the heat sink. First of all, one has to decide whether a passive– or active– (air or water) cooling should be employed. The latter certainly results in the lowest volume and mass of the heat sink. As a matter of fact the cost of material is lowest as well. On the other hand, external equipment such as a water supply and a pump must be present. If only clean room applications would be targeted as described in chapter 1, an active water cooled system is the preferred choice since the required connectors are usually present in these facilities. However, since the aim of the herein discussed system is a universally applicable device which is independent of any supply except the power cord, a forced air cooled heat sink with a fan is chosen. The broad application range involves a wide ambient temperature range T_A within that the converter has to be safely operated. If the converter is mounted in a cabinet, ambient temperatures of up to 40 °C are present. For safety reasons and protection of the user, the maximum heat sink temperature $T_{HS,max}$ shall not exceed 70 °C.

In a first step, an adequate design procedure for the heat sink must be chosen. In recent years, mathematical models for the determination of the optimal volume and/or mass of a heat sink have become more and more into the scope of interest for power electronics designers. However, these mathematical models [38], [39] result in high computational effort. Quite often, these multi–parameter optimisation procedures also go beyond the scope of an industrial product since the manufacturing of the thereby arising tiny structures is very difficult and quite often even impossible to realise. The problem is that the optimum heat sink geometry that results in minimum thermal resistance for a given base plate size needed to attach the two power modules, usually results in very thin fins and/or very small channel widths. When aiming for a design applicable for medium size volume production an efficient manufacturing procedure

for the heat sink is crucial. Otherwise the cooling part becomes a major cost driver of the overall system.

Under all these circumstances the most cost effective solution for the heat sink is the use of extruded aluminum sheets. The thickness of the fins is thereby restricted by manufacturing constraints. In this design, it is set to 2 mm according to manufacturer data. Due to the given casing size, the maximum width and length of the fin is limited to 70 mm. Only the height can theoretically be varied up to a maximum of 25 mm. Considering this, the aim in the selection process of the fan is to maximise the fan size and thereby receiving maximum air flow. Doing this, leads to a fan with external measurements of 70x70x25 mm. The maximum air flow of the chosen fan [40] at the rated dc-voltage of 12 V is 1.73 m³/min.

In the next step, the design of the fins and the overall heat sink geometry must be carried out. In [41] an analytical optimisation procedure for a given fan is presented that takes care of this issue. Applying the respective equations to the herein occurring problem allows it to define the heat sink parameters without the necessity of time consuming numeric 3D-simulations that are otherwise necessary to systematically find an optimum design. The design of the so obtained heat sink is depicted in Fig. 2.18. The length of the base plate is 160 mm and the height is 44 mm. The fins are placed on both sides of the main frame as can be seen there. Namely, 7 fins above the power modules and 12 on the reverse side of the base plate. The thickness of the fins is 2 mm and the length 40 mm above the power modules and 20 mm on the backside, respectively. The length of the fins is given by the available space in the casing of the converter. The extrusion length of the heat sink is 160 mm as well. The heat sink is made out of aluminum with a thermal conductivity of 239 W/m°C, a density of 2700 kg/m⁻³ and a specific heat of 896 J/(kg°C).

In order to verify these heat sink parameters gained by analytical calculations a thermal simulation of the temperature distribution in the heat sink has been carried out with the fluid dynamics software *Icepak* [42] for the worst case load point of the pump system. The ambient temperature is set equal to the ambient temperature in semiconductor fabs, which is $T_A = 20$ °C. At this operating point, the *rms* current value of each drive-phase and bearing-phase is 14.2 A and 2 A, respectively. With the loss equation presented in section 2.3.4, the losses in the drive- and bearing-module can be calculated. Doing this leads to a total energy loss

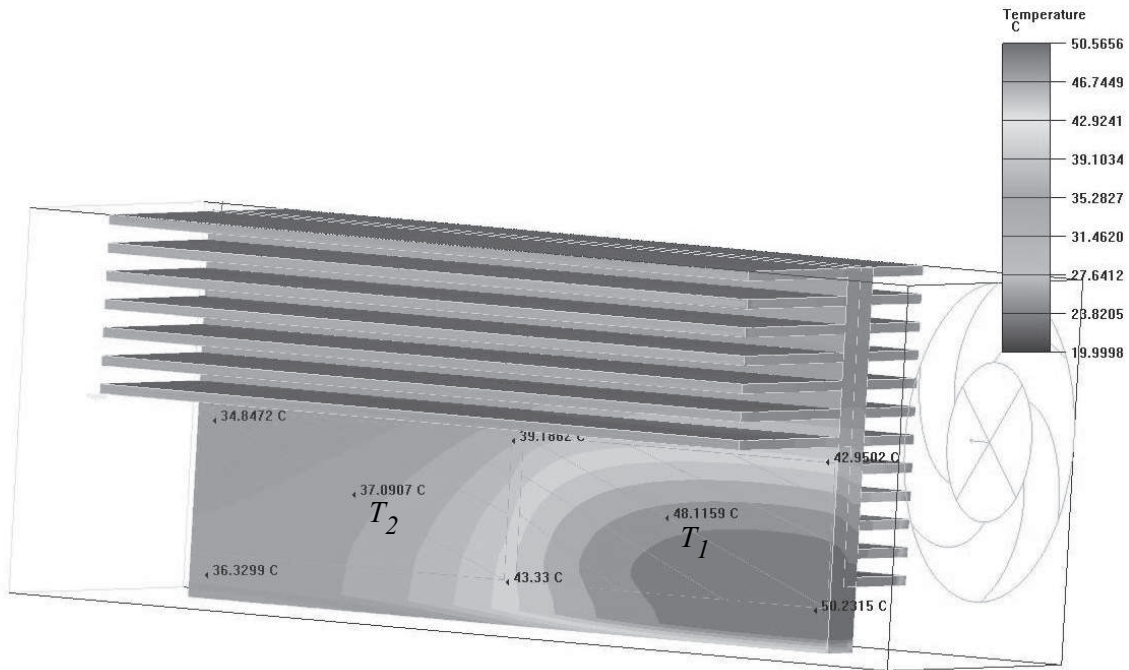


Figure 2.18: Verification of the designed heat sink with a thermal simulation.

of $P_{L,D,tot} = 128.86$ W in the drive module and $P_{L,B,tot} = 8.96$ W in the bearing module. The simulation results (cf. Fig. 2.18) reveal that these loss energies result in a heat sink temperature of $T_{HS} = 48.2$ °C in the center of the drive module and 37.2 °C case temperature in the center of the bearing module. The simplification in the simulation considering two heat sources emitting the respective loss energies is justified by the fact that setting up extremely accurate thermal models of power semiconductors does typically not make a lot of sense, since the interface between the case of the power module and the surface of the heat sink (typically thermal grease) is not well defined but contributes significantly to the thermal resistance. Nevertheless, the temperature at the junction of the semiconductor is the limiting factor that determines the applicability of the power module. Therefore, the worst case junction temperatures of the switches and diodes have to be estimated.

The power semiconductors in the common bridge–leg face the highest current stresses and as a consequence the losses and thereby the junction temperature of these elements is the highest. Thus, for the verification of the cooling concept, the junction temperature of the IGBT’s and diodes in this bridge–leg are calculated. Looking at the internal layout of the power module (cf. Fig. 2.10) reveals that the transistor diode combina-

tions T_1/D_1 and T_2/D_2 of the common bridge leg are located in the lower left corner of the drive module. In the IGBT T_2 losses of $P_{L,T_2} = 17.15$ W arise, whereas the switched current in the diode D_2 generates a loss energy of $P_{L,D_2} = 11.53$ W for a drive phase current of 14.2 A. According to the datasheet of the employed power module [35], the thermal resistance per IGBT is $R_{th,J-C,IGBT} = 1.5$ °C/W and per diode $R_{th,J-C,diode} = 2.5$ °C/W. The case to heat sink resistance is given by $R_{th,C-HS} = 0.1$ °C/W. Based on these values and assuming a worst case heat sink temperature of $T_{HS} = 50.25$ °C the junction temperature of the transistor T_2 is calculated to

$$T_{J_{T_2}} = P_{L,T_2} \cdot R_{th,J-C,IGBT} + P_{L,tot} \cdot R_{th,C-HS} + T_{HS} = 88.9 \text{ °C}. \quad (2.22)$$

Similarly, the junction temperature of the diode D_2 results in

$$T_{J_{D_2}} = P_{L,D_2} \cdot R_{th,J-C,IGBT} + P_{L,tot} \cdot R_{th,C-S} + T_{HS} = 91.98 \text{ °C}. \quad (2.23)$$

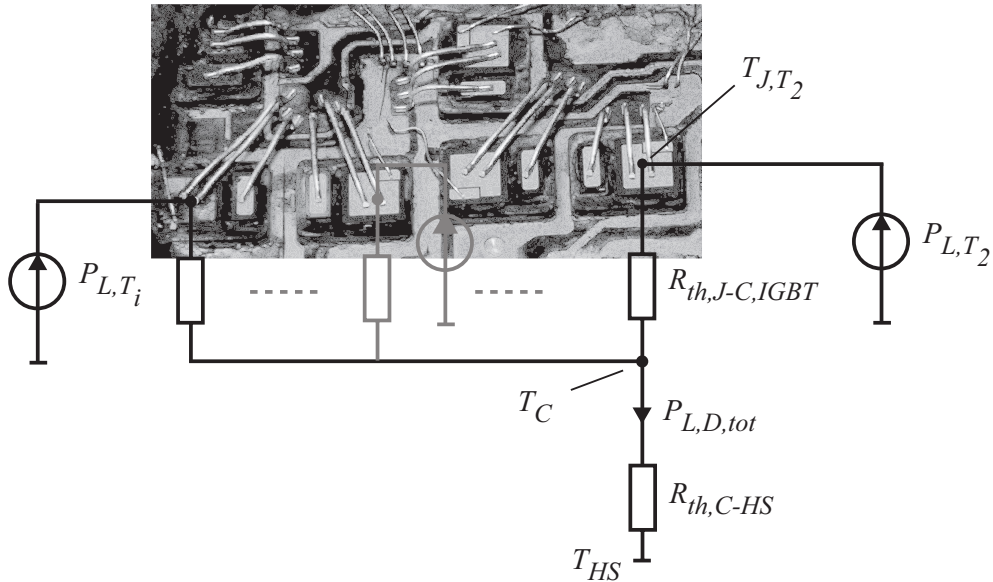


Figure 2.19: Model for the calculation of the junction temperature of the IGBT T_2 .

Considering the worst case ambient temperature of 40 °C, these results have to be shifted by a temperature offset of $T_{offset} = 20$ °C. Doing

this leads to a worst case junction temperature of the diode D_2 of $91.98\text{ }^\circ\text{C} + 20\text{ }^\circ\text{C} \approx 112\text{ }^\circ\text{C}$, which is still well below the thermal limit of $125\text{ }^\circ\text{C}$ specified in the the datasheet of the power module [35]. At an ambient temperature of $40\text{ }^\circ\text{C}$, the maximum heat sink temperature is shifted to $70.24\text{ }^\circ\text{C}$. Given the requirement for a maximum heat sink temperature of $70\text{ }^\circ\text{C}$ mentioned in the beginning, this simulation shows good agreement with the design input. In addition to this thermal simulation of the worst case operating point of the pump, a number of other load points have been verified by simulations and measurements on the laboratory prototype shown in chapter 7. As an example, the temperature T_1 (center of the drive module) and T_2 (center of bearing module) for a operating point of the pump where the drive module generates losses of 60 W and the loss energy in the bearing module is 10 W are compiled in Table 2.4.

Temperature	Simulation	Measurement
T_1	$38.7\text{ }^\circ\text{C}$	$34.3\text{ }^\circ\text{C}$
T_2	$39.2\text{ }^\circ\text{C}$	$34.9\text{ }^\circ\text{C}$

Table 2.4: Verification of heat sink design with thermal measurements for loss energies of 60 W at the measurements point T_1 and 10 W at T_2 (cf. Fig. 2.18).

2.3.7 DC–Link Capacitor

As a consequence of the passive diode rectifier the power, which is flowing from the mains to the converter is pulsating with twice (in case of single–phase mains) or six times (in case of three–phase mains) the mains frequency. The voltage measured at the output of the diode rectifier without the presence of a dc–link capacitor is fluctuating with the same frequencies depending on the mains. In order to apply a constant voltage to the drive and bearing windings a capacitor must be present in the dc–link which smoothes the voltage after the diode bridge. This capacitor also serves as energy storage device in order to comply with the voltage sag ride-through capability required for semiconductor processing equipment according to SEMI F47–0200 [43]. Furthermore, in case of a mains loss of more than 1 s not specified in [43] the capacitor has to guarantee a safe shut down of the bearing system. Otherwise the impeller could touch the housing and by that an abrasion of the coating occurs which results in a contamination of the process fluid. For the bearingless

pump system discuss in this work a 1.8 mF capacitor is required.

The power that is flowing in and out of the capacitor during one mains period is defined as

$$\Delta P = -P_0 \sin(2\omega_N t), \quad (2.24)$$

where P_0 is the steady state power demand from the mains and ω_N is the mains frequency. Assuming a constant dc-link voltage U_{dc} with only very small fluctuations under steady state operation, the current flowing in and out of the capacitor is defined as

$$i_C = -\frac{P_0}{U_{dc}} \sin(2\omega_N t). \quad (2.25)$$

The peak-to-peak value ΔU_c of the dc-link voltage fluctuation is then approximated with the integration of i_C over time:

$$\Delta U_c \approx \frac{1}{C_{dc}} \int i_C dt = \frac{P_0}{U_{dc} \omega_N C_0}. \quad (2.26)$$

Considering the beforehand mentioned operation a the single-phase mains with a minimum voltage of ($U_{dc} = \sqrt{2}200$ V), a capacitor value of $C_{dc} = 1.8$ mF and a maximum load of $P_0 = 2000$ W the maximum voltage deviation ΔU_C is calculated to

$$\Delta U_C = \frac{P_0}{U_{dc} C_0 \omega_N} = 12.5V. \quad (2.27)$$

This results in a fluctuation of 2.2 % of the dc-link voltage at steady-state operation. In case a smaller dc-link capacitor is chosen and thus a higher voltage deviation arises, additional control methods such as feed-forward control of U_{dc} in Fig. 3.6 need to be taken into consideration. Due to the mentioned voltage-sag ride-through requirements the capacitor value is given and no additional control is necessary.

The relatively large capacitor value can either be achieved by connecting several smaller capacitors in parallel or through one single capacitor. Capacitors with smaller values have the advantage that the height of their housing is lower compared to those with large capacitance values and thus would result in a favorable solution for a compact design with

given restrictions regarding the height. On the other hand, the placement of several capacitors next to each other requires more space on the board than a single capacitor with the same value does. A comparison of electrolytic capacitors considering the required board space compared to the achievable total capacitance has shown that the parallelisation of several small capacitors does not result in a more compact design. Since in the herein discussed design the space on the board is very limited whereas the height of the capacitor is not a limiting factor a single dc-link capacitor design is chosen.

2.4 Summary

In this chapter, a comparison of inverter topologies regarding their suitability for driving a bearingless two-phase pump is performed. In particular, the conventional full-bridge topology is opposed to alternatives with reduced number of components, such as the split-capacitor and the interleaved half-bridge topology. The comparison includes the number of utilized components, the maximum achievable drive voltage, additional control effort, current stresses in the power semiconductors and practical system aspects. Based on this analysis, the interleaved half-bridge topology is selected for the realisation of a next generation bearingless pump controller with a power rating of 2 kW.

A base for the design, in a first step, an analysis of the current stresses in the selected power modules has been carried out. The calculation of the losses in the power semiconductors that are depending on the chosen motor winding configuration is then shown on switching loss data which have been gained through switching loss measurements. Based on these loss calculations, the best suitable cooling concept is evaluated and out of this, a forced air cooled heat sink is designed and verified by thermal simulations and measurements.

Furthermore, the requirements for the dc-link capacitor are shown and with that, the calculation of the necessary capacitor value is carried out.

Chapter 3

Sensor and Control System

3.1 Introduction

The combination of both drive-phases to a single module and similarly also the bearing-phases to a second one allows the employment of different switching frequencies in each module as outlined in the previous chapter. As a result of this, the losses in the system can be minimised. In this chapter, the control requirements of both systems and resulting conditions for the switching frequencies are discussed and weighted based on their critical influence on a stable operation of the system. Furthermore, the approach of minimising the cost for the current measurement by using hall effect based current sensor IC's is discussed and their influence on the control bandwidth is shown. Based on these considerations, the switching frequencies of the drive and the bearing systems are defined.

3.2 Current Sensor

As outlined in chapter 1.1.4, the overall cost reduction approach of a bearingless pump system also addresses the current measurement method. The current in each phase that is connected to the separate bridge leg is measured with one current sensor (cf. Fig. 3.1). In total, four sensors are employed to measure the respective phase currents.

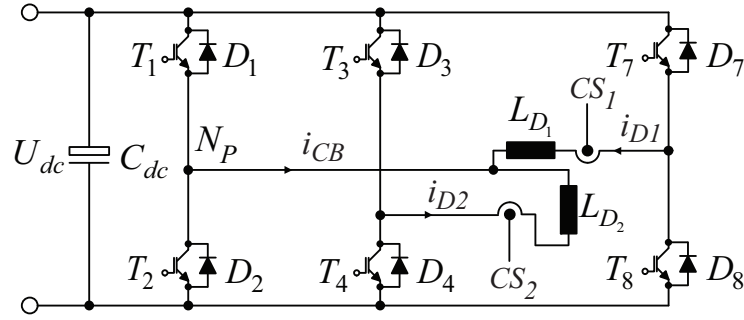


Figure 3.1: Location of current sensors in the interleaved half-bridge.

In today's systems, high-quality current sensors with a bandwidth up to 200 kHz are employed. These high performance components clearly result in higher cost compared to alternative concepts. And even more, bandwidths of 200 kHz are not necessarily required for the stable control of bearingless pump systems if the bandwidth of the controller can be significantly lower. The resulting phase delay of the low bandwidth current sensors and its impact on the selection of the control frequency is therefore investigated in this chapter.

In [44] an overview on current sensing technologies for very compact power electronics is given with the aim of lowering the cost and achieving compatibility with manufacturing processes. One approach a more cost effective design would be the application of current shunts which work on the principle of the ohmic voltage drop. However, since the voltage measured across such a shunt is in reference to the ground potential of the power stage, additional effort must be taken for the realisation of the potential separation between the shunt potential and the ground potential of the remaining sensor electronics which is in interaction with the user and thus has to be electrically isolated from the power stage due to safety restrictions.

An alternative concept to the employment of shunts are sensor IC's that measure the magnetic field based on the hall effect [45]. These devices can be applied to both dc and ac current sensing up to hundred kHz. The output signal of these sensors is electrically isolated from the measured signal. Thus, no additional components for the potential separation are needed. Due to its compact design and attractive price, these sensors are the favorable concept for the current measurement in next generation bearingless pump systems. However, compared to magneto resistive current sensor with a response time below $0.15 \mu s$, hall effect

current sensors have the disadvantage of relatively large delay times. For the hereafter employed current sensor of the type Allegro ACS712 [46], a propagation delay time of $t_{delay} = 3 \mu s$ has to be taken into consideration for the design of the current controller.

The modelling of the current sensor behaviour is realised with a delay time and a PT1 element for the signal rise. Given the rise time from 10% to 90% of $6.6 \mu s$ specified in the datasheet, the corresponding time constant for a rise of the output signal from 0 to 63% requested by the PT1 element is $\tau_{CS} = 3 \mu s$. With this, the current sensor is modeled as:

$$G_{CS}(s) = e^{-s t_{delay}} \frac{1}{1 + s \tau_{CS}} \quad (3.1)$$

The exponential transfer function is thereby approximated by a rational transfer function using Padé approximation [47]. The bode plot and step response of this transfer function are shown in Fig. 3.2 and 3.3, respectively.

The implemented phase response of the applied current sensor has also been verified by measurements (cf. Fig. 3.4). As can be seen there, the measurements show very good agreement with the simulations. Therefore, this transfer function of the current sensor can be used for the analysis of the current control loop,.

3.3 Drive System

From the viewpoint of minimising the losses in the power module of the drive system, the switching frequency of the IGBT's in that module should be selected as low as possible. However, a trade-off arises between lowering the losses while ensuring an accurate current control. In order to ensure full performance it is necessary that the currents are sampled with a sampling frequency being high enough. Due to the variable permeability of the drive inductance, high currents, which arise due to high torque demand, lead to saturation and thereby over currents if a too low sampling rate is chosen and the currents cannot be controlled accurately enough. To avoid this, at least ten sampling points within one half sine period have to be acquired (cf. Fig. 3.5).

Furthermore, as outlined in section 1.1.3, the output pressure of bear-

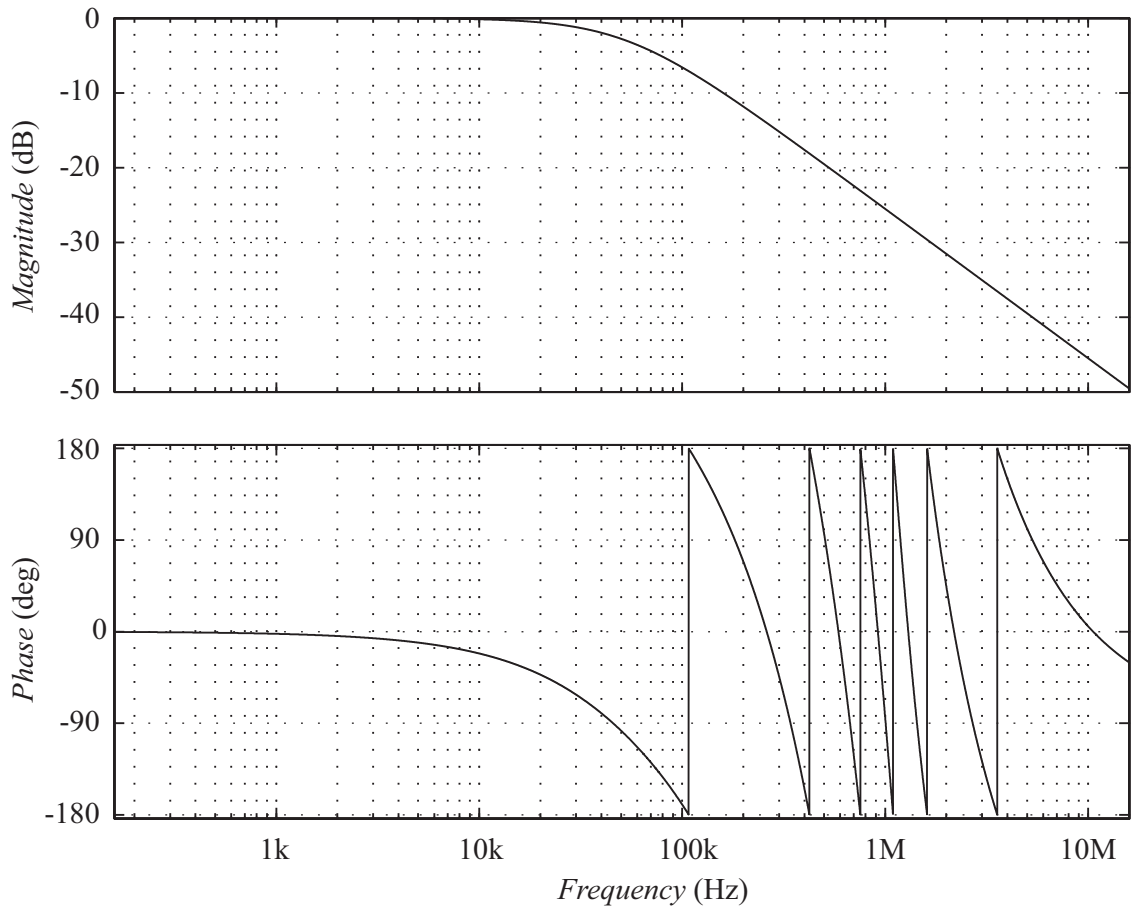


Figure 3.2: Bode plot of the current sensor model $G_{CS}(s)$ with $t_{rise,CS} = 6.6 \mu s$ and $t_{delay,CS} = 3 \mu s$.

ingless pumps in semiconductor applications has been increased in the upcoming years. This has a direct impact on the speed of the impeller, since the output pressure of a centrifugal pump scales with n^2 (4.2). According to these forecasts, rotational speeds up to 12,000 rpm are demanded in the near future for the pump size at hand. This implies a maximum mechanical frequency of

$$f_{m,max} = \frac{12000 \text{ rpm}}{60 \text{ s}} = 200 \text{ Hz.} \quad (3.2)$$

Combining 3.2 with the minimum rate of 20 samples per full sine period results in a minimum sampling frequency of the drive current of

$$f_{I,D,min} = f_{m,max} \cdot 20 = 4 \text{ kHz.} \quad (3.3)$$

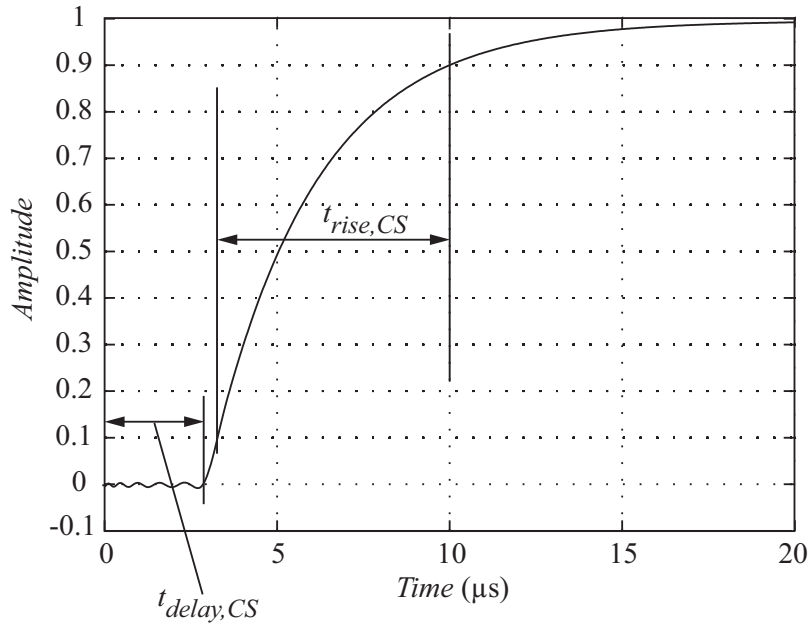


Figure 3.3: Step response of the current sensor model $G_{CS}(s)$ with a rise time of $t_{rise,CS} = 6.6 \mu s$ and a response delay of $t_{delay,CS} = 3 \mu s$.

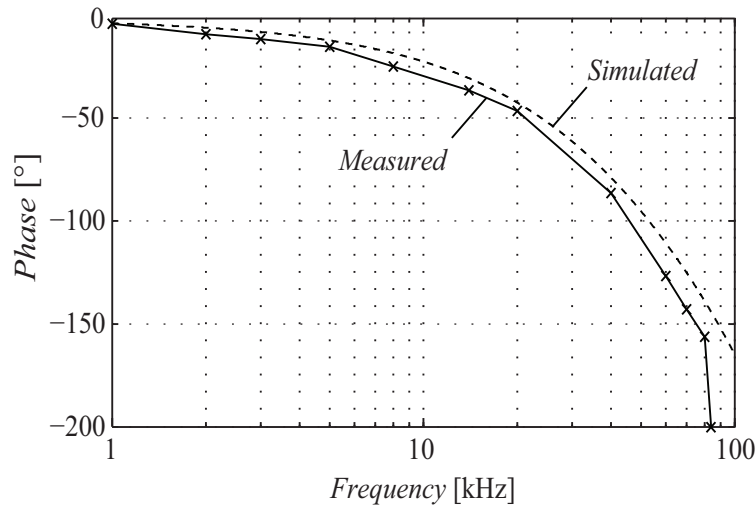


Figure 3.4: Phase difference of the current sensor.

With this, the minimum sampling time of the drive current is given by

$$t_{Sample,D,min} = \frac{1}{f_{I,D,min}} = 250 \mu s. \quad (3.4)$$

The acquisition of the drive currents is triggered by an interrupt that

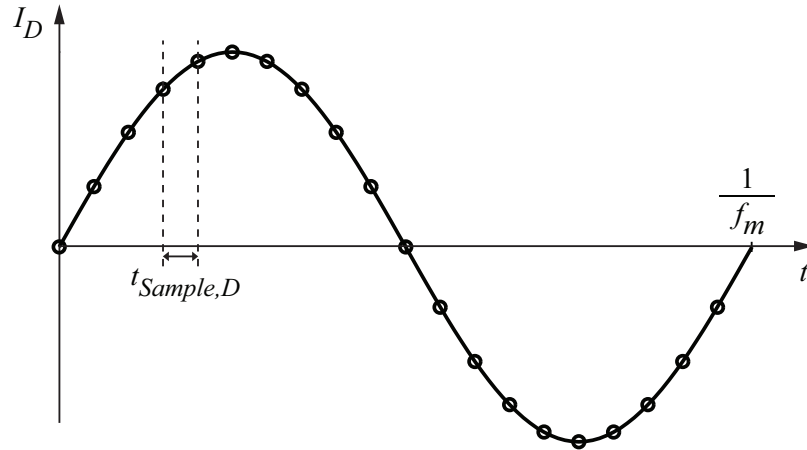


Figure 3.5: Minimum number of sample points within one period of the drive phase current with the mechanical frequency f_m and the sampling time $t_{Sample,D}$.

correlates with every switching instant of the drive system. Hence, the minimum switching frequency of the IGBT's involved in the control of the drive current has to be set to 4 kHz.

3.4 Bearing System

For the selection of the switching frequency of the bearing–system, multiple parameters must be considered. First, the mechanical time constant of the system gives an indication of the critical timing issues of the position control. For a stable system operation, the bandwidth of the position controller must be at least equal to the inverse value of the mechanical time constant of the bearing–system which is defined as

$$\tau_M = \sqrt{\frac{m_I}{k_{R,B}}}, \quad (3.5)$$

where m_I is the mass of the impeller and $k_{R,B}$ the radial stiffness that specifies the required radial force F_R needed to return the rotor back to its stable position after being displaced by 1mm. For the herein employed motor [48] the radial stiffness is $k_{R,B} = 25.97$ N/mm and the mass of the impeller is $m_I = 434$ g. With this, the mechanical time constant results in $\tau_M = 4.1$ ms.

According to the before mentioned criteria, the bandwidth of the position controller has to be at least $1/4.1 \text{ ms} = 244 \text{ Hz}$. On the other side, the electrical time constant of the bearing current controller

$$\tau_E = \sqrt{\frac{I_{B,max} \cdot L_B}{U_{cl,B,max}}}, \quad (3.6)$$

gives an indication of the minimum control bandwidth of the current controller. With the values of $I_{B,max} = 1.5 \text{ A}$ as the maximum bearing current, $L_B = 55 \text{ mH}$ as the bearing inductance and $U_{cl,B,max} = \sqrt{2} \cdot 230 \text{ V}$, as the maximum applicable clamp voltage to the bearing phase, the electrical time constant results in $\tau_E = 0.5 \text{ ms}$. As shown in [49], for achieving a stable system control the condition

$$\tau_E \ll \tau_M \quad (3.7)$$

has to be satisfied in the design of a magnetic bearing system. Applying (3.5) and (3.6) for the already existing design of the two-phase motor (1.1.1) reveals that $\tau_M = 8.2 \cdot \tau_E$. Thus, 3.7 is fulfilled. As a matter of fact in cascaded control schemes the subordinate current-controller has to be about five times faster than the overlying position controller whose minimal bandwidth is given by τ_M . With this, the minimal bandwidth of the current controller is given by $5 \cdot 244 \text{ Hz} = 1.22 \text{ kHz}$. For the hereafter presented design of the control loop, the bandwidth of the current controller is set to

$$BW_{CC} = 1.2 \text{ kHz}. \quad (3.8)$$

The control structure of the bearings system is comprised of a position controller and an underlying current controller as shown in Fig. 3.6. Herein, the delay time of the current sensor presented in the previous section has a direct influence on the control bandwidth. Thus, this issue will be analysed in the following. The overlying position control is presented in detail in [2] and will not be further investigated in this work.

The linear transfer function of one bearing phase is given by

$$G_{BNG} = \frac{1}{1 + sL_B/R_B}. \quad (3.9)$$

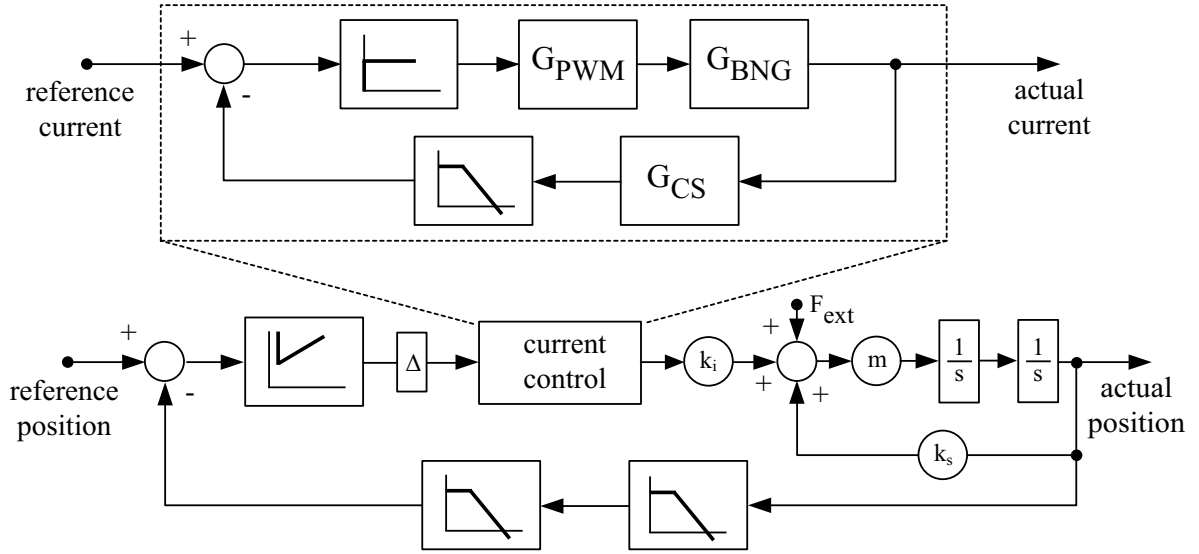


Figure 3.6: Control structure of the position and current controller.

Due to its first order integral behaviour, the bearing system results in a phase shift of -90° as can be seen in the bode plot in Fig. 3.7. With a desired control bandwidth of 1.2 kHz a proportional gain controller $G_P = k_P$ with a gain of

$$k_P \geq 10^{\frac{52.4dB}{20dB}} = 417 \tag{3.10}$$

is required.

This shows that -90° phase shift have to be added by the subsequent transfer functions in the open loop chain to guarantee a stable system. For a stability analysis, additional delays occurring in the system, which lead to a lower phase margin, have to be analysed.

The interrupts of the control system are generated by a timer that is counting up and down as shown in Fig. 3.8. At every minimum and maximum of the timer value an interrupt is triggered. These interrupts are occurring with twice the switching frequency:

$$f_I = \frac{1}{T_I} = 2 \cdot f_s. \tag{3.11}$$

When the timer reaches its minimum value, the PWM register of the DSP is written to the respective output pin and thereby a new duty cycle is applied after every pulse interval

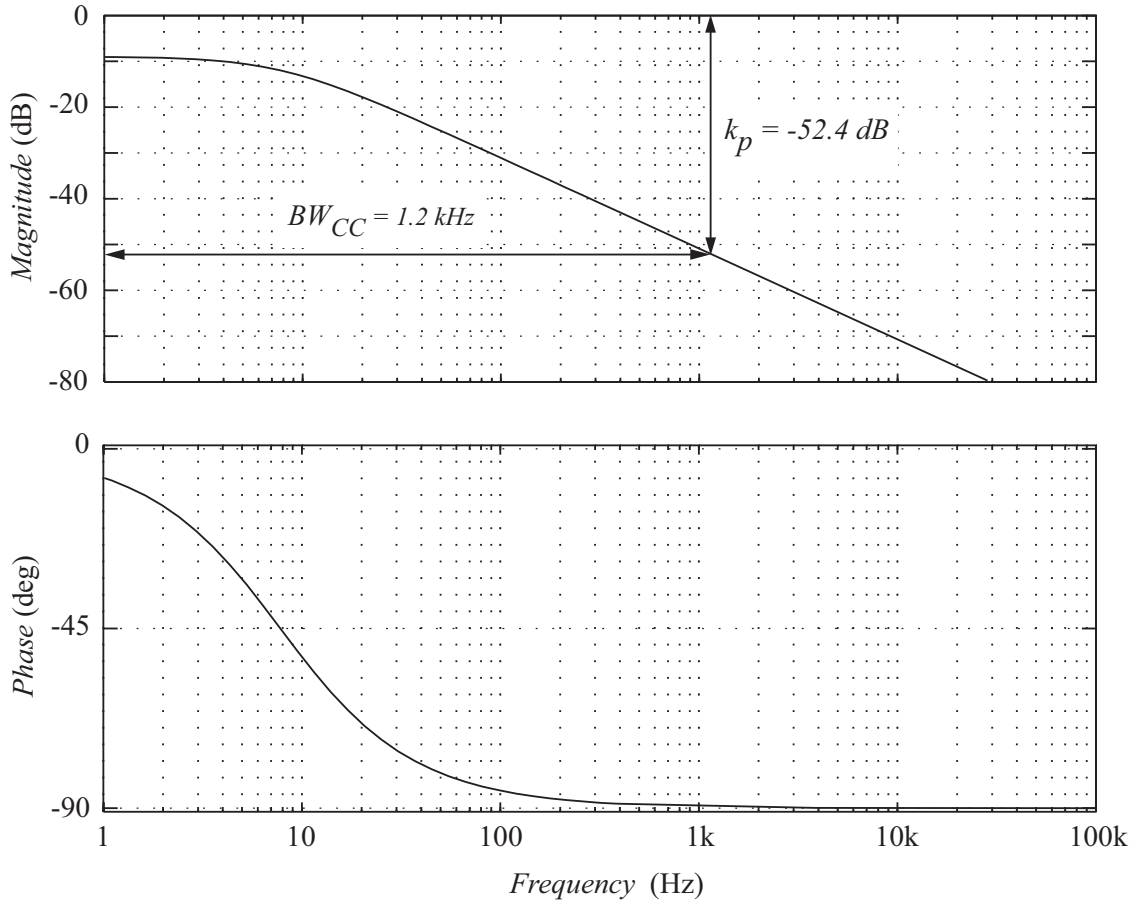


Figure 3.7: Bode diagram of the bearing plant with $L_B = 55 \text{ mH}$ and $R_B = 2.67 \Omega$.

$$T_P = 1/f_s. \quad (3.12)$$

In average, the PWM output is delayed by $3 \cdot T_P/2$. In Fig. 3.8 it is shown that the delay is caused by one interrupt period resulting of the calculation and hold time of the new duty-cycle until it is written to the respective output pin. The PWM is updated only once per pulse period and thus, an additional delay of $T_P/2$ is caused until the new value is active [50].

With that, the total delay, which is depending on the switching frequency, can be written as

$$G_{PWM} = e^{-s 3T_p/2} = e^{-s 3T_I} \quad (3.13)$$

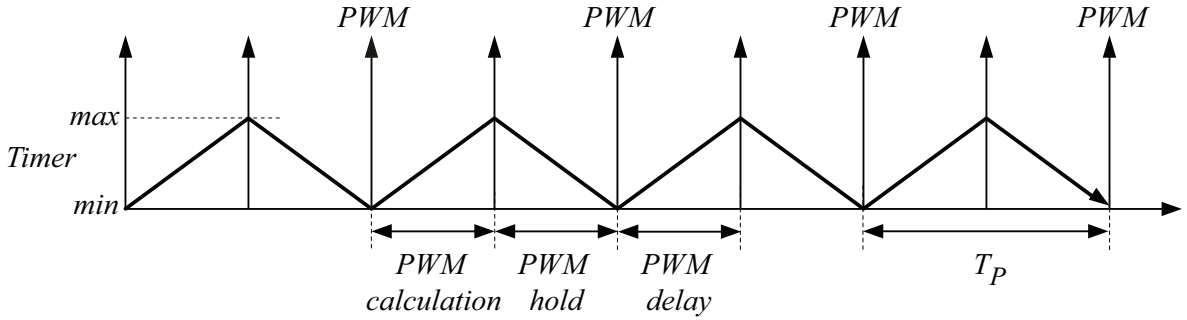


Figure 3.8: Interrupt generation.

For the analysis of this time delay, different switching frequencies will be taken into consideration. The lowest switching frequency in this analysis is chosen to be 4.5 kHz, which equals the minimum allowed switching frequency of the drive system calculated in the previous section. Furthermore, the behaviour at a switching frequency of 9 kHz and 18 kHz is investigated (cf. Fig. 3.9).

As outlined earlier on, the bearing phase already contributes -90° phase shift which influences the stability of the system. Looking at the bode plot in Fig. 3.9 reveals that at 1.2 kHz the PWM delay with a switching frequency of 4.5 kHz results in additional -134° phase shift and thus already leads to an unstable system. A switching frequency of 9 kHz contributes a phase shift -67.4° and thereby to a stable system when only this delay is considered in combination with the bearing plant. However, only 22.6° phase shift are reserved for the current sensor and the low-pass filter in this case. Increasing the switching frequency to 18 kHz reduces the phase shift to -33.7° and thereby allows certain margin for the subsequent transfer functions.

Besides the phase margin as a stability criteria of the open loop system, for the current control, the overshoot behaviour of the closed loop system is of major interest as well. Thereby, the goal is to minimise the overshoot if a unit step is applied to the closed loop system. The coherence between the phase margin of the open loop system in the frequency domain and the overshoot of the closed loop system in the time domain is given according to [51] by a simple approximation

$$\Delta h[\%] = 70 - \Delta\varphi[^\circ]. \quad (3.14)$$

Here, Δh is the maximum overshoot of the closed loop system in %

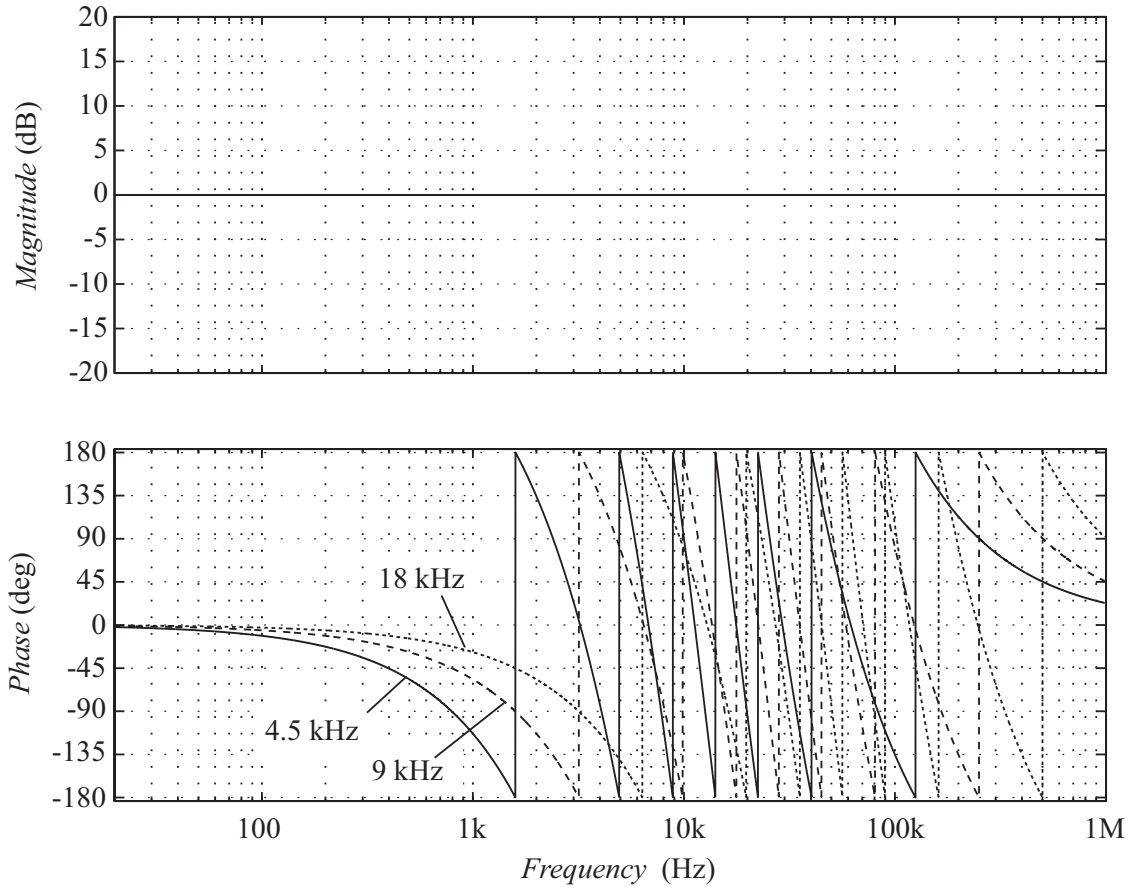


Figure 3.9: Bode plot of the delay of the PWM signal according to 3.13 for switching frequencies of $f_s = [4\ 9\ 18]$ kHz.

of the unit step and $\Delta\varphi$ is the phase margin at the frequency point of interest. This shows, that a phase margin close to 70% must be targeted in order to achieve a system without overshoot.

Due to the relatively high noise level in a bearingless pump system, the output signal of the current sensor must be filtered. The bandwidth of this filter is a trade-off between filtering of the noise and maximising the phase margin of the open loop system. For the here employed bearingless pump system, a first order low-pass filter with a transfer function

$$G_{LP} = \frac{1}{1 + s \frac{1}{2\pi f_{c,LP}}} \quad (3.15)$$

and a cut off frequency of $f_{c,LP} = 8.8$ kHz is chosen. With this, all components of the open loop transfer function G_{OL} are known and it can

be written as

$$G_{OL} = G_P \cdot G_{PWM} \cdot G_{BNG} \cdot G_{CS} \cdot G_{LP}. \quad (3.16)$$

For a stability analysis, the phase margin of the open loop system must be considered. The respective bode plot for the switching frequencies 4.5 kHz, 9kHz and 18 kHz is shown in Fig. 3.10. Here again, one can see that choosing a switching frequency of 4.5 kHz results in an unstable system.

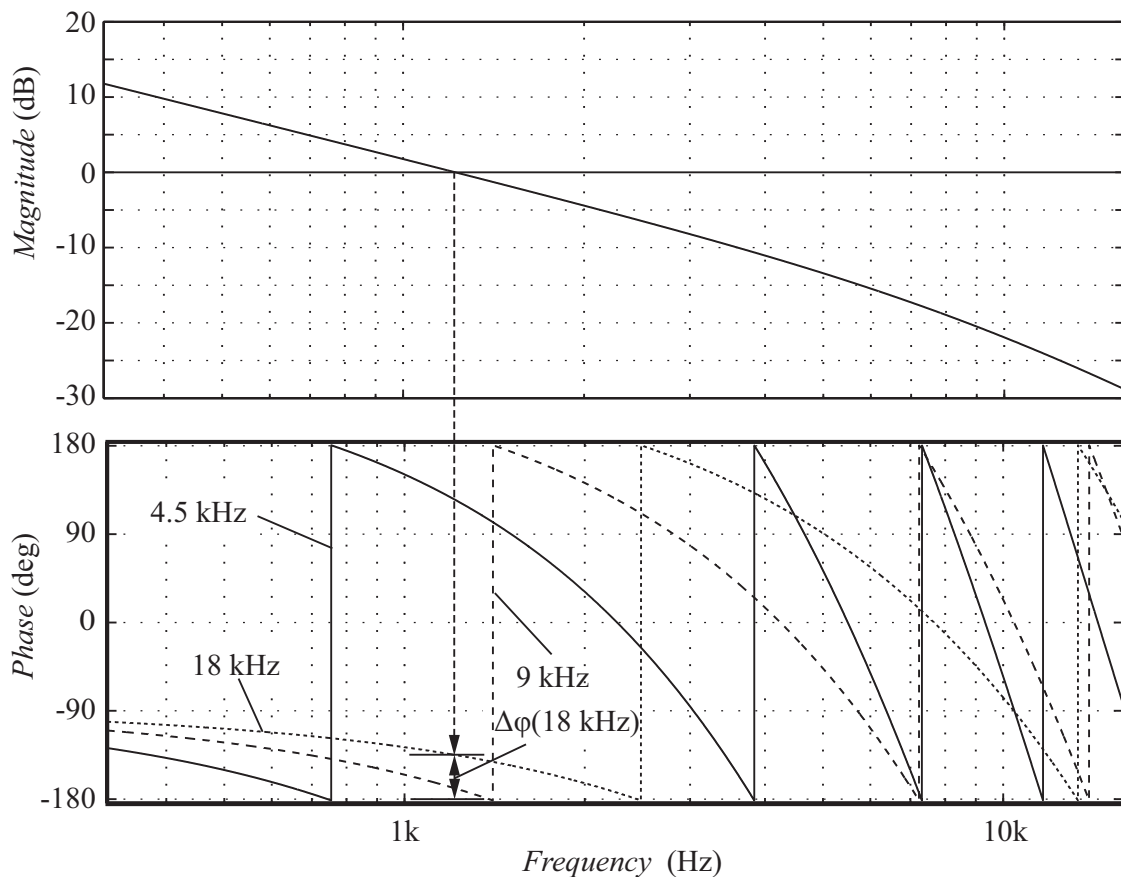


Figure 3.10: Bode plot of the open loop transfer function G_{OL} for switching frequencies $f_s = [4.5 \ 9 \ 18]$ kHz.

Taking into account 3.14, still an overshoot of

$$\Delta h[\%] = (70 - 46)[^\circ] = 24\% \quad (3.17)$$

results for a switching frequency of 18 kHz. This is illustrated in Fig. 3.11.

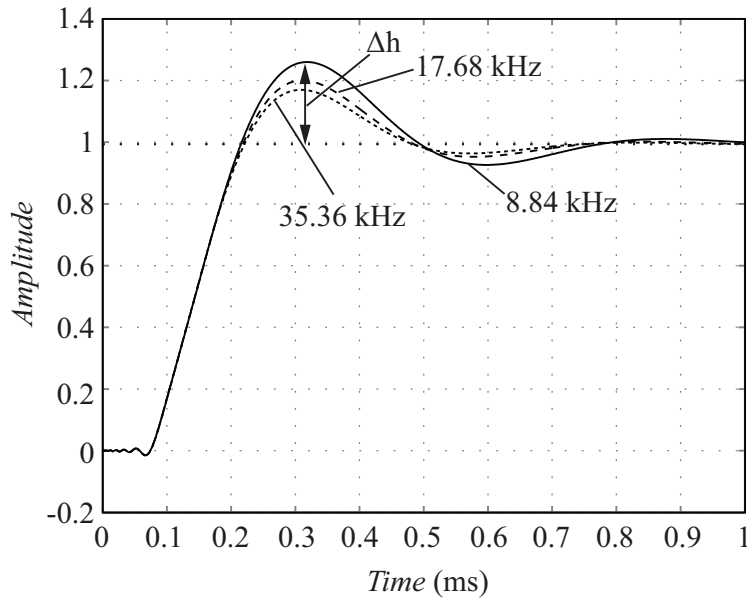


Figure 3.11: Step response of the closed loop system in dependency of the cut-off frequency of the low-pass filter.

As can be seen there, the overshoot is reduced by 7.7% if a low-pass filter with a cut-off frequency of 35.36 kHz is used. This leads to the conclusion that a switching frequency of at least 18 kHz must be selected for the bearing-system.

3.5 Software

In the following, a brief overview about the software routines necessary for the control of a bearingless slice motor system shall be given. Based on this, the control sequence of the routines depending on the selected switching frequencies is shown. The software is divided into four main routines. Namely:

- Control of bearing current and position (BNG)
- Control of drive current (DRV)
- Speed control (RPM)
- Control of additional tasks (AUX)

As mentioned in the introduction of this chapter, the control structure of a two-phase bearingless slice motor with its elements (low-pass filter, PI-controller, PID-controller) and the field- and stator-oriented coordinate transformations are presented in [2] and are therefore not further investigated in this work.

BNG The routine BNG comprises the overlying position controller and the underlying bearing-current controller. When this routine is called, in a first step, the actual rotor angle is acquired. Its value is required for the transformation of the bearing currents from the stator- into the rotor-coordinate system [2]. Similarly, it is used for the backward transformation of these currents into the stator-coordinate system after their calculation has been carried out. Subsequent to this, for the control of the impeller position, the actual rotor position must be gained by reading in the values of the position sensors. Based on this information, the calculation of both bearing currents is obtained with a PID-controller as shown in Fig. 3.6. In a next step, the output values of the bearing current sensors are acquired. Based on the required current values calculated by the position controller and the information gained by the current controller, the latter sets the duty-cycle for the switches so that the required voltages can be applied to the bearing coils.

DRV The control of the drive currents is analogue to that of the bearing currents except the fact that the overlying speed control is realised in a separate routine which is being called by a different interrupt. The output values of the hall sensors are read into the DSP and based on this, the actual rotor angle is calculated. Following this, the output values of the drive current sensors are acquired. The control of these currents is obtained with a PI-controller. Only the q-component, which equals the torque current, is of interest in a bearingless slice motor system (see section 5.3.2). The calculation of the reference value of this current component is carried out in the separate routine RPM. The d-component is set to zero since no field-weakening [52] is desired. As described in section 2.2.3, the deployment of the interleaved half-bridge topology (cf. Fig. 2.3) implies the necessity for advanced modulation schemes in order to achieve full performance of the bearingless slice motor system. This provokes an increase in the required calculation time of this routine.

Among these routines, the TQM method (see section 4.4.1) takes longest to compute the duty-cycles, namely $24.45 \mu\text{s}$.

RPM In the routine RPM, the speed of the impeller is controlled based on subsequent rotor angle values. The output of this PI-controller is the torque current desired to obtain the demanded speed. This value then serves as the reference current for the PI-controller in the routine DRV.

AUX AUX fulfills various non periodical tasks such as the observation of the dc-link voltage and the heat-sink temperature, the communication with external devices and several other tasks that consume very little time. Thus, this routine is not critical in terms of the overall timing.

Routine	calculation time
BNG	$16.75 \mu\text{s}$
DRV	$24.45 \mu\text{s}$
RPM	$3.61 \mu\text{s}$
AUX	various

Table 3.1: Execution times of the software routines.

These routines are invoked by system interrupts. As outlined earlier on, the control of the bearing system is more time critical than that of the drive system. The system interrupts are triggered at the time instants of the highest switching frequency in the system, namely that of the bearing-system. The calculation times of these routines are summarised in Table 3.1. Their timing schedule is depicted in Fig. 3.12. In the therein shown case, the DRV-routine is triggered with half the frequency of the bearing routine. However, as shown in the previous section, the drive routine can even be called by one fourth of the occurrence of the bearing routine with regard to lowering the losses.

The measured calculation times withing this timing schedule are shown in Fig. 3.13. Looking at these figures reveals that the calculation of the DRV-routine takes longest, namely $24.45 \mu\text{s}$. Assuming that due to additional calculations necessary for additional modulation methods this time varies by approximately 10%, a maximum interrupt time of $26.9 \mu\text{s}$ must be considered. This results in a interrupt time of $53.8 \mu\text{s}$ and with

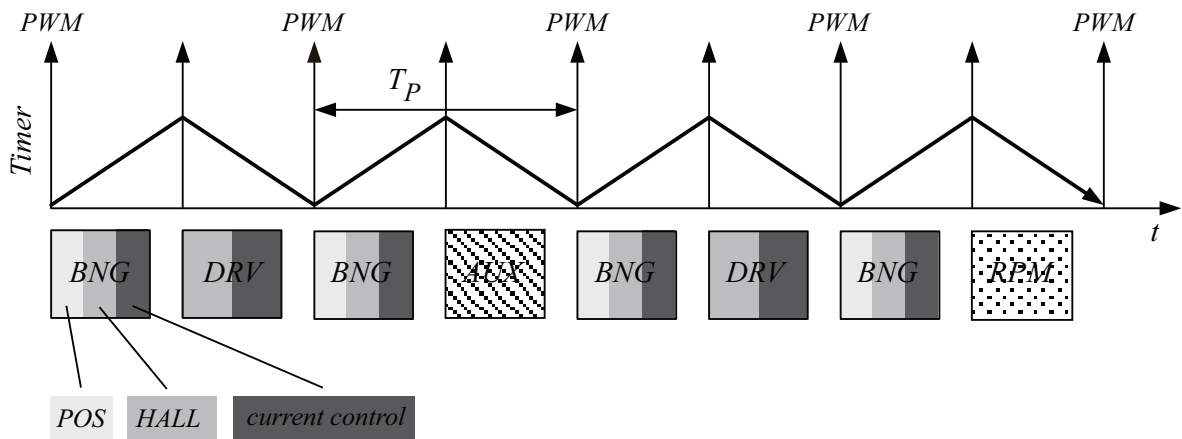


Figure 3.12: Timing schedule of the different software routines.

that to a maximum interrupt frequency of 18.6 kHz. Given this figure, the switching frequencies for the herein investigated system are selected to $f_{s,B} = 18$ kHz for the bearing system and $f_{s,D} = 4.5$ kHz for the drive system.

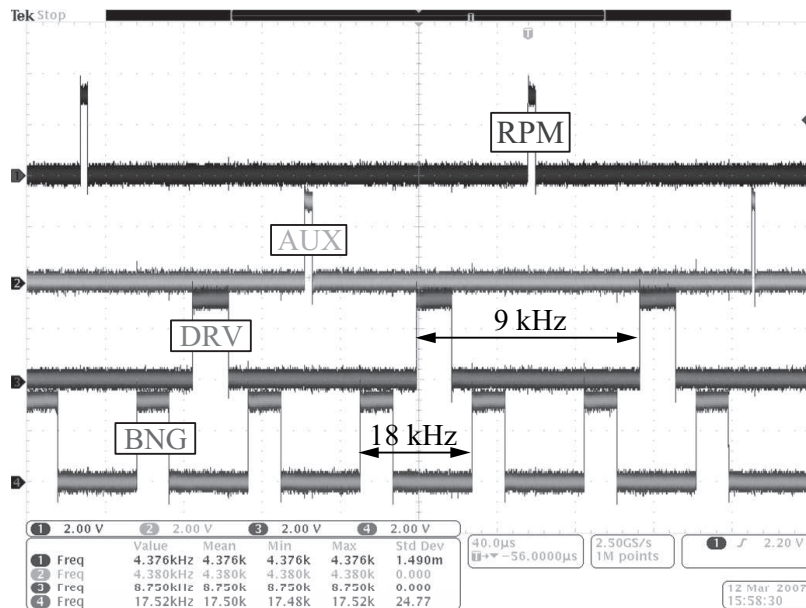


Figure 3.13: Execution times of RPM- ($3.61\mu s$), AUX-, DRV- ($18.19\mu s$) and BNG- ($16.75\mu s$) routine.

Chapter 4

Modulation Methods

4.1 Introduction

One of the drawbacks that came up in chapter 2 is that the interleaved-half-bridge does only allow half of the dc-link voltage to be applied to the drive phases in case the common bridge-leg is operated with a constant duty-cycle of 50%. To overcome this drawback of a lack of performance of the motor compared to an operation with the full-bridge topology (cf. Fig. 2.2.1) this chapter deals with different modulation methods for the interleaved half-bridge topology (cf. Fig. 4.1) for the control of a bearingless slice motor and their eligibility to increase the peak drive power of the motor. This is especially relevant in applications, such as the ones in the semiconductor industry, where the same performance is required with the future volume and cost optimised pump systems as with today's configurations. In a first approach, a basic modulation with lowest control effort is presented. Then, alternative modulation methods with superposed harmonics are characterised in order to provide higher modulation depth and therefore better motor performance. In literature, the addition of higher harmonics to the output waveforms of an inverter in conjunction with a motor is intensively considered under the aspect of lowering the losses and thereby minimising the overheating of the motor as well as reducing the vibrations in the motor [53],[54],[55]. In pumps, the delivered fluid contributes to the cooling of the motor and an evacuation of the heat arising due to losses in the motor is achieved without

the need of additional cooling. However, this is not the case for high temperature fluid applications in the semiconductor industry. But for the handling of fluids with ambient temperature or even actively cooled substances the focus can be lied on the maximisation of the achievable drive power by the addition of higher harmonics rather than on minimising the losses in the pump. The latter would result in lowering the range of potential applications for the pumps and thereby reducing the modulation depth. A further issue that has to be taken care of in conventional motors are vibrations. This, however, also has minor influence on the correct operation and the altering of a bearingless motor since no stiff connection between the rotor and stator is present. The following discussion of different modulation schemes concentrates on the drive system since its requirements regarding the modulation range are higher compared to the bearing system. However, the considerations are also valid for the modulation of the voltages applied to the bearing coils.

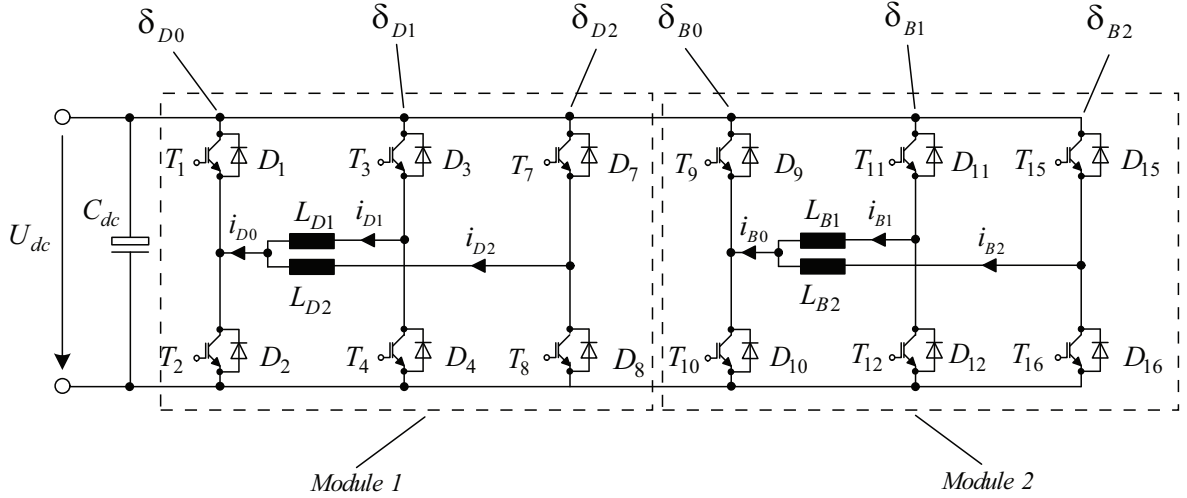


Figure 4.1: Interleaved half-bridge topology with two common bridge-legs for the two drive (L_{D1} , L_{D2}) and bearing (L_{B1} , L_{B2}) systems. Also the drive (i_{D1} , i_{D2}) and bearing currents (i_{B1} , i_{B2}) are shown.

The average voltages $\bar{u}_{D1}(t)$ and $\bar{u}_{D2}(t)$ of the drive coils are defined as

$$\begin{aligned}\bar{u}_{D1}(t) &= U_{dc} \cdot (\delta_{D1} - \delta_{D0}) = M \cdot U_{dc} \cdot \cos(\omega t) \\ \bar{u}_{D2}(t) &= U_{dc} \cdot (\delta_{D2} - \delta_{D0}) = M \cdot U_{dc} \cdot \cos(\omega t),\end{aligned}\quad (4.1)$$

where the modulation depth m is defined as

$$M = \frac{\bar{u}_{max}}{U_{dc}} = 0 \dots M_{max}, \quad (4.2)$$

with $M_{max} = 0.95$. This corresponds to the maximum value allowed to ensure a safe operation of the system.

Moreover, U_{dc} stands for the dc-link voltage and δ_{D0} , δ_{D1} and δ_{D2} are the duty cycles applied to the upper switches in each bridge-leg of the drive module (cf. Fig. 4.1). The duty cycles of the lower switches are then given by $(1 - \delta_{Di})$ with $i = 1, 2, 3$. In the following, only the expression δ_{Di} is used to describe the duty cycles of the bridge-legs. Furthermore, \bar{u}_{max} is the maximum value of the average voltage (local average value over one pulse period) at the junction point of a bridge-leg. Analogously, the duty cycles δ_{B0} , δ_{B1} and δ_{B2} are applied to the upper switches of the bearing module in Fig. 4.1. The interleaved half-bridge converter is operated with unipolar modulation as it is described in section 1.1.1.

4.2 Constant Common Bridge Leg Modulation (CCM)

In this basic modulation scheme, the duty cycle δ_{D0} of the common bridge-leg is kept constant at $\delta_{D0} = 0.5$. This leads to an average potential of $U_{dc}/2$ at the connection point of the two windings. In addition, the duty cycles δ_{D1} and δ_{D2} are sinusoidally modulated with

$$\begin{aligned} \delta_{D1} &= \frac{1}{2} + \frac{M}{2} \cos(\omega t) \\ \delta_{D2} &= \frac{1}{2} + \frac{M}{2} \sin(\omega t). \end{aligned} \quad (4.3)$$

This can be seen in Fig. 4.2. Furthermore, the resulting voltages $\bar{u}_{D1}(t)$ and $\bar{u}_{D2}(t)$

$$\begin{aligned} \bar{u}_{D1}(t) &= \frac{M}{2} \cdot U_{dc} \cos(\omega t) \\ \bar{u}_{D2}(t) &= \frac{M}{2} \cdot U_{dc} \sin(\omega t), \end{aligned} \quad (4.4)$$

along with the currents $i_{D0}(t)$, $i_{D1}(t)$ and $i_{D2}(t)$ of the two drive windings are depicted in Fig. 4.2 as well. It can be seen that the maximum average voltage across a drive coil obtainable with the described modulation scheme is given by

$$\bar{u}_{D,max,SC} = M_{max} \cdot \frac{U_{dc}}{2}. \quad (4.5)$$

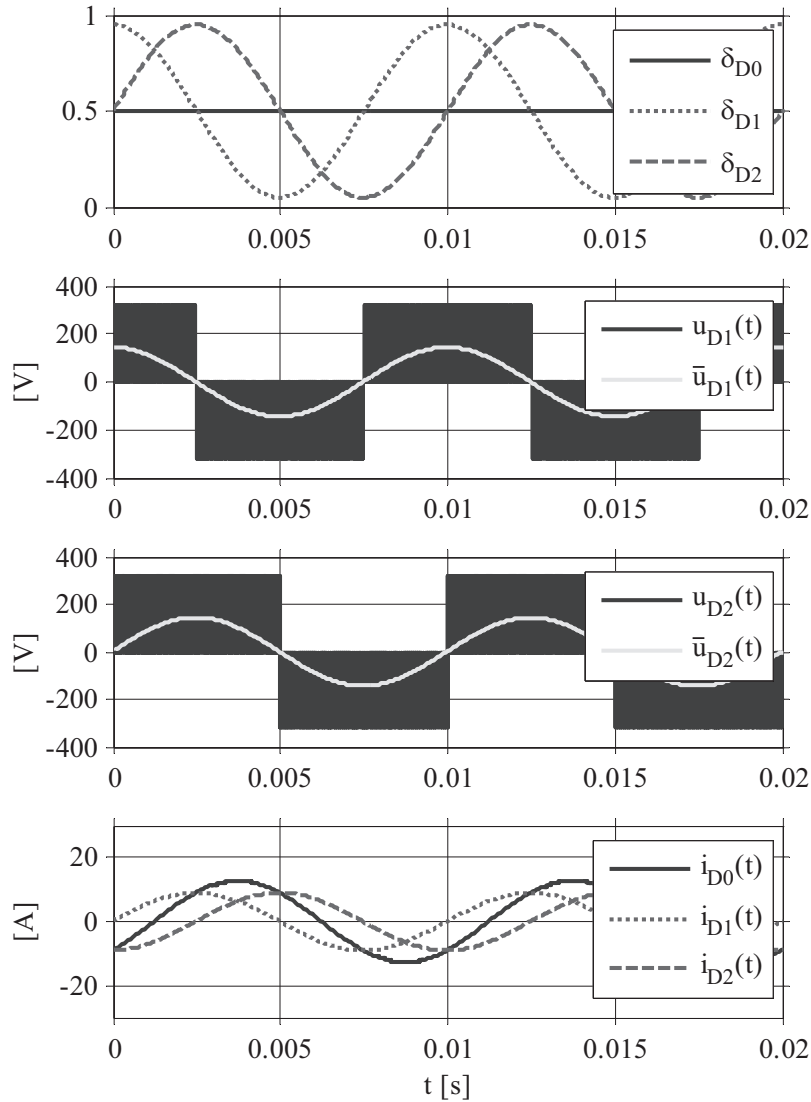


Figure 4.2: Simulation results for constant common bridge-leg modulation (CCM). Duty cycles δ_{D0} , δ_{D1} and δ_{D2} , switched voltage u_{D1} and average voltage \bar{u}_{D1} across coil L_{D1} , switched voltage u_{D2} and average voltage \bar{u}_{D2} across coil L_{D2} and currents i_{D0} , i_{D1} and i_{D2} of the drive system.

Compared to the conventional modulation of the full-bridge topology

where the full dc-link voltage is constantly applied to the drive coils the voltage is reduced by a factor 2. Hence no improvement compared to the split capacitor topology is achieved. Especially for the drive system, where high voltages across the coils are needed in order to deliver high pump power, this performance decrease is unacceptable. According to literature [56], [57], [58], the hydraulic power P_{hydr} of a centrifugal pump is given by the product of the output pressure Y and the output flow Q :

$$P_{hydr} = Y \cdot Q. \quad (4.6)$$

Based on the scaling properties of centrifugal pumps the hydraulic power is also quadratically depending [59] on the speed n and the diameter d of the impeller:

$$P_{hydr} \propto d^2 \cdot n^2. \quad (4.7)$$

Taking into consideration that an existing two-phase bearingless motor shall be operated with these modulation methods, the diameter of the impeller as well as any geometry of the pump cannot be changed. This shows that it is mandatory to find a way to increase the speed of the impeller in order to increase the performance of the pump compared to the level achievable with the CCM method. Additional modulation methods must therefore be developed in order to increase the hydraulic power of the pump.

4.3 Sinusoidal Common Bridge Leg Modulation (SCM)

An increased modulation ratio is achievable for the drive system if the duty cycle δ_{D0} of the power switch T_1 (cf. Fig. 4.1) in the common bridge-leg is varied sinusoidally. For the calculation of the required duty cycle it is assumed that the gate signals of all switches are phase shifted by the angle φ_0

$$\delta_{D0} = \frac{1}{2} + \frac{M}{2} \sin(\omega t + \varphi_0), \quad (4.8)$$

and that δ_{D1} and δ_{D2} are symmetrically distributed with respect to

δ_{D0} by the angle $\Delta\varphi$:

$$\begin{aligned}\delta_{D1} &= \frac{1}{2} + \frac{M}{2} \sin(\omega t + \varphi_0 - \Delta\varphi) \\ \delta_{D2} &= \frac{1}{2} + \frac{M}{2} \sin(\omega t + \varphi_0 + \Delta\varphi)\end{aligned}\quad (4.9)$$

A symmetrical distribution of δ_{D1} and δ_{D2} vs. ωt is chosen due to the fact that the same modulation depth for both drive windings is desired. In the following, the calculation of the optimal values of φ_0 and $\Delta\varphi$ for highest modulation depth is presented. Substituting δ_{Di} with $i = 0, 1, 2$ in (4.1) with (4.8) and (4.9) results in the following expression for $\bar{u}_{D1}(t)$

$$\bar{u}_{D1}(t) = M U_{dc} \sin\left(\omega t + \varphi_0 - \frac{\Delta\varphi}{2}\right) \sin\left(-\frac{\Delta\varphi}{2}\right) \stackrel{!}{=} \hat{U} \cos(\omega t). \quad (4.10)$$

In an analogue manner $\bar{u}_{D2}(t)$ can be calculated to:

$$\bar{u}_{D2}(t) = M U_{dc} \sin\left(\omega t + \varphi_0 + \frac{\Delta\varphi}{2}\right) \sin\left(\frac{\Delta\varphi}{2}\right) \stackrel{!}{=} \hat{U} \sin(\omega t). \quad (4.11)$$

Applying the trigonometric legality that $-\cos(\alpha) = \cos(\alpha + \pi)$ to (4.10) and solving it for φ_0 leads to

$$\varphi_0 = \frac{\Delta\varphi}{2} - \pi, \quad (4.12)$$

whereas the combination of (4.11) with $\cos(\alpha) = \sin(\alpha + \pi/2)$ results in

$$\Delta\varphi = \frac{\pi}{2}. \quad (4.13)$$

With this, φ_0 can now be calculated to

$$\varphi_0 = -\frac{3\pi}{4}. \quad (4.14)$$

Eq. (4.8) and (4.9) can then be combined with (4.13) and (4.14). Doing this leads to the following expressions for δ_{D0} , δ_{D1} and δ_{D2}

$$\begin{aligned}
\delta_{D0} &= \frac{1}{2} + \frac{M}{2} \sin\left(\omega t - \frac{3\pi}{4}\right) = \frac{1}{2} - \frac{M}{2} \cos\left(\omega t - \frac{\pi}{4}\right) \\
\delta_{D1} &= \frac{1}{2} + \frac{M}{2} \sin\left(\omega t - \frac{5\pi}{4}\right) = \frac{1}{2} - \frac{M}{2} \sin\left(\omega t - \frac{\pi}{4}\right) \\
\delta_{D2} &= \frac{1}{2} + \frac{M}{2} \sin\left(\omega t - \frac{\pi}{4}\right) = \frac{1}{2} + \frac{M}{2} \sin\left(\omega t - \frac{\pi}{4}\right), \tag{4.15}
\end{aligned}$$

and for $\bar{u}_{D1}(t)$ and $\bar{u}_{D2}(t)$:

$$\begin{aligned}
\bar{u}_{D1}(t) &= \frac{M}{\sqrt{2}} U_{dc} \cos\omega t \\
\bar{u}_{D2}(t) &= \frac{M}{\sqrt{2}} U_{dc} \sin\omega t \tag{4.16}
\end{aligned}$$

With this, the new duty cycles δ_{D1} and δ_{D2} are phase shifted by π while the angle between the winding currents $i_{D1}(t)$ and $i_{D2}(t)$ remains $\pi/2$ (cf. Fig. 4.3 (left)). As can be seen in Fig. 4.8, the voltages across the drive coils achievable with the SCM scheme are increased by a factor of $\sqrt{2}$ ($= +41\%$) as compared to the CCM method (cf. Fig. 4.3(left)).

In Fig. 4.4 it is shown how the duty cycles δ_{D0} , δ_{D1} and δ_{D2} of the SCM method can be calculated out of the duty cycles δ_{D0} , δ_{D1} and δ_{D2} of the CCM method by an analog implementation.

4.4 Harmonic Injection

Following the concept of the SCM method discussed in the previous section, additional higher harmonics can be superposed to the common bridge-leg duty cycle in order to further increase the modulation depth. In a first approach, a third harmonic is superposed to a purely sinusoidal duty cycle. This provides a higher utilisation of the dc-bus voltage. The amount of the third harmonic and the fundamental component is chosen so that the latter is maximized while ensuring that the peak-to-peak amplitude does not exceed the maximum allowed modulation depth. The corresponding average duty cycle is depicted in Fig. 4.6(b). With this, the

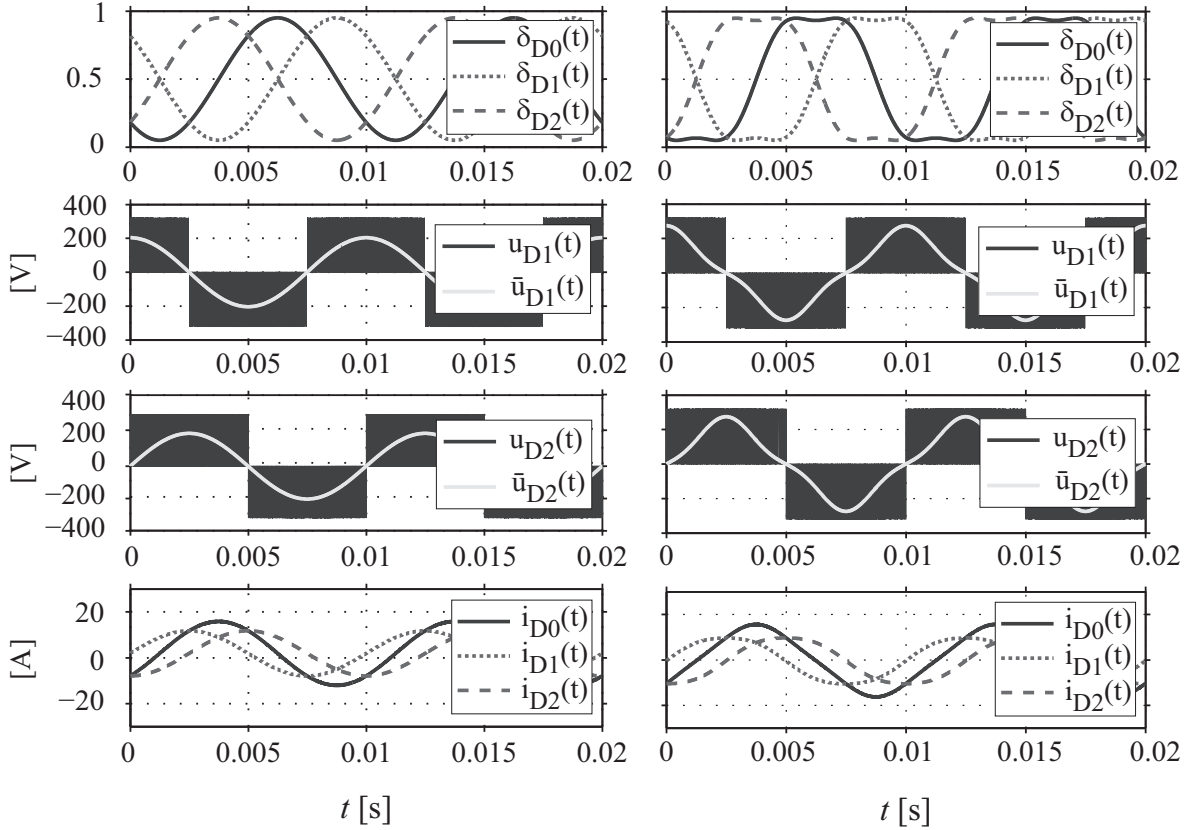


Figure 4.3: Simulation results for (left) sinusoidal common bridge-leg modulation (SCM) and (right) third harmonic modulation (THM). Duty cycles δ_{D0} , δ_{D1} and δ_{D2} , switched voltage u_{D1} and average voltage \bar{u}_{D1} across coil L_{D1} , switched voltage u_{D2} and average voltage \bar{u}_{D2} across coil L_{D2} and currents i_{D0} , i_{D1} and i_{D2} of the drive system.

voltage–time product is increased compared to purely sinusoidal modulation. Adding additional higher harmonics to the sinusoidal fundamental subsequently leads to a full square wave as it can be seen in the waveform Fig. 4.6(d).

4.4.1 Third Harmonic Modulation (THM)

Applying the previously discussed concept of the superposition of a third harmonics to each of the duty cycles, while keeping the same phase shift as it is defined for SCM, leads to another modulation concept denominated as third harmonic modulation (THM). Considering the before mentioned limitation that the peak–to–peak amplitude does not exceed the maximum allowed modulation depth leads to the following equation

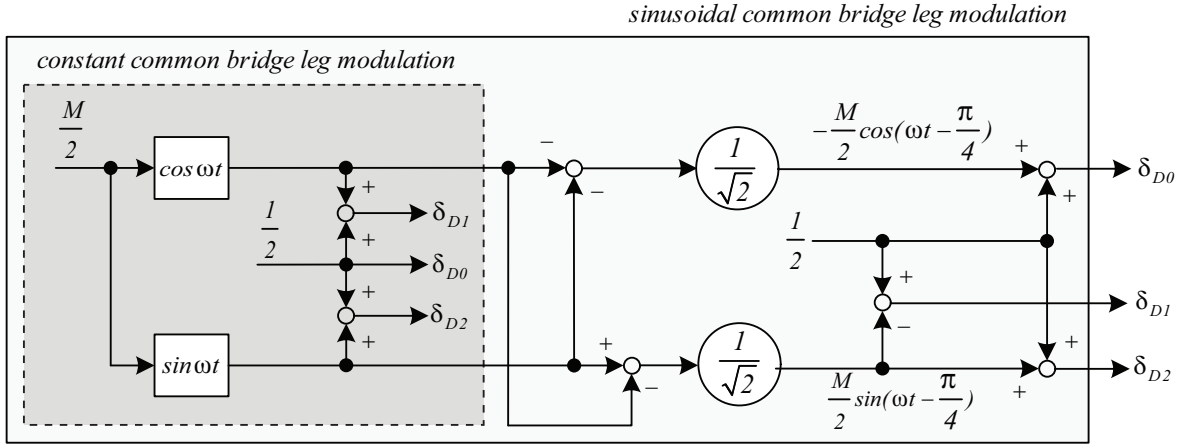


Figure 4.4: Analog implementation of the sinusoidal common bridge–leg modulation with resulting duty cycles δ_{D0} , δ_{D1} and δ_{D2} .

of the duty–cycle δ_{D0} :

$$\max(\delta_{D0}) = \max\left(\frac{1}{2} - A \frac{M}{2} \cos\left(\omega t - \frac{\pi}{4}\right) + m B \sin(3\omega t + C)\right) = m. \quad (4.17)$$

Solving (4.17) for A, B and C leads to $A = \frac{2\sqrt{2}}{\sqrt{3}}$, $B = \frac{1}{6\sqrt{3}}$ and $C = -\frac{3\pi}{4}$.

With this, the duty cycle δ_{D0} of the common bridge–leg is calculated to:

$$\delta_{D0} = \frac{1}{2} - \frac{M}{\sqrt{3}} \cos\left(\omega t - \frac{\pi}{4}\right) + \frac{M}{6\sqrt{3}} \cos\left(3\omega t - \frac{3\pi}{4}\right) \quad (4.18)$$

Similarly, the duty cycles δ_{D1} and δ_{D2} result in:

$$\begin{aligned} \delta_{D1} &= \frac{1}{2} - \frac{M}{\sqrt{3}} \sin\left(\omega t - \frac{\pi}{4}\right) + \frac{M}{6\sqrt{3}} \sin\left(3\omega t + \frac{\pi}{4}\right) \\ \delta_{D2} &= \frac{1}{2} + \frac{M}{\sqrt{3}} \sin\left(\omega t - \frac{\pi}{4}\right) - \frac{M}{6\sqrt{3}} \sin\left(3\omega t + \frac{\pi}{4}\right). \end{aligned} \quad (4.19)$$

The duty cycle, voltage and current waveforms for the THM method

are shown in Fig. 4.3 (right). Compared to CCM the first harmonic of the drive voltage is increased by a factor of $2\sqrt{2}\sqrt{3}(= +63\%)$. A drawback of this control technique clearly is that the currents in the windings are not sinusoidal anymore. This issue will be addressed further in section 4.5.1.

4.4.2 Square Common Bridge Leg Modulation (QCM)

For this modulation method and unlike the previously presented modulation schemes for the QCM, the duty cycle of the common bridge-leg δ_{D0} is of rectangular shape (cf. Fig. 4.5 (left)) with the same phase shift π as it has been used for THM and SCM.

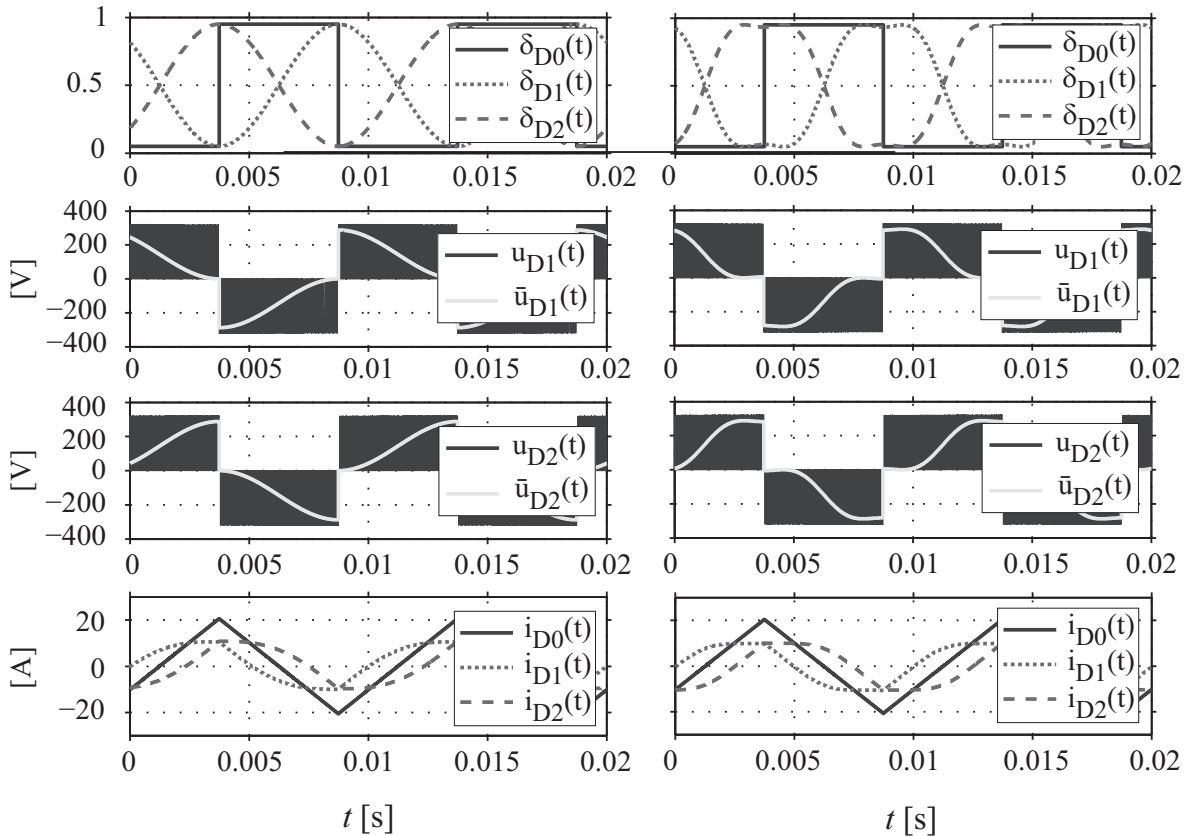


Figure 4.5: Simulation results for (left) QCM and (right) TQM with duty cycles δ_{D0} , δ_{D1} and δ_{D2} , switched voltage u_{D1} and average voltage $\bar{u}_{D1}(t)$ across coil L_{D1} , switched voltage u_{D2} and average voltage $\bar{u}_{D2}(t)$ across coil L_{D2} and currents i_{D0} , i_{D1} and i_{D2} of the drive system.

This modulation of the common bridge-leg represents the maximum

quantity of superposed higher harmonics which leads to a full square wave. The average duty cycles δ_{D1} and δ_{D2} are sinusoidally modulated and show a phase shift of $\pi/2$. The maximum amplitude of the fundamental harmonic of the applied drive voltage is increased by 62% compared to the one achieved with CCM.

4.4.3 Third Harmonic and Square Common Bridge Leg Modulation (TQM)

A further increase in the maximum current amplitude can be achieved when combining the idea of the THM and the QCM. This leads to a square wave modulation of the duty cycle in the common bridge δ_{D0} while superposing third harmonics to the sinusoidal fundamental of the duty cycles δ_{D1} and δ_{D1} as it is depicted in Fig. 4.5(b). With this modulation scheme the fundamental drive voltage is increased by 72% compared to CCM.

Different from the modulation schemes discussed before the duty cycle can be limited to the maximum applicable modulation depth over a certain amount of time (e.g. 120°) while it is increasing/decreasing at the beginning/end of a half period (Fig. 4.6(c)). In this case, the duty cycle δ_{D0} of the common bridge-leg is modulated according to:

$$\delta_{D0} = \begin{cases} \frac{1}{2} - m \cos(\omega t - \frac{\pi}{4}) & \text{if } 0 \leq \omega t \leq \pi/6 \\ \frac{1}{2} + \frac{M}{2} & \text{if } \pi/6 \leq \omega t \leq 5\pi/6 \\ \frac{1}{2} - m \cos(\omega t - \frac{\pi}{4}) & \text{if } 5\pi/6 \leq \omega t \leq 7\pi/6 \\ \frac{1}{2} - \frac{M}{2} & \text{if } 7\pi/6 \leq \omega t \leq 11\pi/6 \\ \frac{1}{2} - m \cos(\omega t - \frac{\pi}{4}) & \text{if } 11\pi/6 \leq \omega t \leq 2\pi \end{cases} \quad (4.20)$$

However, this does not lead to a significant increase of the first harmonic amplitude of the voltages applied to the drive coils compared to third harmonic modulation and thus will not be investigated further. Theoretically, a square-wave duty-cycle could be applied to all bridge-

legs for the control of the drive system. The resulting currents in the drive phases as well as in the common bridge-leg are shown in Fig. 4.7(a) for the case of a phase inductance of $L_D = 35$ mH and dc-link voltage of $U_{dc} = \sqrt{2} \cdot 230$ V. As can be seen the current i_{D0} in the common bridge-leg does linearly increase with the sum of the two drive currents according to

$$\hat{i}_{D0} = \sum_{j=1}^2 t_{rise} \frac{U_{dc}}{L_{Dj}}. \quad (4.21)$$

Here, t_{rise} is defined as $t_{rise} = 1/(4f_m)$ with f_m as the mechanical frequency of the rotor. In Fig. 4.7(b), the frequency f_r dependent drive peak current i_D and the corresponding common bridge-leg current i_{D0} are depicted. Looking at this graph clearly reveals that applying full-square-waves to all bridge-legs is not possible in the frequency range up to 9000 rpm (= 150 Hz). As a conclusion, the square-wave modulation can only be applied to the common bridge-leg.

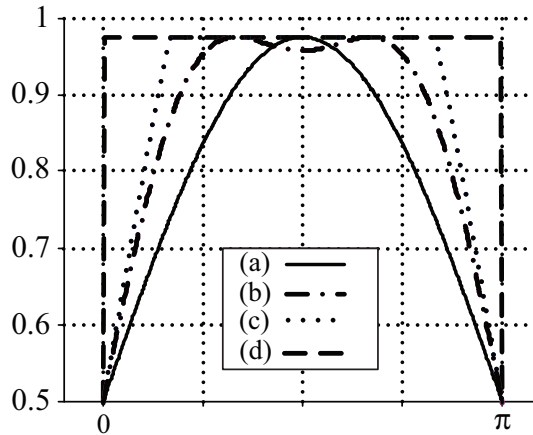


Figure 4.6: Duty cycle waveform for (a) purely sinusoidal, (b) third harmonic, (c) constant 120° and (d) full square wave modulation.

The proposed modulation schemes have been implemented on a DSP and tested with a laboratory prototype of the system that is shown in chapter 7. The measurement results are also illustrated in that chapter.

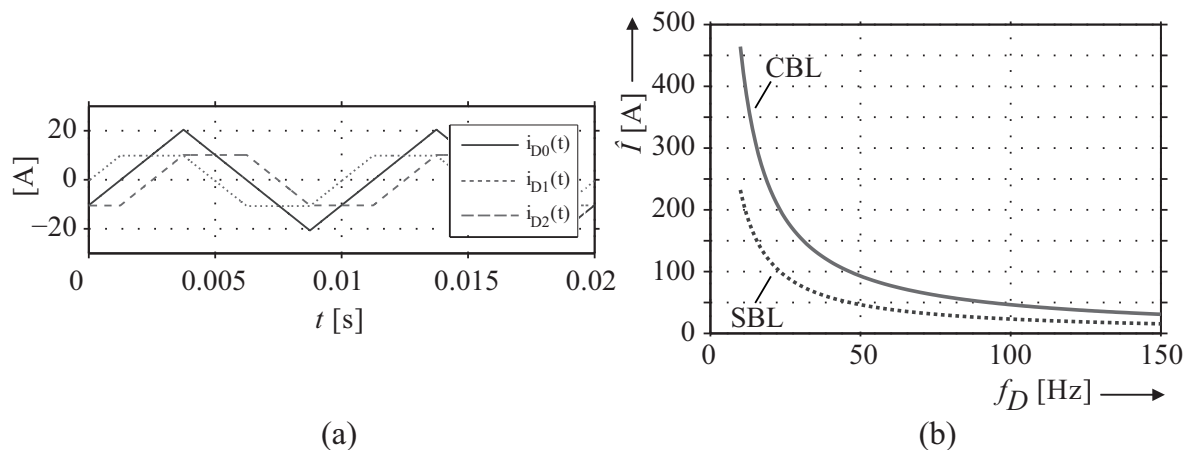


Figure 4.7: Simulated current waveform in case of square-wave modulation in all bridge-legs (a) and frequency dependent maximal current amplitude in the separate (SBL) and common bridge-leg (CBL) (b).

4.5 Comparison

In order to compare the effect of the presented modulation schemes the fundamental harmonic of the voltage applied to the drive coil L_D is calculated for each of the average voltages \bar{u}_{D1} depicted in Fig. 4.2, 4.3 and 4.5. The comparison is done with the value obtained with the state-of-the-art full-bridge modulation method (FBM) implemented for the control of the topology in Fig. 2.1. The maximum amplitude achievable with the CCM method is half of that which results from FBM as can be seen in Fig. 4.8. Furthermore, the maximum voltage that can be obtained with the optimal modulation scheme (TQM) for the interleaved half-bridge topology is 86% of that resulting with FBM and the state-of-the-art full-bridge topology. This circumstance has a direct influence on the maximum achievable drive power of the pump. Therefore, in a next step, the peak drive power that can be achieved with each of the modulations discussed beforehand is calculated in dependency on the rotational speed of the impeller. This is an important figure for characterising the suitability of a topology for driving a pump with a certain power demand at certain rotational speeds. Since in pump applications significantly higher power levels are required for the drive system than for the bearing system, the decisive factor for the comparison is the drive part and the following considerations will only refer to this part of the system.

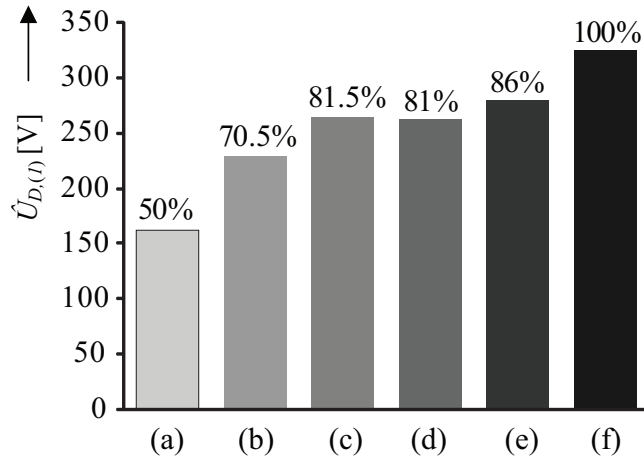


Figure 4.8: Maximum applicable fundamental amplitude of drive voltage $u_{D(1)}$ achieved with the (a) CCM (b) SCM (c) QCM (d) THM (e) TQM and (f) FBM method with respect to the full dc-link voltage (100%) that can be obtained with full-bridge topology.

4.5.1 Fundamental Drive Voltage

The maximum applicable drive power to each of the two motor phases is depending on the back EMF (electromagnetic force) voltage, which is induced into a drive coil as well as on the drive current impressed in that coil. Thus, before the drive power can be calculated, the form of this fundamental voltage must be known. If field oriented control is applied (cf. Fig. 4.9), the fundamental components of these quantities are in phase.

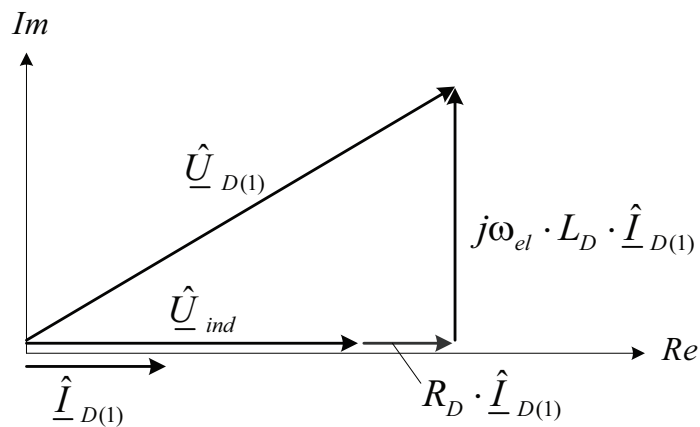


Figure 4.9: Phasor diagram of the equivalent electrical circuit of one drive phase with the basic phasor orientation.

The question now arises how the superposition of higher harmonics to the applied drive voltage does result in speed oscillations of the impeller and as a result of this in a induced voltage that is of nonsinusoidal form. Arising speed oscillations would also result in higher vibrations of the impeller which then reduces its lifetime. Latter is a known issue not only in the design of bearingless pumps but also in the design of conventional pumps [60]. In order to verify this circumstance for the bearingless pump system, the following experimental verification is carried out. The pump is run in one phase operation at a constant speed of $n = 5000$ rpm. This means that only one of the two drive phases is connected to the voltage–source inverter, whereas the second one is kept open. The control of the first one is done with the TQM modulation scheme presented in section 4.4.3. The induced voltage $U_{ind}(t)$ is then measured across the open drive coil L_{D2} . As can be seen in Fig. 4.10, this voltage is of sinusoidal form although the current i_{D1} is distorted significantly. This leads to the conclusion that as a result of its high inertia the impeller is rotating at constant speed despite of higher harmonics superposed to the drive current. With this, it has been proven that the impeller speed of the pump can be assumed to be constant. This implicates a non pulsating and thus constant output flow of the pump.

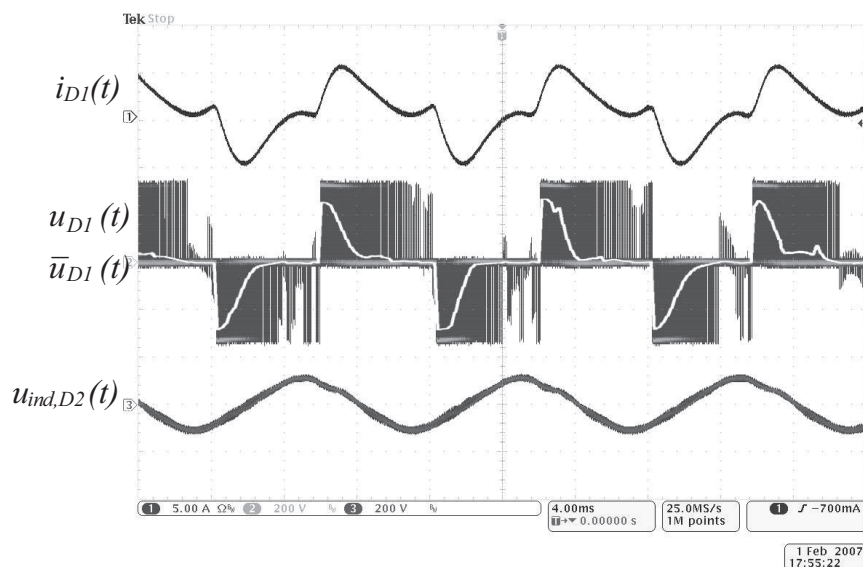


Figure 4.10: Experimental results for the induced voltage for highly distorted drive currents obtained with TQM. Time behavior of drive current i_{D1} , switched voltage u_{D1} and average voltage \bar{u}_{D1} across drive coil L_{D1} and induced voltage $u_{ind,D2}$ in drive L_{D2} . Current scale: i_{D1} : 5 A/div, voltage scale: u_{D1} , $u_{ind,D2}$: 200 V/div, time scale: 4 ms/div.

4.5.2 Maximum Achievable Drive Power

Due to the fact that the induced voltage does not contain higher harmonics (see previous section), only the fundamental harmonic of that current needs to be considered for the calculation of the drive power. Assuming sinusoidal waveforms, the absence of magnetic saturation and the employment of field oriented control, the drive power P_D of one drive winding is given by:

$$P_D = \hat{U}_{ind} \sin(\omega t) \cdot \hat{I}_{D,(1)} \sin(\omega t), \quad (4.22)$$

with the peak value of the fundamental harmonic of the current in the drive phase $\hat{I}_{D,(1)}$, which is controlled to be in phase with with \hat{U}_{ind} , the peak value of the induced voltage in that winding. The induced voltage is increasing linearly with the rotational speed n

$$U_{ind,rms} = k_{U,ind} \cdot n, \quad (4.23)$$

The value of k_U depends on the specific configuration of the motor and is calculated by simulations to $k_U = 4.16$ mVrms/rpm per 100 windings for the here employed motor [48]. According to the phasor diagram shown in Fig. 4.9, the following equation is given:

$$\hat{U}_{D,(1)}^2 = \left(\hat{U}_{ind} + R_D \hat{I}_{D,(1)} \right)^2 + \left(\omega_M L_D \hat{I}_{D,(1)} \right)^2, \quad (4.24)$$

where $\omega_M = 2\pi n/60$ is the rotating speed of the impeller in rad/s in a two-phase motor setup (see section 5.3.4). Solving 4.24 for $\hat{I}_{D,(1)}$ and combining it with 4.23 results in:

$$\hat{I}_{D,(1)} = \frac{-\sqrt{2} k_{U,ind} R_D}{R_D^2 + (\omega_e L_D)^2} \pm \frac{\sqrt{(R_D^2 + (\omega_e L_D)^2) \hat{U}_{D,(1)}^2 - (\omega_e L_D k_{U,ind} \sqrt{2} n)^2}}{R_D^2 + (\omega_e L_D)^2} \quad (4.25)$$

Due to the field-oriented control the drive current and the induced voltage are in phase and thus the drive power $P_{D,1}$ in phase 1 is a square

sine and the drive power $P_{D,2}$ is a square cosine. With

$$\cos^2 + \sin^2 = 1 \quad (4.26)$$

a constant electric motor power $P_{D,el,tot}$ results from the superposition of the two single phase drive power values that have the same absolute value:

$$P_{D_{el,tot}} = 2 \cdot P_D = 2 \cdot U_{ind,rms} \cdot I_{D,(1),rms}. \quad (4.27)$$

In Fig. 4.11 the values of the maximum achievable drive power for the different modulation schemes are evaluated for the two-phase motor configuration. The employed motor has an inductance $L_D = 35$ mH and resistance $R_D = 720$ m Ω per drive phase and the converter parameters are given by the dc-link voltage $U_{dc} = 325$ V, the maximum duty cycle $M_{max} = 0.95$ and a maximum current rating $I_{D,max,rms} = 10$ A for the coil current and thus also for the currents in the semiconductors of the separate bridge-legs. This still provides a current margin for the semiconductors in the common bridge-leg which face higher currents due to the discussed reasons. The maximum drive power demanded by a specific pump application ($P_{Pump,el}$) [48] at different rotational speeds is depicted in that graph as well. It can be seen that the achievable drive power is limited for lower rotational speeds by the maximum allowable drive current. When increasing this figure, the achievable peak power is shifted towards lower speed values. On the other hand, for higher speeds the maximum applicable drive voltage that is ensured by the respective modulation scheme limits the achievable drive power. This is due to the fact that with increasing rotational speed, the induced voltage rises as well (eq. 4.23) and thus limits the voltage drop across the coil that is needed to drive the current and thus generate the drive power in conjunction with the induced voltage.

As can be seen in 4.11, above a rotating speed of $n = 6500$ rpm the CCM method cannot be utilised anymore since the induced voltage is becoming higher than the maximum applicable voltage, whereas with SCM still three times the power can be delivered to the drive system at this speed. The power rating can be further improved when switching to an increased modulation depth by using the QCM, THM (which have the same performance). Operating the interleaved half-bridge topology

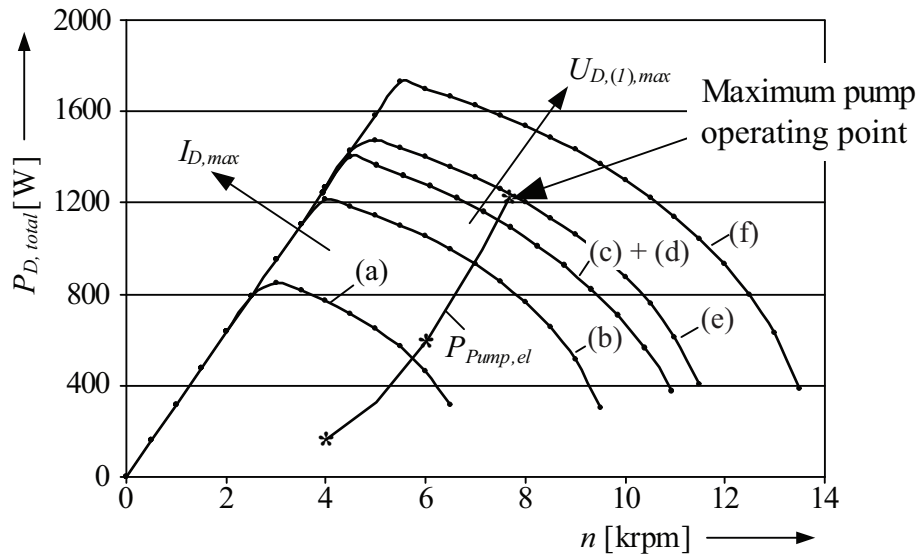


Figure 4.11: Total achievable drive power for the motor in dependency on the rotational speed, when employing the conventional full-bridge (f) topology and the interleaved half-bridge topology with CCM (a), SCM (b), QCM (c), THM (d) and TQM (e). Also shown is the typical electrical power required for a specific pump application ($P_{Pump,el}$).

with the square-wave modulation method in the common bridge-leg (e) leads to a further significant increase of the maximum obtainable drive power as illustrated in this figure. The maximum hydraulic power of the pump is limited to a flow of 100 l/min with a pressure of 3.6 bar [48]. This is achieved at a speed of $n = 8000$ rpm and the necessary drive power required to operate the pump at this point is $P_D = 1190$ W. This can be achieved by the TQM method with no performance decrease compared to the conventional full-bridge topology with its modulation. Furthermore, it can be seen that the achievable drive power is limited for lower rotational speeds by the maximum allowable drive current. On the other hand, for higher speeds the maximum applicable drive voltage that is ensured by the respective modulation scheme limits the achievable drive power.

4.5.3 Variation of Drive Windings

Until now, the comparison has been carried out with a motor that is available off-the-shelf and therefore it is not possible to vary the number of drive windings. However, the drive power characteristic changes with

the selection of the number of drive turns.

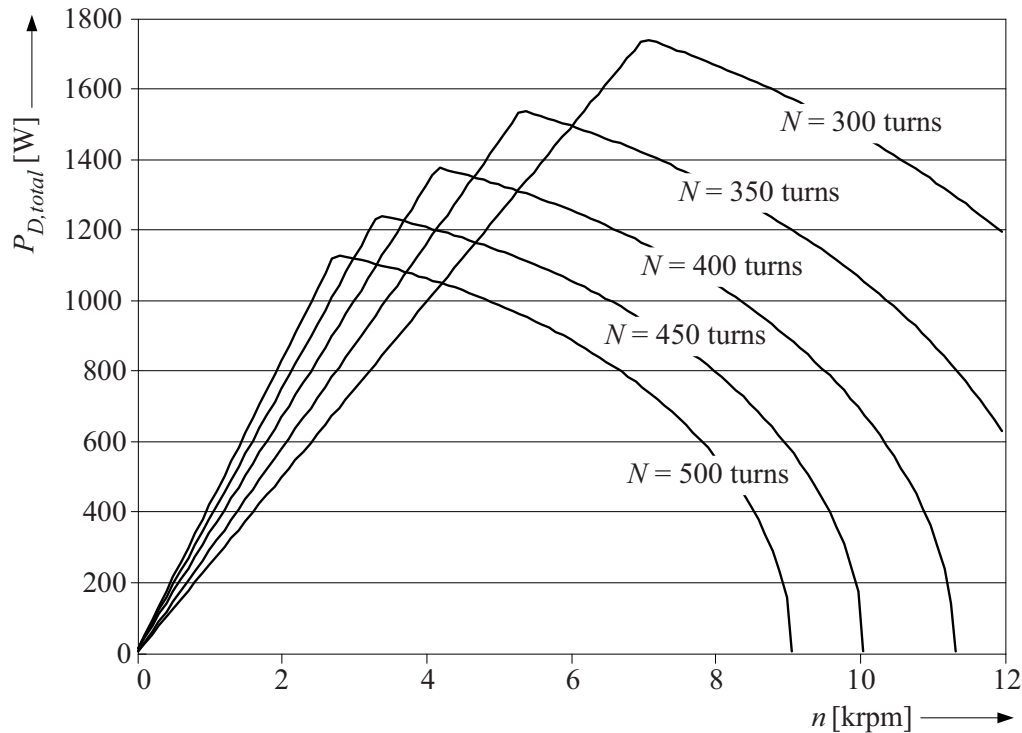


Figure 4.12: Dependency of the drive power characteristic for the interleaved half-bridge topology (c.f. Fig. 2.3 operated with the TQM method on the number of drive windings.

In particular, a higher winding number results in higher factor $k_{U,ind}$ and thus in a higher induced voltage (see eq. 4.23). As a result of this the drive power is increased at low rotational speeds. On the other hand, the inductance becomes higher and as a result of that, a lower drive power at high rotational speeds arises. Fig. 4.12 illustrates the optimisation of the number of drive windings for the interleaved half-bridge topology with operated with TQM. Since for pump applications the power demand is normally increasing with the rotational speed, the selection of the number of drive windings must be carried out properly in order to deliver the maximum power at maximum rotational speed. E.g., for the case at hand, $N = 370$ must be chosen to drive the pump until 6000 rpm.

4.5.4 Summary

In this chapter, modulation concepts for the control of a two-phase bearingless slice motor pump operated with the interleaved half-bridge topology are derived from the constant common bridge-leg modulation discussed in chapter 2. It is shown that peak voltage applicable to the drive phases is increased when higher harmonics are superposed to the duty-cycles of the bridge-legs. With the highest level of harmonic superposition the maximum voltage applicable to the drive phases is 86% of that obtained with the state-of-the-art full-bridge topology and its control method. Furthermore, it is shown with experimental measurement that the higher harmonics in the drive current, which are caused by this harmonic injection, do not have an impact on the constant speed of the impeller and thus on the constant output flow of the pump. The proposed modulation schemes are compared based on the maximum achievable drive power for the motor. This comparison has revealed that the maximum power level of the pump operated with the full-bridge topology can also be achieved with interleaved half-bridge topology by use of the herein presented modulation schemes. This clearly shows that this topology is a favorable concept for next generation bearingless pump systems.

Chapter 5

Motor Configurations

So far, only the power electronics has been taken into consideration as the part with a potential for complexity and hence cost reduction on the way towards a next generation bearingless pump system. Since the mechanical setup of the motor has a strong impact on the realisation effort of a bearingless slice motor this part of the system must also be investigated regarding the complexity reduction, losses and performance. Thus, this section focuses on the evaluation and discussion of five different motor-controller setups. The comparison will be carried out for two-, three- and four-phase bearingless slice motor concepts based on performance indices such as power losses, power electronics requirements and cost related issues. Especially, the latter plays an important role in the applicability of these concepts in the respective applications mentioned in section 1.1.3. In prior research [7] the scalability of bearingless slice motors in centrifugal pumps towards higher power levels was investigated. One of the conclusions of that work is that the iron losses increase disproportionately high if the motor is scaled geometrically. Thus, a direct scaling for higher power levels is not applicable for bearingless slice motors. In fact, the motor dimensions have to be designed individually for the targeted power level. Scaling all motor dimensions linearly is only possible in a small power range as shown in [7]. The focus in that work is on the investigation of the maximum achievable bearing force in the respective configurations, while the achievable torque and the power electronics requirements were not taken into consideration. A further finding of that

work, which is very helpful for the hereafter carried out comparison is the fact that only temple motor configurations with 6 and 8 claws are of interest for a temple motor design suitable for the power level targeted in this chapter. A configuration with 12 claws should only be considered for a rated power above 2000 W. Since the focus of this work lies on a cost efficient motor–controller configuration up to a maximum of 2000 W and not on the scalability of the motors, these results provide a good base for the selection of the configurations of interest for the comparison. Certain configurations can thereby be excluded right away without the necessity of further investigations. As shown in [2], only configurations with a number of pole pairs of $p_2 = p_1 + 1$ (p_2 represents the pole pairs of the bearing system and p_1 of the drive system, respectively) must be taken into consideration, since configurations with $p_2 = p_1 - 1$ possess awkward force proportions. In these configurations, particular rotor angles exist where the Maxwell– and Lorentz–forces cancel each other out. This makes the realisation of these configurations difficult – if not even impossible. However, in [1] and [61] it is shown that it is theoretically possible to build up a bearingless motor with $p_2 = p_1 - 1$. Besides the temple motor design, also a bearingless motor design in disc shape that was first presented in [61] is taken into consideration in the following since it is a promising concept for a future bearingless pump system with a reduced volume.

The focus is also laid on the interaction of the flux impressed by the currents in the drive and bearing windings. For example, a configuration where due to the chosen arrangement of the drive phases the currents in the respective phases cause shear forces that act on the rotor would influence a stable levitation of the impeller. Thus, certain measures would have to be taken into consideration when selecting such a configuration for a future bearingless pump system.

5.1 Force and Torque Calculation

In an electrical machine, two magnetic actions of force are known. Namely the Lorentz and the Maxwell force. These two quantities must be known for the calculation of the forces and torque acting on the rotor. With the analytical force and torque model, which was first presented in [61] for the design of bearingless slice motors in disc shape with concentrated coils,

these quantities can be evaluated. The applicability of this model for the comparison of slice motor concepts is demonstrated in [62]. However, in that paper the comparison has only been carried out for slice motors in disc shape with concentrated coils, whereas the main focus in the hereafter presented comparison is laid on the temple motor design.

The model can be used under the assumption of a completely linear system where the impeller, meaning the rotor of the motor, is positioned exactly in the center of the iron circuit and no unbalances are present. Also, no saturation of the iron circuit is occurring and any armature reaction is neglected. In the following, only a brief summary of the theoretical fundamentals will be given here. Continuitive information on the analytical model can be found in [63].

With the precise knowledge of the electromagnetic field variables in the air gap of the motor a general force and torque model can be derived with the use of the Maxwell stress tensor T_M [64]

$$\mathbf{T}_M = \mu \begin{bmatrix} H_t^2 - \frac{1}{2}H^2 & H_t H_n & H_t H_n \\ H_n H_t & H_n^2 - \frac{1}{2}H^2 & H_n H_z \\ H_z H_t & H_z H_n & H_z^2 - \frac{1}{2}H^2 \end{bmatrix}. \quad (5.1)$$

Here, H is the magnetic field intensity, which is composed of

$$\mathbf{H} = [H_t \ H_n \ H_z]^T, \quad H = |\mathbf{H}|, \quad (5.2)$$

and μ is the permeability. The mechanical stress σ acting on a surface element can then be calculated with

$$\boldsymbol{\sigma} = \mathbf{T}_M \mathbf{e}_n, \quad (5.3)$$

where \mathbf{e}_n represents the vector perpendicular to the stator surface (cf. Fig. 5.1). Furthermore, it is assumed that the permeability of the ferromagnetic stator is much higher than that of air ($\mu_2 \gg \mu_1$) and thus the tangential component of the flux density H_{1t} in the air gap can be neglected for the following calculation of the torque and the forces responsible for the levitation of the impeller.

With this, the mechanical tension σ_{12} on the interface between air

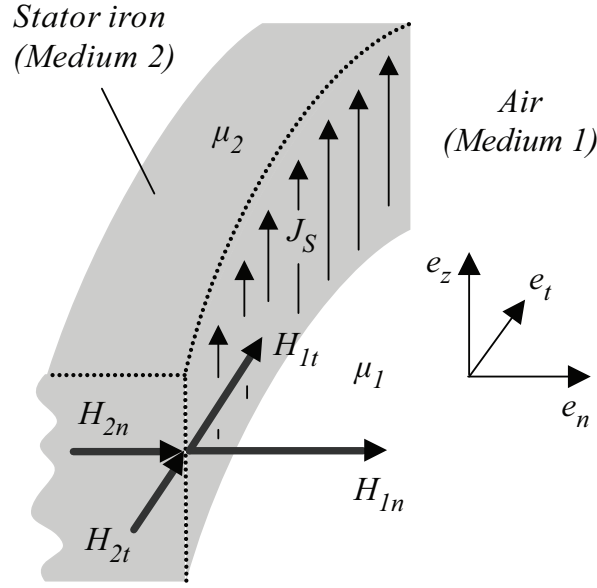


Figure 5.1: Stator surface with current density distribution and field strength in the air gap.

(medium 1) and stator iron (medium 2) can be approximated by

$$\boldsymbol{\sigma}_{12} = \begin{bmatrix} \frac{B_{1n}^2}{2\mu_0} \\ B_{1n} J_s \\ 0 \end{bmatrix} \quad (5.4)$$

where J_s is the current density distribution on the stator surface, which is assumed of cylindrical shape, and B_{1n} is the normal component of the flux density in air. The forces that are generated by the component $\frac{B_{1n}^2}{2\mu_0}$ are often called Maxwell–forces in literature. Due the high permeability of iron they act almost radially away from the rotor in a electrical machine and are therefore responsible for the generation of the levitation forces. The component $B_{1n} J_s$ generates forces that are acting tangentially along the outline of the rotor. These Lorentz–forces cause levitating forces as well as torque. The two quantities that act on the rotor of the bearingless slice motor are determined by the surface integral

$$\mathbf{F} = \oint_A \boldsymbol{\sigma}_{12} dA, \quad (5.5)$$

where A represents the area of the surface. With the help of (5.5) the

rotor angle α depending torque T_s and force F_s that act on the rotor can be calculated to

$$T_s = -l_s r_s^2 \int_{-\pi}^{\pi} B_{1n} A_s d\alpha, \quad (5.6)$$

$$\mathbf{F}_s = -l_s r_s \int_{-\pi}^{\pi} \begin{bmatrix} \cos\alpha & -\sin\alpha & 0 \\ \sin\alpha & \cos\alpha & 0 \\ 0 & 0 & 1 \end{bmatrix} \cdot \begin{bmatrix} \frac{B_{1n}^2}{2\mu_0} \\ B_{1n} A_s \\ 0 \end{bmatrix} d\alpha. \quad (5.7)$$

Looking at these equations reveals that the calculation of the bearing forces can be approximated with the flux density in the air gap and the current density distribution on the stator surface. The flux density in the air gap is the superposition of the flux density of the permanent magnet and the flux density that is caused by the stator windings. Furthermore, the so resulting bearing force and the torque are depending on the rotor angle. The magnitudes obtained in 5.6 and 5.7 are acting on the stator. However, for the classification of the motor embodiments, the respective forces \mathbf{F}_r and torque M_r acting on the rotor are of interest. They can be calculated with

$$\mathbf{F}_r = -\mathbf{F}_s \quad (5.8)$$

and

$$T_r = -T_s. \quad (5.9)$$

Before this model can provide the base for the analysis of the different concepts, a simulation of all the topologies must be carried out in order to gain the electromagnetic field distribution in the different motor embodiments. In the here presented case, the simulations are carried out with the simulation program Maxwell [65]. Given a specific load point in a pump application with the therein required torque on the impeller and the arising forces to stabilise it, the currents in the drive and bearing system, which provide the basis for the comparison of the hereafter presented motor configurations can be obtained with this mathematical model. The load point at which the comparison is carried out is specified in the following section.

5.2 Investigated Configurations

In the following, the five different bearingless slice motor concepts are presented that will be comparatively evaluated with the performance indices presented in the previous section. As a base for the comparison, the following assumptions are considered for the design of the bearingless slice motors:

- The required rated drive power at the chosen operating point is $P_{DR} = 1200$ W.
- The bearing system is designed in order to ensure the sufficient levitation forces for the whole operating range. The peak bearing force is set to 20 N in all configurations.
- The maximum speed for the comparison is set to 8000 rpm.
- The rotor diameter and the stator bore, respectively, are the same for all the chosen configurations.
- At rated torque, the current density in the windings is the same for all the chosen configurations.
- The flux density in the iron circuit is assumed the same for motor configurations (a)–(d).
- Configurations (a)–(d) are realised as a temple motor (cf. Fig. 1.1), whereas configuration (e) is from disc shape.

In the following motor schematics, the direction of the currents flowing into the coils is marked with a dot or a cross. If a current is flowing into the coil, a cross is drawn on the coil. Otherwise, the coil is marked with a dot. The magnetisation of the rotor is illustrated with arrows. The coils responsible for the torque generation are labeled with a D and the bearing windings with a B , respectively. In case of a winding configuration, where the torque and levitation forces are generated in the same winding, the identification of the coils is carried out with a BD .

5.2.1 Two-Phase Motor Configuration (a)

The first motor concept included in the comparison is depicted Fig. 5.2. It shows a two-phase bearingless slice motor with 12 separate windings for the drive and bearing system and a two-pole ($p = 1$) permanent magnet (PM) rotor.

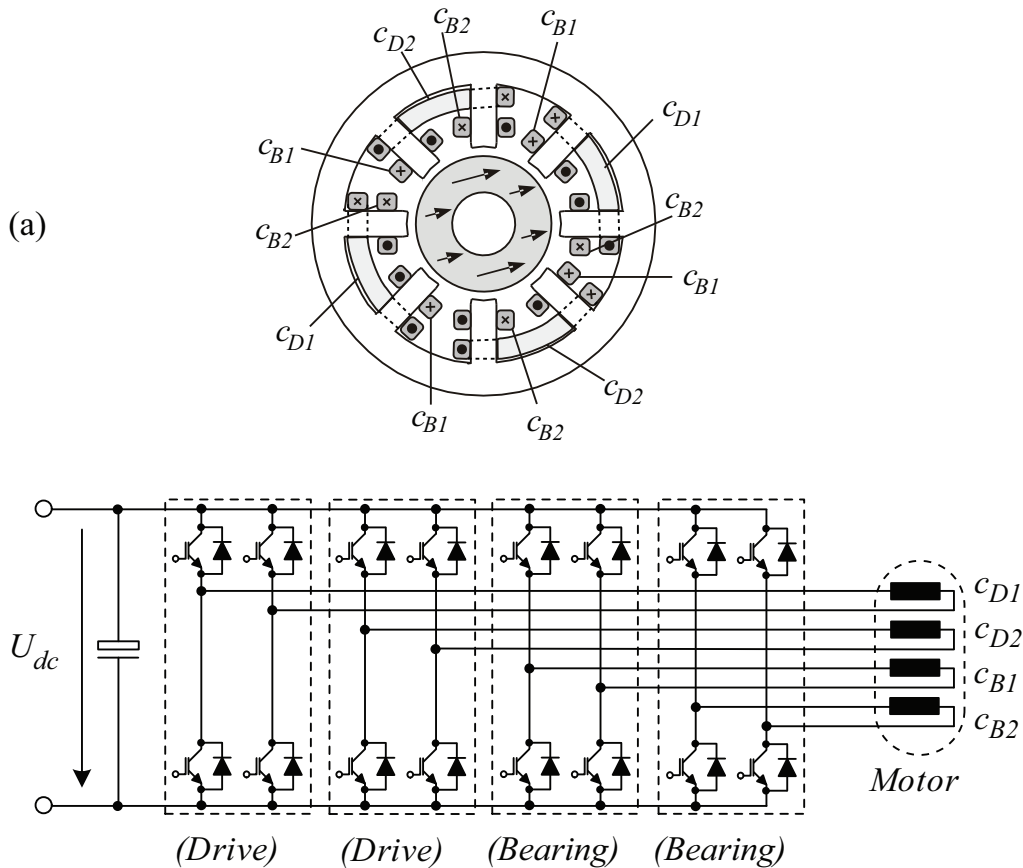


Figure 5.2: Two-Phase Motor Configuration (a).

This symmetrical winding configuration represents the standard setup in today's bearingless pump systems (see section 1.1.1) and possesses a total of eight claws. The orthogonal placement of the drive and bearing system results in an independent control of the drive and bearing flux due to $p_2 = p_1 + 1$. Contrary to the operation of this topology with only six half-bridges discussed in section 2 the standard full-bridge configuration with a total of 16 power transistors will be used in this section for sake of better comparability with the other concepts. The two-pole diametrically magnetised slice rotor is also relatively easy to manufacture. This results in a further advantage of this concept compared to motor

embodiments with rotors employing segment magnets. As shown in [66], this magnet generates a sinusoidal field distribution with low harmonics. These harmonics are mainly caused by the notches. Thus, the detent torque is also very small. However, the passive tilting behaviour is worse than with a magnet with four poles as described in [2].

Due to the already proven applicability of this concept in a bearingless pump and its acceptance in the existing markets, this concept shall also be included in the hereafter presented comparison. It can by all means also result in the favourable concept for future bearingless pump systems.

5.2.2 Three–Phase Pitched Drive Configuration (b)

In Fig. 5.3, a three–phase bearingless slice motor with nine separate windings and six claws for the drive and bearing systems and a two–pole ($p = 1$) PM rotor is shown.

This configuration does not have an orthogonal placement of the drive and bearing system as the one in the previous section. Thus, it cannot be excluded that the drive currents could cause bearing forces or vice versa. For this, a calculation of the configuration specific rotor angle dependent force–current constants k_{Fx} , k_{Fy} (in N/A) and torque–current k_T (in Nm/A) with the analytical model presented in section 5.1 must be carried out in order to verify this issue. The calculation results are shown in Fig. 5.4.

In the topmost row, the rotor angle dependent force–current constant k_{Fx} in x–direction is shown. It can be seen, that not only the bearing currents I_{B1} , I_{B2} and I_{B3} lead to a rotor angle dependent force in that direction, but also the drive currents I_{D1} , I_{D2} and I_{D3} have the same impact. Thus, these currents also contribute to the generation of bearing forces. For a stable levitation of the impeller, these shear forces must be compensated with a force applied by the bearing winding that points into the reverse direction. These additional currents lead to higher losses in the bearing system and thus give an indication about the overall losses arising in the motor configuration.

This drawback can either be overcome with an adequate control algorithm presented in [61] or by splitting the three drive windings in 6 drive windings as it is depicted in Fig. 5.5. Instead of two drive phases with two in series connected coils as in configuration (a), configuration

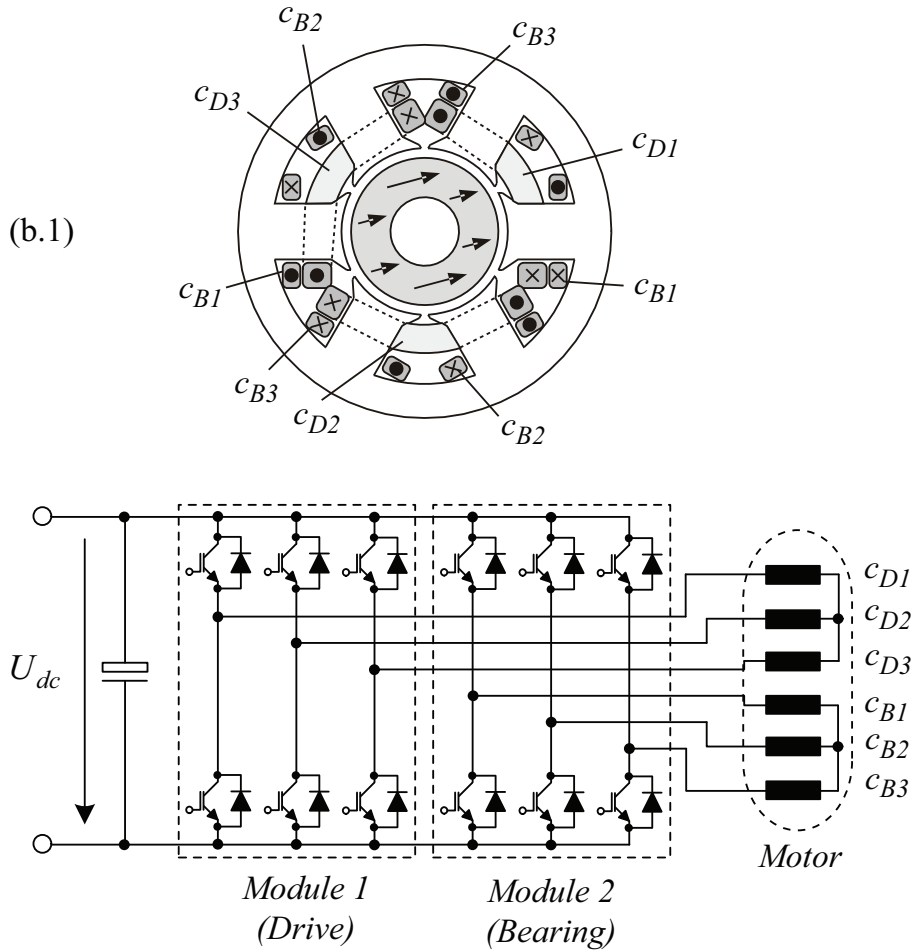


Figure 5.3: Three-Phase Pitched Drive Configuration (b.1).

(b.2) is realised with three drive phases having two coils in series each.

Compared to Fig. 5.4 the drive currents I_{D1} , I_{D2} and I_{D3} in the upper and middle row of Fig. 5.6 are equal to zero and thus do not lead to the generation of shear forces. They only lead to the desired torque and therefore do not influence the stable levitation of the impeller. The subsequent calculation of the copper losses for this motor embodiment is carried out with this modified configuration (b.2). However, the same results can also be obtained when the mentioned control schemes are applied for the control of the motor.

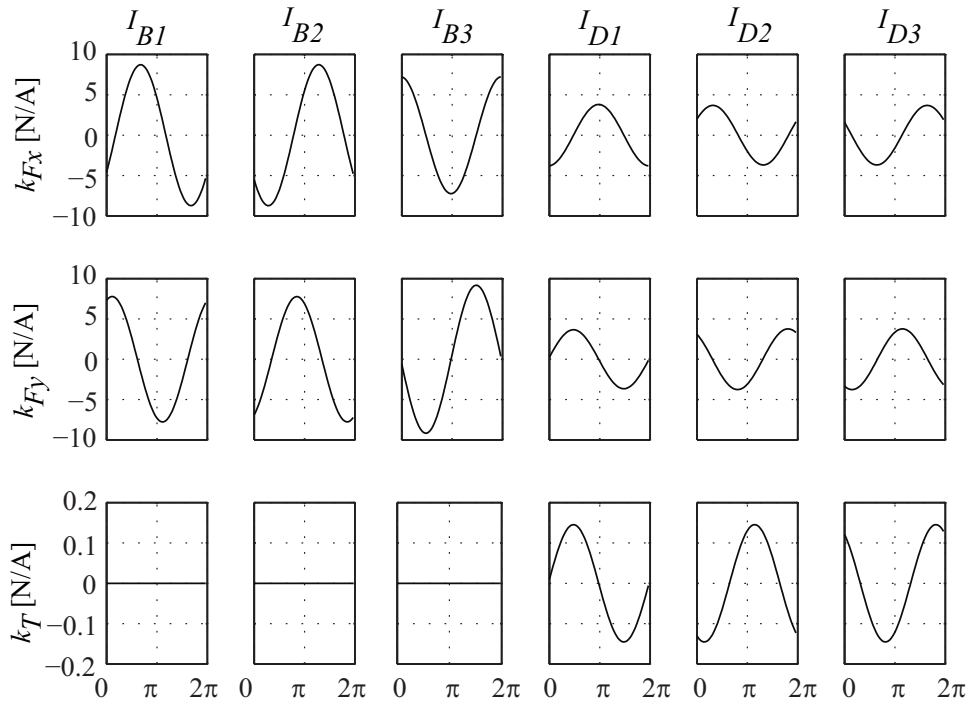


Figure 5.4: Force and torque currents in the Three-Phase Pitched Drive Configuration (b.1).

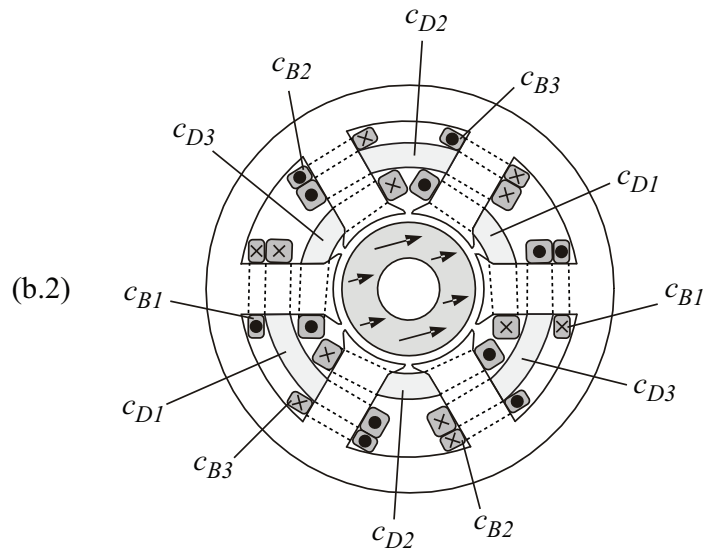


Figure 5.5: Three-Phase Common Drive Configuration with split drive phases (b.2).

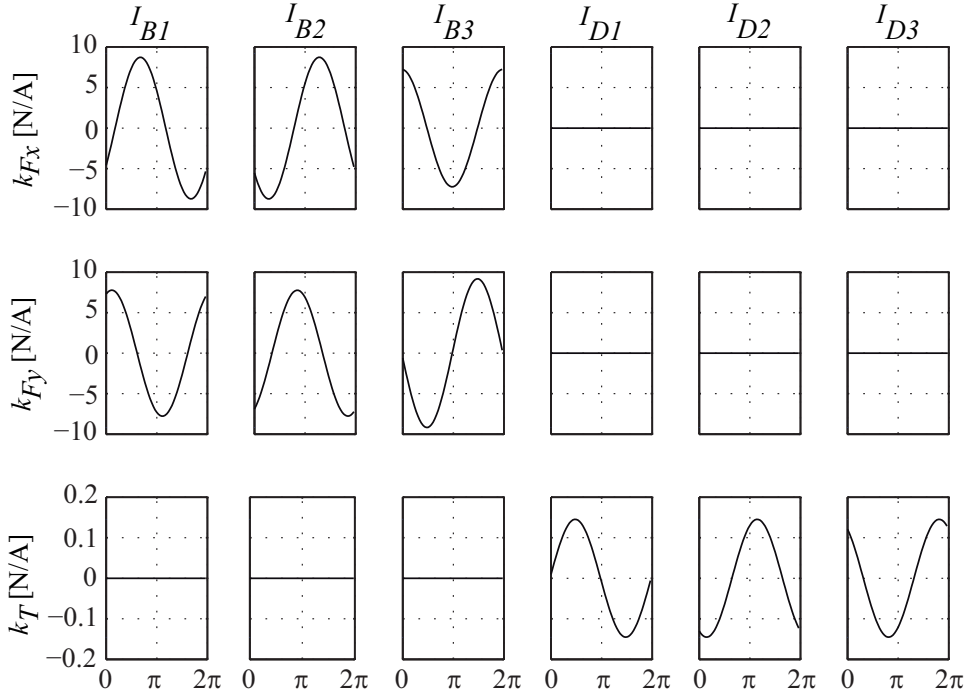


Figure 5.6: Force and torque currents in the Three–Phase Common Drive Configuration with split phases (b.2) (cf. Fig. 5.5).

5.2.3 Three–Phase Concentrated Drive Configuration (c)

A slightly modified three–phase concept is depicted in Fig. 5.7. It consists of nine separate windings and six claws building the drive and bearing systems. A two–pole ($p = 1$) PM rotor is also employed here. This concept was evaluated in [7] as the preferable topology for high power bearingless motors in centrifugal pumps. Though, the power electronics was not taken into consideration in that work as mentioned earlier on. Also its applicability for lower power levels has not been analysed yet. For these reasons, this motor–converter setup is also included in this comparison.

The motor constants k_{Fx} , k_{Fy} and k_M in dependency of the rotor angle are shown in Fig. 5.8. As can be seen there, an advantage of this setup is that the drive currents do not lead to a generation of bearing forces as it is the case for the previously described configuration. Thus, no further action must be taken considering the influence of the drive system on the stable levitation of the impeller.

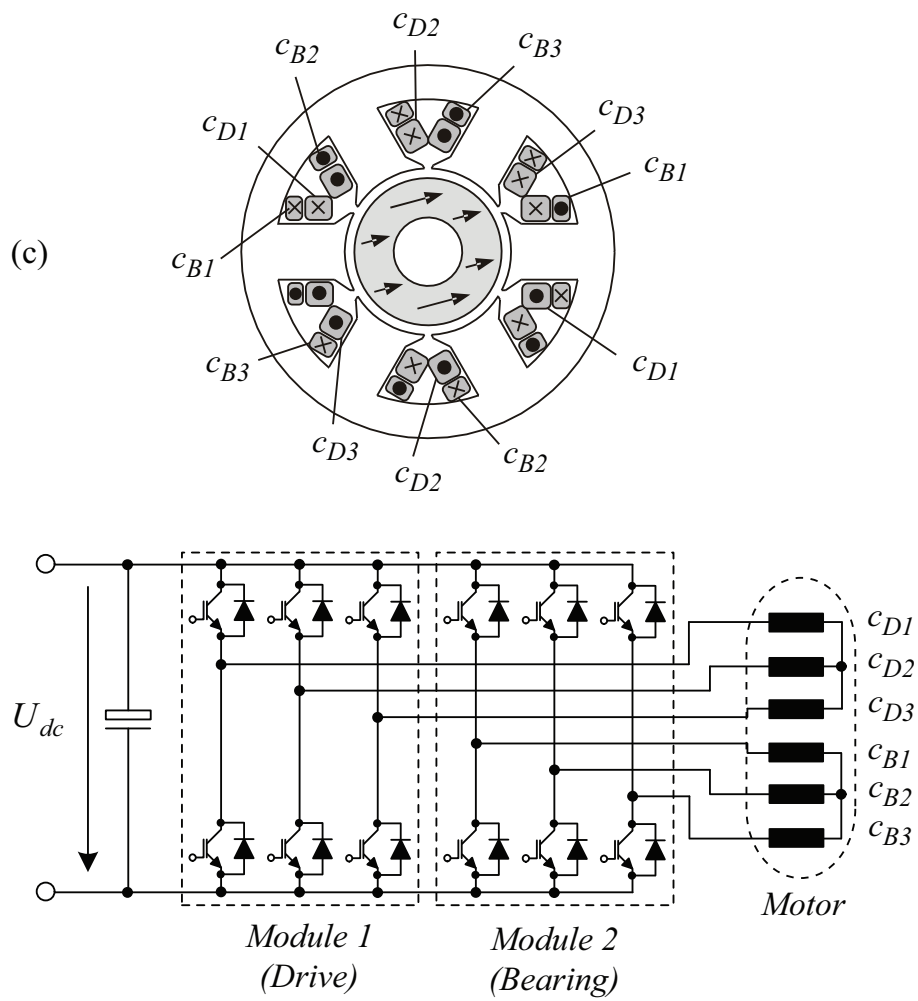


Figure 5.7: Three-Phase Concentrated Drive Configuration (c).

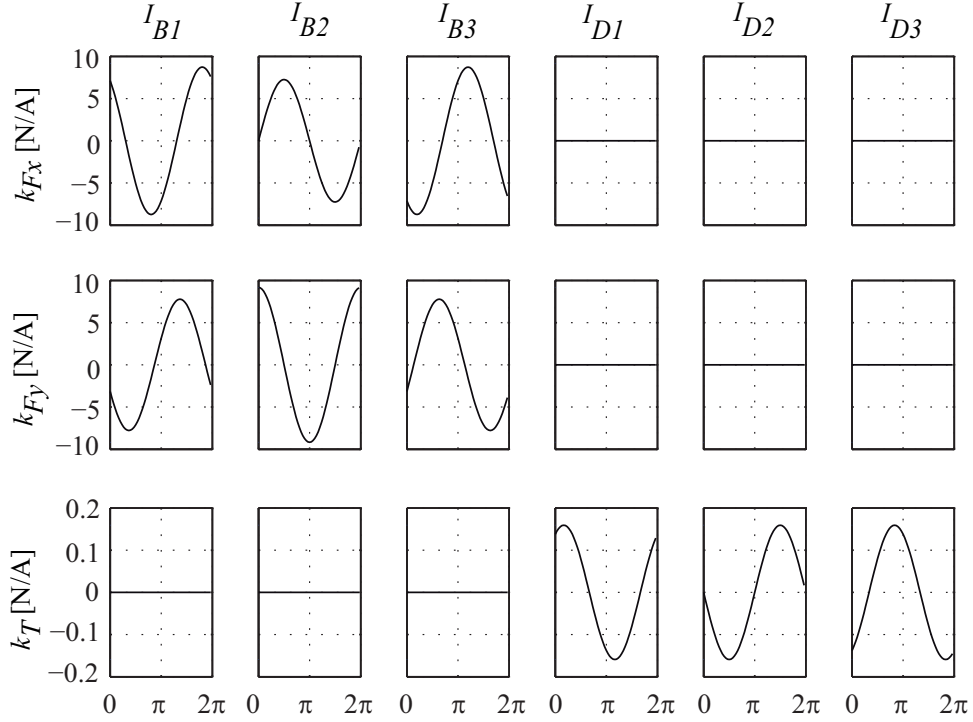


Figure 5.8: Rotor angle dependent force and torque constants in the Three-Phase Concentrated Drive Configuration (c).

5.2.4 Three-Phase Pitch Winding Configuration (d)

A three-phase bearingless slice motor with a number of six coils that generate the torque and the axial forces in common is the next concept to be looked at. The motor and the corresponding power electronics topology are depicted in Fig. 5.9. Due to the circumstance, that in this topology the drive and bearing currents are applied to the same windings, the current rating is the same for all coils. Again, a two-pole ($p = 1$) PM rotor is employed. The pitch winding configuration results in a more efficient torque generation and consequently in lower power losses compared to the motor embodiments (a) – (c) as will be shown later on. As a matter of fact, all currents in the six windings generate the torque and bearing forces in common as can be seen in Fig. 5.10.

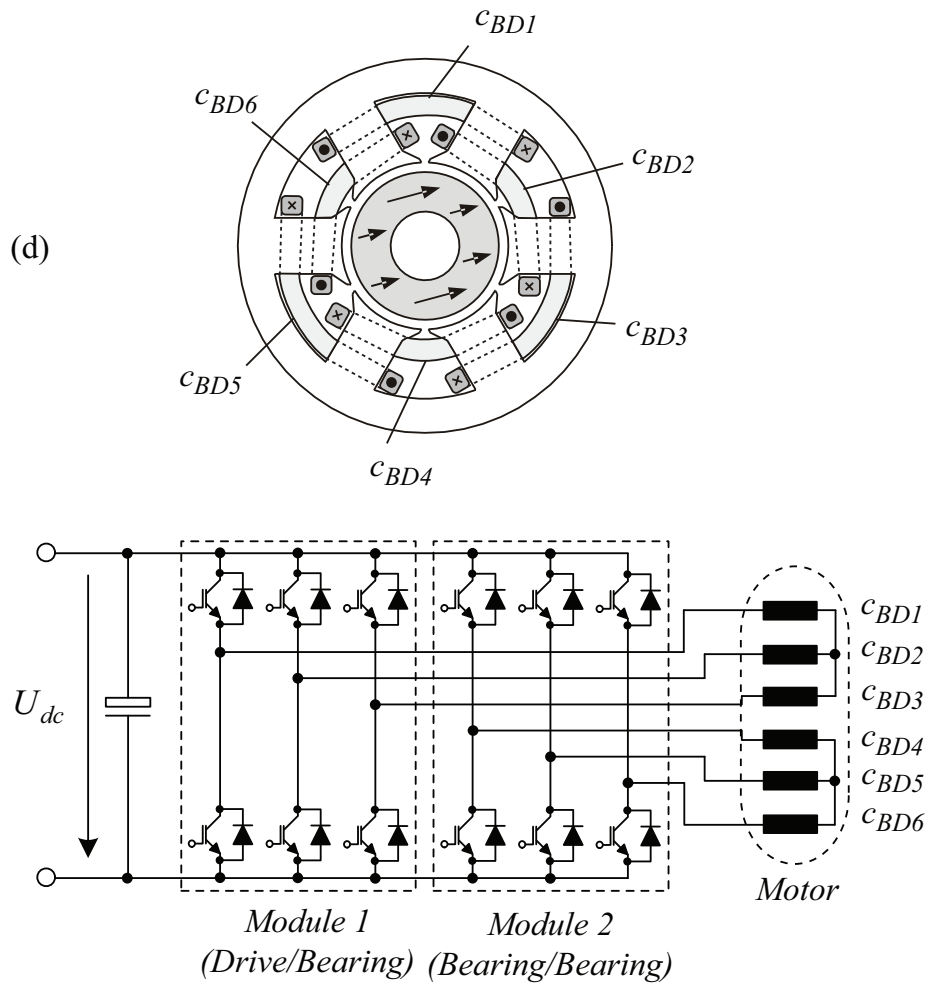


Figure 5.9: Three-Phase Pitch Winding Configuration (d).

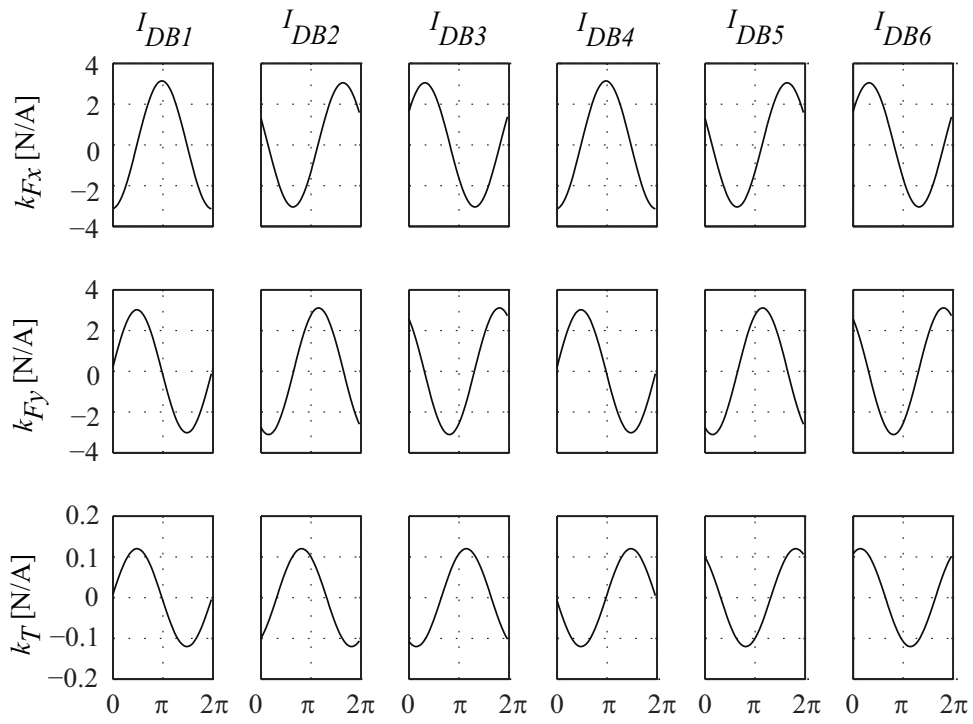


Figure 5.10: Rotor angle dependent force and torque constants in the Three-Phase Pitch Winding Configuration (d).

5.2.5 Four-Phase Combined Configuration (e)

The realisation of a bearingless motor with four concentrated coils was introduced in [61] and is named as the bearingless one phase motor. Its design is the simplest configuration that allows a bearingless operation. The drive and bearing systems are combined in a multiphase winding. This has the drawback that the dynamic of the bearing system is lowered due to the induced voltage in the coils, which has its origin in the rotating field of the rotor. The concept of a four-phase bearingless slice motor and a four-pole ($p = 2$) PM rotor is shown in Fig. 5.11.

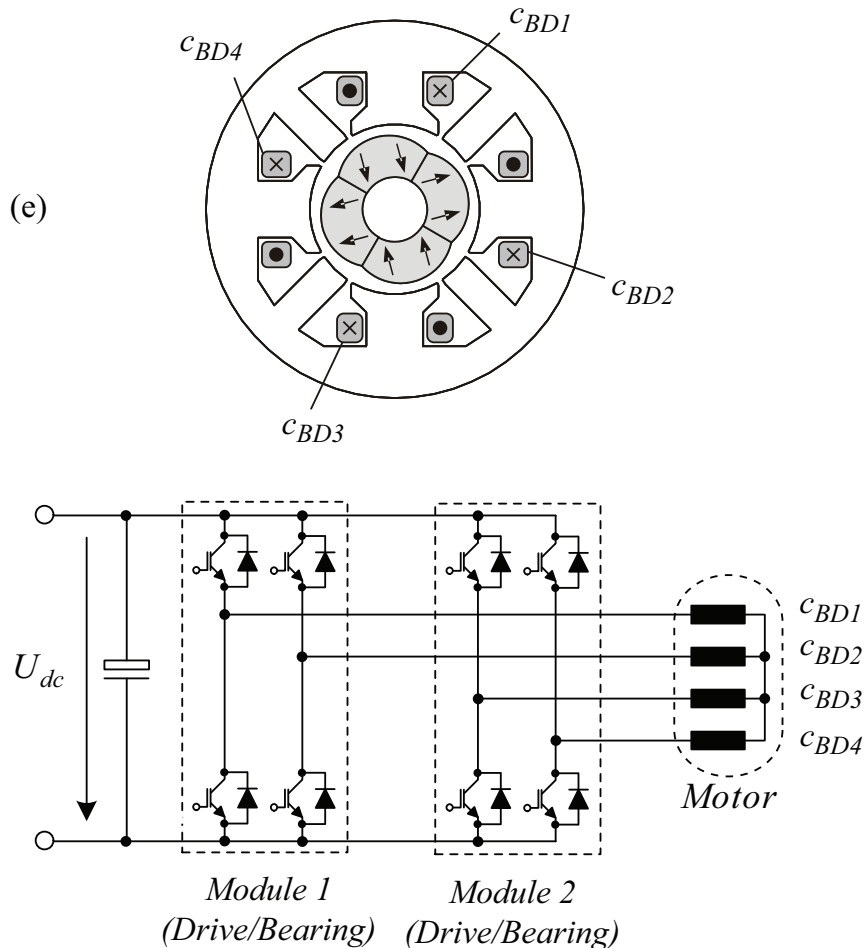


Figure 5.11: Four-Phase Combined Configuration (e).

In contrary to the previously described configurations, which are realised in temple motor design with each claw being placed in an orthogonal manner to the back iron (see Fig. 1.1), this motor is realised in disc shape with a homogeneously orientated lamination of the iron sheets.

The absence of intersections between the claws and the back iron in this configuration has a major impact on the total iron losses as well be shown later on. Although the motor has four phases that are connected in star, the torque generation is equivalent to a single phase motor [61]. Furthermore, it offers the benefit that only four power half-bridges are needed to generate the torque and levitation currents in the motor. Similar to embodiment (d), the drive and bearing systems are not decoupled anymore. This can be seen on the curves in Fig. 5.12, where all currents contribute to the force and torque generation.

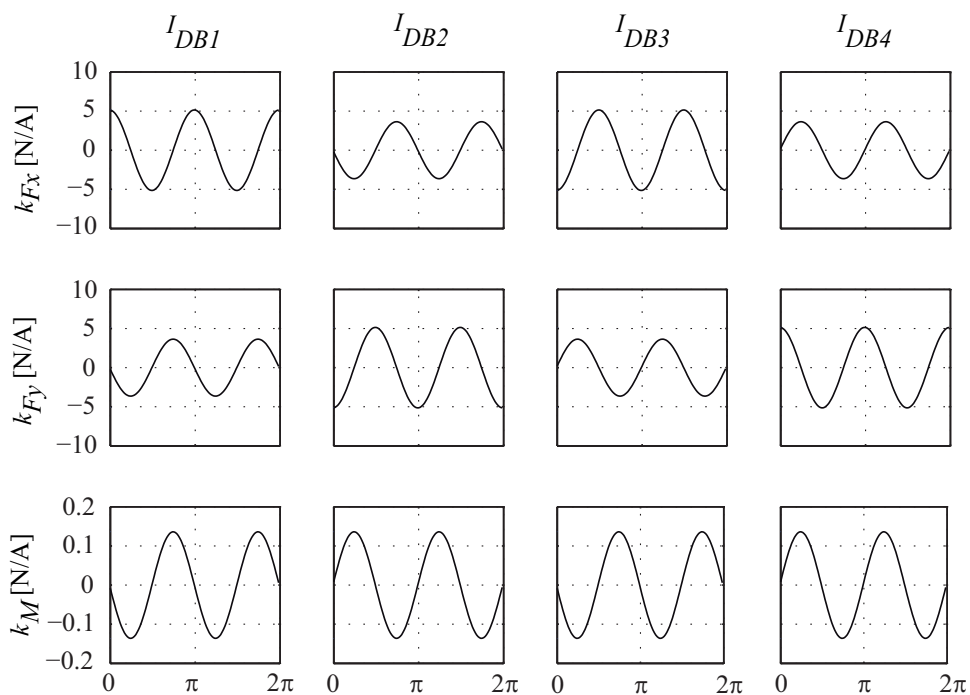


Figure 5.12: Rotor angle dependent force and torque constants in the Four-Phase Combined Configuration (e).

5.3 Comparison

For the comparison of the presented motors the configuration specific parameters must be known. The drive and bearing phase resistances R_D and R_B and inductances L_D and L_B along with the force-current- (k_x , k_y) and torque-current- (k_M) constant are compiled in table 5.1. The values of k_x , k_y and k_M have been gained with simulations based on the model presented in 5.1. In this comparison, the concepts are referenced

with (a)–(e) in accordance to the figures 5.2, 5.5, 5.7, 5.9 and 5.11. The evaluation is based on the load point specified in section 5.2. Because of the combined bearing and drive windings in the configurations (d) and (e) no values are available for R_B and L_B separately. The phase resistance and inductance for these two configurations are given by R_D and L_D .

Configuration	(a)	(b.2)	(c)	(d)	(e)
R_D [Ω]	0.67	0.6	0.54	0.46	0.34
L_D [mH]	35	21.4	41	21	3
k_x/k_y [N/A]	11.88	8.73	8.73	3.14	5.14
k_T [mNm/A]	201	145	159	120	136
R_B [Ω]	2.67	1.867	1.867	–	–
L_B [mH]	55	25.8	46.1	–	–

Table 5.1: Specific winding parameters of the presented topologies.

Looking at the torque constant k_M reveals that the highest torque per ampere phase current is achievable with the two-phase configuration (setup (a)). Still 79% of that can be achieved with the three-phase configuration (c). Still twenty six percent of the maximum torque of configuration (a) can be achieved with the three-phase configuration (c), whereas significantly lower values are obtained with the combined phase variations (d) and (e). Depending on the chosen application, this will be a major issue on the losses in the motor and as a consequence of that on the thermal limits of the motor since higher currents are demanded for a certain torque.

5.3.1 Loss Calculations

The evaluation of the losses in the motor and the power electronics is indispensable for a thorough comparison of the motor concepts. The most important portion is the copper losses occurring in the windings of the motor. In order to receive a better comparability between motors (a)–(e) the same current densities in the drive and bearing windings, respectively, have been assumed as design criteria for the calculation of the windings. A further important portion is the speed dependent iron losses, which are evaluated for all the presented embodiments subsequently.

Copper Losses

In a first step the copper losses P_{Cu} in the configurations (a)–(e) are evaluated. The calculation of the copper losses in the windings is principally based on the following equation:

$$P_{Cu} = \sum_{i=1}^m R_i I_{i,rms}^2, \quad (5.10)$$

with m as the number of winding phases of the subjected motor and R_i as the corresponding resistance value, which is calculated with

$$R_i = \frac{\lambda_{Cu} l_w}{A_{Cu}} \cdot n_C. \quad (5.11)$$

Here, l_w stands for the average winding length of the drive or bearing winding, λ_{Cu} the specific resistance of copper ($17.8 \cdot 10^{-3} \Omega mm^2/m$), n_C the number of coils that form a phase and A_{Cu} the wire cross area. However, the iron losses lead to a reduction of the drive torque wherefore an equivalent load torque has to be considered:

$$T_{Fe} = \frac{P_{Fe}}{\omega_m} = \frac{P_{Fe}}{2\pi f_m}. \quad (5.12)$$

Since the phase current is linearly dependent on the torque, the copper losses P_{Cu} in each motor can be written as

$$P_{Cu} = m_D \cdot \left(\frac{T_{mech} + T_{Fe}}{k_M} \right)^2 \cdot R_D + I_B^2 \cdot m_B \cdot R_B. \quad (5.13)$$

Doing this for all the motor embodiments (a)–(e) for the load point specified in section 5.2 leads to a loss distribution as depicted in Fig. 5.13. There, the copper losses are depicted in dependence of the applied bearing force. At 0% bearing force, only the copper losses in the drive system occur. Looking at the values at zero bearing force reveals that motor embodiment (d) only generates 56% of the losses occurring in configuration (b). This proportion stays almost the same when increasing the bearing force up to 100% (which equals 20N). The largest percental

increase in losses due to the generation of the levitation forces arises for motor (d). There, at maximum force the losses are increased by 30% compared to the load point with no currents in the bearing phases.

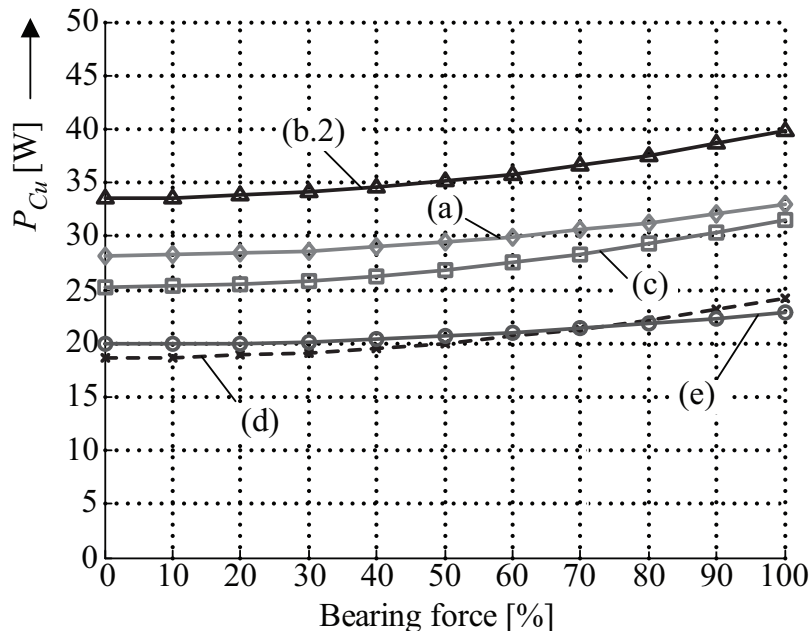


Figure 5.13: Total copper losses subject to an increasing levitation force at the design point of 1200W drive power for the motor configurations (a)–(e). 100% equals the maximum bearing force requested in a transient condition.

Iron Losses

According to [67], the hysteresis losses of iron can be approximated under the assumption that the magnitude of the flux density B of an alternating field is in the range of 0.2–1.5 T by the following equation:

$$P_{Hy} = c_{Hy} f_e \hat{B}^{1.6} m_{Fe}. \quad (5.14)$$

The hysteresis losses are thus linearly dependent on a material constant c_{Hy} , the electrical frequency f_e of the motor, and the iron mass m_{Fe} , while the dependency on the flux density is of higher order. On the other hand, according to the law of induction, an alternating magnetic field induces voltages that are then causing currents in the material [68]. These eddy current losses in the stator iron are linearly dependent on the material constant c_{Ed} and given by

$$P_{Ed} = c_{Ed} f_e^2 \hat{B}^2 d_{Fe}^2 m_{Fe}, \quad (5.15)$$

if the iron circuit is built up with isolated laminated sheets with a thickness of d_{Fe} .

However, for the evaluation of the hysteresis and eddy current losses the magnetic flux density in the iron path cannot be assumed to have a homogeneous distribution, wherefore 5.14 and 5.15 cannot directly be used. In order to calculate the iron losses accurately, the whole stator needs to be segmented into k parts with each having a constant flux density and a mass $m_{Fe,x}$. The whole iron losses P_{Fe} of each motor configuration can then be calculated according to

$$\begin{aligned} P_{Fe} &= P_{Hy} + P_{Ed} \\ &= m_{Fe,x} \left(c_{Hy} f_e \sum_x^k \hat{B}_x^{1.6} + c_{Ed} f_e^2 \sum_x^k \hat{B}_x^2 d_{Fe}^2 \right). \end{aligned} \quad (5.16)$$

This correlation can also be written as

$$P_{Fe} = k_1 \cdot n_e + k_2 \cdot n_e^2 \quad (5.17)$$

with k_1 being the linear and k_2 being the square loss factor, respectively and the motor speed n_e . These factors, which have been gained with empirical measurements on experimental test setups, are compiled in Table 5.2 for all configurations. In these measurements, the flux in all stator parts has been measured.

Configuration	(a)	(b),(c),(d)	(e)
k_1 [W/1000 rpm]	0.921	0.850	0.671
k_2 [W/(1000rpm) ²]	0.645	0.602	0.153

Table 5.2: Iron loss factors.

It can be seen that especially the square loss factor k_2 (due to the eddy current losses) is significantly lower for configuration (e) compared to the others. The main reason for that lies in the fully radial construction of that setup with an equally orientated lamination of the iron sheets. In

contrary, the concepts (a)–(d) are realised in temple motor design, where the stator parts have to be linked in an orthogonal manner and a continuous lamination is not possible. The due to this configuration increased losses in the junctions of the back iron and the claws are investigated in [7]. Furthermore, setup (e) has a lower iron mass, which is, however, compensated by the higher electrical frequency (due to $p = 2$). In total, as shown in Fig. 5.14, a clear advantage for the motor configuration (e) is given regarding the iron losses, especially for higher rotational speeds.

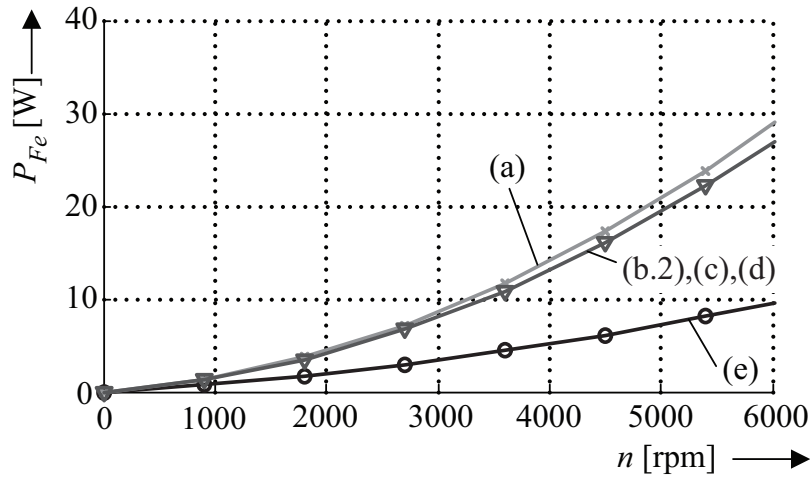


Figure 5.14: Total iron losses P_{Fe} of the presented motor configurations (a)–(e) in dependence on the motor speed n .

5.3.2 Losses in the Power Electronics

For the overall system comparison also the power electronics losses arising in the control of the investigated configurations must be taken into consideration. The calculation of the losses is carried out under the assumption that the respective power stages are either realised with integrated power modules as the one presented in section 2.3.2 or in case of the motor embodiments (a) and (e) with the discrete components that have the same loss characteristic as the ones integrated in the modules. With this, the switching losses can be evaluated based on the same switching loss energy data as in section 2.3.3. The compilation of the configuration depending switching and forward losses is depicted in Fig. 5.15. The calculation is carried out for a drive power of $P_D = 1200$ W and 70% bearing force. The speed is set to $n = 8000$ rpm.

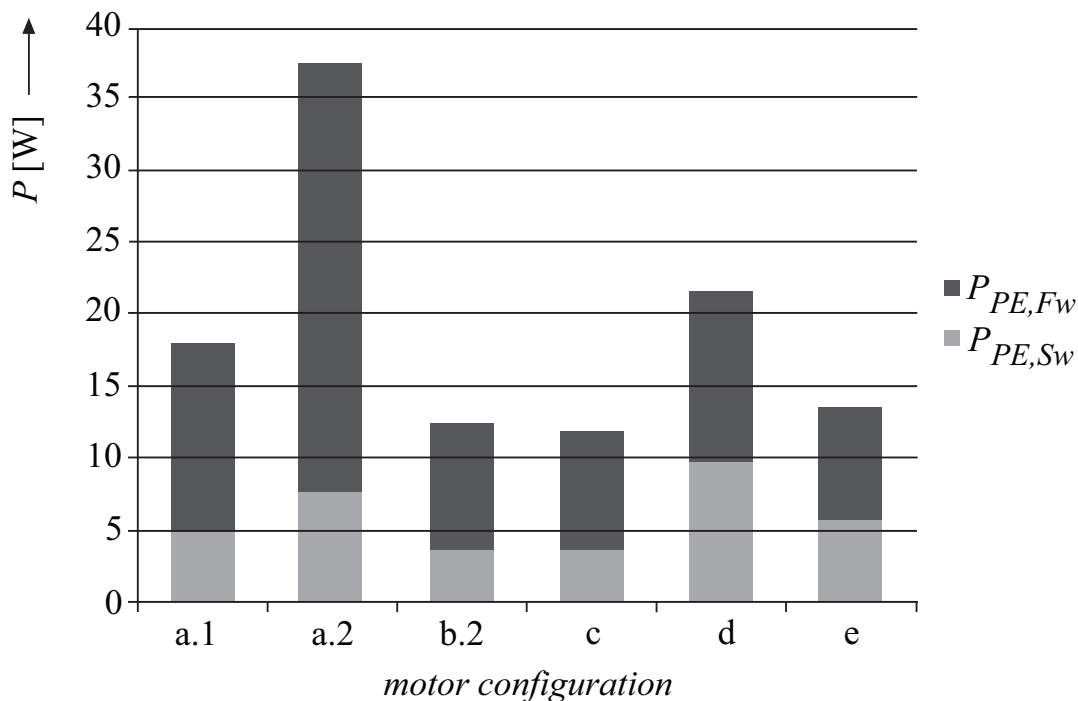


Figure 5.15: Switching losses ($P_{PE,Sw}$ and forward losses ($P_{PE,Fw}$) in the power electronics for a drive power of $P_{DR} = 1200$ W at 70% bearing force at a motor speed of $n = 8000$ rpm for the motor configurations depicted in 5.2, 5.5, 5.7, 5.9 and 5.11.

In addition to configuration (a.1) presented in section 5.2.1, the two-phase motor configuration is also analysed in conjunction with the interleaved half-bridge topology presented in chapter 2. This concept is referred to as (a.2) in the following. The combination of the drive currents in the common bridge leg leads to a significant increase in forward losses as can be seen in this figure. However, due to the modulation method presented in section 4.4.3 the maximum clamp voltage applicable to the drive phases is sufficient to ensure this operating point. The lowest power electronics losses among the investigated motor-controller configuration occur when the three-phase motor embodiment (c) is operated with the converter presented in chapter 2. In this setup, 11.85 W losses arise in the power transistors. This is 68% less compared to the losses arising in configuration (a.2).

5.3.3 Loss Distribution in Bearingless Motor System

As a base for the selection process of the best suitable configuration applicable for a certain application it is necessary that not only a loss distribution in the power electronics is present, even more an overview about the overall losses that occur in the motor–controller configuration is indispensable for a thorough comparison. For that reason, in Fig. 5.16 a compilation of the power electronics, the copper and the iron losses arising at the load point specified in the beginning of section 5.2 is shown. It can be seen that the total losses are lowest for configuration (e), followed by setup (c).

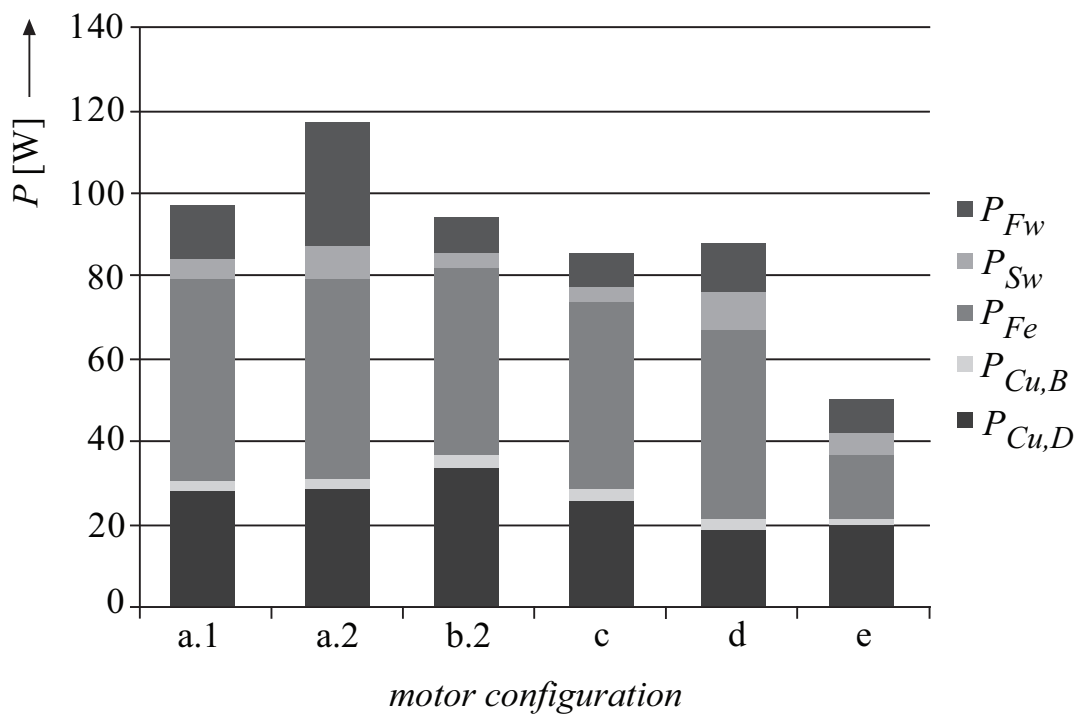


Figure 5.16: Overall loss distribution for the motor and converter configurations depicted in Fig. 5.2, 5.5, 5.7, 5.9 and 5.11. The shown losses are the copper losses in the drive system ($P_{Cu,D}$) and in the bearing system ($P_{Cu,B}$), the iron losses (P_{Fe}) as well as the switching losses ($P_{PE,Sw}$) and the forward losses ($P_{PE,Fw}$) in the power electronics.

5.3.4 Power Electronics Requirements

For the selection of the power semiconductors, the Volt–Ampere (VA) requirement is an important figure. In the past, a lot of research has

been carried out on the VA rating of various motor concepts [69], [70]. Thereby, different definitions for the VA ratings were established, such as the inverter peak VA rating, and the VA rating in terms of inverter peak voltage and rms current. For low speed applications or a at standstill, when the rotor is blocked and therefore high peak currents arise at the instant when the currents are applied to the windings, the definition of inverter peak current times peak voltage is most reasonable, since the semiconductors are facing the peak current value as worst case. In the context of bearingless motors, which are mainly used at higher rotational speed, the VA rating in terms of inverter peak voltage and rms current is more meaningful, because the silicon die sizing is based on thermal considerations and device losses rather than on peak currents. For a motor with m phases in the drive and bearing system the VA rating in a mathematical form is given by

$$P_{VA} = \sum_{i=1}^m \hat{U}_{i,cl} I_{i,rms}, \quad (5.18)$$

with the rms current $I_{i,rms}$ in the respective drive or bearing phase and the peak voltage $\hat{U}_{i,cl}$ at the phase clamps. Applying the phasor diagram in Fig. 4.9 and neglecting the small resistive voltage drop across the drive or bearing winding resistance, the required value of the peak phase voltage $\hat{U}_{i,cl}$ results in

$$\hat{U}_{i,cl} = \sqrt{\left(\omega L_i \hat{I}_i\right)^2 + \hat{U}_{i,ind}^2} \quad (5.19)$$

with the phase inductance L_i , the peak phase current \hat{I}_i and the amplitude of the induced voltage $\hat{U}_{i,ind}$.

The sinusoidal induced voltage in the drive phases is caused by the rotating field of the permanent magnet rotor. In [52] it is shown that electrical machines with m -phases can be represented as a two-phase equivalent machine. The voltages and currents are thereby represented in the dq -equivalent system [2]. If field oriented control is applied, the d -component of the phase currents vanishes [2]. Considering this, the q -component of the phase voltage vector $\underline{U}_{i,cl}$ is calculated to

$$U_{i,cl,q} = p_1 \Psi_{PM} 2\pi f_e = k_U 2\pi f_e, \quad (5.20)$$

where k_U is the voltage constant of the respective phase and $\underline{\Psi}_{PM}$ is the flux linkage that is calculated with the number of windings w and the number of pole pairs p according to

$$\underline{\Psi}_{PM} = \frac{w}{p} \xi \underline{\Phi}_{PM}. \quad (5.21)$$

In 5.21, the winding factor ξ specifies the percentage of the magnetising flux Φ_{PM} that is gathered by the winding system [71]. As explained in [2], the field in the air gap of a bearingless slice motor is sinusoidally distributed with a maximum flux density \hat{B}_{PM} . Based on this, the absolute value of the rotating magnetising flux $\underline{\Phi}_{PM}$ is calculated to

$$\Phi_{PM} = 2 l_r r_r \hat{B}_{PM}. \quad (5.22)$$

Here, l_r represents the length and r_r the radius of the rotor.

Due to the fact that the magnetising flux $\underline{\Phi}_{PM}$ is caused by a permanent magnet, the d -component of the field oriented current \underline{I}_i does not contribute to the torque and is therefore set to zero. Consequently, the torque T is only dependent on the q -component of the current and the torque constant k_M [52]:

$$T = k_T I_{i,q}. \quad (5.23)$$

Assuming an operation of the motor without any losses, the following equivalent can be applied where P_e is the electrical and P_m the mechanical power, respectively:

$$\begin{aligned} P_e &= P_m \\ \frac{m}{2} U_{i,cl,q} I_{i,q} &= T 2\pi f_m \\ \frac{m}{2} k_U 2\pi f_e I_{i,q} &= k_T I_{i,q} 2\pi f_m \end{aligned} \quad (5.24)$$

Herein, the electrical frequency f_e and mechanical frequency f_m are coupled by the number of pole pairs of the drive system according to [2]:

$$f_e = p_1 \cdot f_m. \quad (5.25)$$

Combining 5.24 and 5.25 leads to

$$k_U = \frac{2 k_T}{p_1 m} \quad (5.26)$$

This shows that with the knowledge of the number of pole pairs p_1 and drive phases m along with the current–torque constant k_M , which is obtained by simulations, the voltage constants of the presented motor configurations can be calculated.

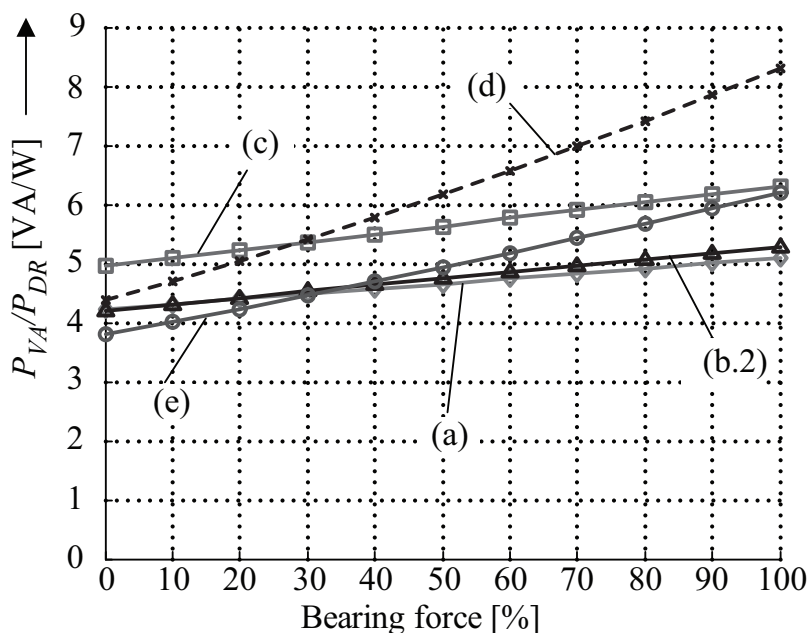


Figure 5.17: VA requirement of the presented motor configurations (normalisation basis: rated drive power $P_{DR} = 1200$ W).

For the configurations (a)–(c), which feature separated drive and bearing systems, different peak phase voltage requirements can be calculated for both systems. However, due to the availability of only one common dc–link voltage of the converter, the higher voltage requirement (which occurs for the drive system) has been chosen for the peak clamp voltage $\hat{U}_{i,cl}$. This also offers the benefit that the bearing system has a broad stability margin to compensate for external disturbances. For the configurations (d)–(e), which generate the levitation forces and the torque in the same windings, a certain stability margin for the bearing system has to be added explicitly in order to also guarantee a safe operation. Measurements on laboratory prototypes have shown that the voltage requirement has to be increased by a factor of 1.3 for the considered speed

range, which is already taken into account for this comparative evaluation. For higher rotational speeds this margin would have to be increased even more and it was observed experimentally that for a dc-link voltage of 325 V the configurations (d) and (e) cannot be operated above 8000 rpm anymore. Additionally, for configuration (e) the maximum achievable speed is also limited by the digital control, which has to deal twice the electrical frequency due to $p = 2$ as compared to the other topologies.

The VA requirements scaled to the rated mechanical power ($P_{DR} = 1200$ W) are depicted in Fig. 5.17 for the different motor designs. One can see that the required bearing forces have an impact on the VA requirement of the motor. This is especially the case for motor (d), where at 100% bearing force, which equals 20 N, the VA requirement is nearly doubled as compared to zero force. If only the drive system is taken into account (values at 0% bearing force), configuration (e) demands the lowest VA requirement. However, this condition does not arise in normal operation of a bearingless slice motor since levitation forces are always needed in order to safely operate the system. For the considered operating point with 70% bearing forces, which is a typical value for pump applications, motor configurations (a) and (b.2) are the most efficient solutions regarding the necessary VA requirement of the converter.

5.3.5 Cost Related Factors

As mentioned in section 1.1.3, bearingless slice motor pump systems are getting more and more targeted for applications, where mass production becomes feasible. Therefore, additional cost-related factors must be taken into consideration for a complete comparison. In table 5.3 a qualitative comparison of the concepts is given for these factors in addition to the previously discussed performance indices (power losses and VA requirement).

As has been shown in section 5.3.3, configurations (c) and (e) are the favourable ones, if only the losses in the motor and the power electronics are considered. At the chosen operating point the overall losses occurring in configuration (e) are 42.9% of those resulting in configuration (a) operated with the interleaved half-bridge topology. In terms of VA requirements, the motor setups (a) and (b.2) have been found to be preferable for applications, where significant bearing forces occur, e.g. for pumps. On the other hand, configuration (d) has the highest VA require-

Configuration	(a)	(b.2)	(c)	(d)	(e)
Power losses	-	-	√	√	+
VA requirement	+	+	√	-	√
Copper/Iron mass	-	-	-	-	+
Realisation effort	√	√	√	√	+
Control complexity	+	+	+	-	-
Scalability	+	+	+	-	-

Table 5.3: Qualitative comparison of the different bearingless slice motor concepts (a)–(e).

ments and therefore leads to the largest power electronics volume. The comparison of the copper and iron mass, which is required to realise the different motor embodiments, is lowest for configuration (e). The radial design of the iron circuit, which does not need additional vertical claws, as they are required in the temple motor configurations (a)–(d), results in an iron mass which is almost half as compared to the other concepts.

Looking at the embodiments from a manufacturing perspective and with this considering the necessary realisation effort reveals motor (e) as the most promising solution. This mainly emerges from the disc shape structure of this configuration, which offers certain production advantages. First, the four identical coils can directly be wound on the stator claws in one step, which simplifies the manufacturability. In addition, the iron circuit can be realised with a horizontally laminated iron stack. Due to the absence of additional vertical claws the manufacturing effort is clearly reduced compared to the temple motor configurations (a)–(d). Finally, the disc shape setup also offers the possibility of integrating the power electronics part in the motor while still keeping the thereby resulting total case volume in the range of the temple motor configurations without integrated power electronics. In addition, this greatly reduces the cabling effort. Taking all the before mentioned issues into account, the realisation effort clearly is the lowest for this configuration. However, the shape of the iron circuit with its wide-spread claws demands a more sophisticated sensor concept for the position detection of the impeller. Compared to configurations (a)–(d), where the position sensors are mounted in between the claws, the therefore necessary space is not available anymore in this configuration due to the shape of the iron claws. Its design also influences the design of the pump impeller in terms of hy-

draulic efficiency. This fact also strongly limits the applicability of this concept in high pressure/flow applications. In mixer applications, where on the one hand speeds below 4000 rpm and on the other hand the torque demand is higher compared to pump applications this concept seems to be a promising solution. Since also the space available for the placement of the motor and the power electronics below the mixer tank is limited a compact motor concept such as configuration (e) is favorable.

The control complexity of the presented motor embodiments highly depends on the chosen winding configuration. The concentrated coils contribute to a coupled and highly nonlinear force and torque generation and thus require a more complex control algorithm in order to safely operate the motor [61]. In configurations (a)–(c), the control of the drive and bearing system can be done independently (see chapter 3.1). This results in a less complex control structure as for motors (d) and (e).

As explained in section 5.3.4, the scalability of the motor configurations towards higher speeds and pressure is best for configurations (a)–(c). This results from the independent drive and bearing system, where due to the utilisation of the same dc-link voltage the bearing system usually features a large dynamical voltage margin to compensate for external disturbances. In contrast, for configurations (d) and (e) the stability margin for the bearing system has to be added explicitly in order to guarantee a safe operation. This voltage margin together with the maximum available dc-link voltage is the limiting factor for the maximum achievable drive speed of these concepts. As mentioned in section 1.1.3, in today's semiconductor applications a strong demand arises for pumps with high pressure ratings. For these applications motor configurations (d) and (e) cannot be considered as suitable solutions due to their limited speed capability.

Summing up, it can be stated that configuration (e) is highly interesting for future cost-sensitive bearingless motor applications such as pumps for plating industry, mixers for biotechnology processes, or heat and cooling pumps where less stringent pressure and therefore speed requirements (remark: the output pressure increases quadratically with the speed of the impeller) are given than in semiconductor applications. In the latter area, configuration (a) still seems to be the most preferable solution.

The advantage of the converter topologies (b), (c) and (d) is that two intelligent three-phase power modules can be applied. As has been shown

in section 4 embodiment (a) can also be operated with a three-phase converter topology. However, doing this leads to significantly higher losses in the power electronics as shown in the previous section. As an imminent property of the motor embodiments shown in (d) and (e) the rated current of all windings are showing the same value which leads to a good utilization of the power electronics. In contrary, for the configurations depicted in Fig. 4 (a)-(c) separate winding systems for force and torque generation are used. This results in different current ratings for the drive and bearing windings and hence leads to an unbalanced utilisation of the semiconductor devices if identical three-phase power modules are utilised.

5.4 Summary

In this chapter two-, three- and four- phase bearingless slice motors have been comparatively discussed based on performance indices in order to find the most suitable motor embodiment for more cost sensitive application areas of next generation bearingless pump systems. The comparison has been carried out for a typical pump operating point (rated mechanical drive power 1200 W, bearing forces in the range of 0–20 N). The performance indices have been defined as the occurring power losses in the converter and the motor, the power electronics VA requirements arising in the chosen operating point as well as cost related manufacturing issues (such as copper and iron masses, realisation effort in consideration of mass production, control complexity and scalability towards higher speed and pressure ranges). The comparison has not revealed a clear superior concept in all aspects, but has given a better insight to the specific attributes and possibilities of each concept.

Generally, it can be stated that the two-phase motor configuration realised as temple motor in conjunction with the existing bearingless slice motor pump is not the superior concept in terms of losses arising in the motor and the power electronics. Especially, when the two-phase motor concept is operated with the interlaeved half-bridge topology the losses in the power electronics are significantly higher compared to an operation of that motor topology with the conventional half-bridge topology as can be seen in Fig. 5.15. The comparison has rather revealed that the three-phase configuration in temple form (c) is the most effective configuration among the concepts with separated drive and bearing systems with clear

advantages in terms of maximum achievable impeller speed and thus pump pressure compared to concepts with combined drive and bearing systems realised either in planar or temple design.

On the other hand, the four-phase motor configuration (e) seems to be a promising concept for future cost-sensitive applications in the low pressure and low/medium speed range, e.g. pumps for plating industry, mixers for biotechnology processes or eventually even for heat and cooling pumps if they can be produced in large enough numbers. The advantages of this concept in terms of small iron and copper masses and easy manufacturability are mainly arising from its radial construction. In addition, the compact design allows the integration of the power electronics in the motor housing with a resulting volume comparable to that of the temple motor design without integrated electronics. However, for high pressure applications in upcoming semiconductor applications, where speeds above 8000 rpm are demanded, this concept cannot be considered anymore due to its inherent speed limitations.

Chapter 6

Conducted Emissions

6.1 Introduction

In power electronics, there exist two main reason for the necessity of an input filter:

- Protection from electromagnetic influence of devices that are in close proximity of the equipment under test (EUT).
- Protection of malfunction of the that EUT which is caused by disturbances of devices in the surrounding [72].

The noise caused by the converter can be separated into two phenomena, namely common mode (CM) and differential mode (DM) noise. In the following, only the abbreviations CM and DM will be used. The aim of the filter is to damp the CM and DM currents that occur in the converter sufficiently. In a first step, this can be partly achieved by a properly designed layout of the power stage [73] which is optimised regarding Electromagnetic Compatibility (EMC) considerations. Furthermore, an increase in the switching time and due to that slower rise and fall times of the voltages and currents results in a reduction of the noise level. However, as a consequence of the use of integrated power modules (see section 2.3.2) the gate resistors and thus the switching behaviour of the IGBT's cannot be influenced.

Another approach that is broadly discussed in literature is the modulation of the switching frequency in order to decrease the maximum amplitude of the voltage spectrum. With this, a more broadband distribution of the spectral lines can be achieved. The modulation of the switching frequency with a sine-, triangle- or saw-tooth modulated signal [74] and the addition of harmonics to the carrier signal [53] are, besides randomly varying the switching frequency [75], [76], the most common methods. However, they are seldom applied in practice. One reason for this is that in order to comply with the norms the average value as well as the short-term average value must fulfill with the threshold values. For the calculation of the spectrum the average values are always considered. This issue is explicated in [77]. There it is shown that a significantly lower – as one would expect – level reduction is achieved when only the short time average values are considered. Due to the nonlinearities that are caused by the differing rise- and fall-times of the switching slope the resulting levels can only be estimated with numerical methods.

In most cases the damping of the CM and DM disturbances, which are caused by the switched voltages and currents, is not sufficient to fulfill the norms when using the previously described methods. Generally, for bearingless pump systems, the variation of the switching frequency under operation with the aim of reducing the common mode noise is not an option since the control restrictions that apply for the bearing system exclude the application of such methods (see section 3). Thus, passive components (resistors, inductors and capacitors) have to be used for the lowpass filtering. Also a combination of those together with active components (switches) could be considered. This however will not be further taken into account in this work due to its increased complexity and thus lower applicability for industrial designs compared to passive solutions.

In the hereafter presented analysis of the common mode behaviour of the bearingless pump system the following assumptions are made:

- The maximum length of the power cable between the motor and the converter is limited to 20 m. This corresponds to the conditions arising in semiconductor fabs where it is more and more the case that the control part of the process equipment is separated from the chemical processing part. This demands long cables between the controller and bearingless slice motor which is placed in

the chemical cabinet.

- The analysis is carried out with a two-phase bearingless slice motor (see section 5.2.1) operated by the interleaved half-bridge topology introduced in section 2.2.3.
- For next generation bearingless pump systems it is mandatory that they can be connected to the single- as well as three-phase mains.

6.2 Line Impedance Stabilisation Network

When testing the Equipment Under Test (EUT) for compliance with conducted emission limits it has to be connected to the mains via a Line Impedance Stabilisation Network (LISN). Since in real world environments the amplitudes of conducted emissions are strongly varying depending on the characteristics of the connected mains it is of major importance to have a normed equivalent circuit of the mains in order to gain reproducible measurements. With the help of a LISN, the impedance seen by the equipment under test is well defined since the LISN ensures a high frequency decoupling of the device under test and the mains. The schematic of a LISN is shown in Fig. 6.1. In Fig. 6.2 the connection scheme for single- and three-phase measurement is shown. In the hereafter carried out measurements the output of the LISN is connected to a test receiver of the type Rohde & Schwarz ESPI3.

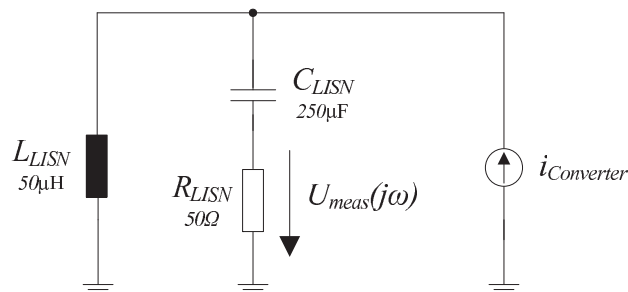


Figure 6.1: Simplified LISN high-frequency model which can be considered for calculation of conducted emissions through calculations and simulations. The EUT is replaced by a constant current source $i_{Converter}$.

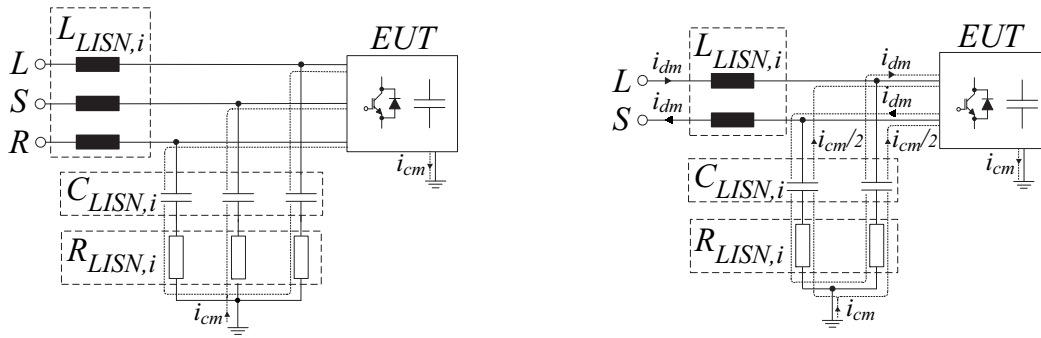


Figure 6.2: Equivalent circuit of one and three phase LISN with $R_{LISN,i} = 50\Omega$, $L_{LISN,i} = 50\mu\text{H}$ and $C_{LISN,i} = 250\mu\text{F}$.

6.3 DM Filter Design

In advance to the CM filter design, the DM filter components must be known since these components influence the behaviour of the CM current propagation paths and are therefore required for a proper CM modeling procedure.

In [77] it is explained how the diode rectifier causes the transition of CM into DM noise and DM into CM, respectively. Not only a dominant CM but also a dominant DM disturbance can be transferred into the other one. Due to differing junction capacitances of the diodes the conversion of CM disturbances into DM disturbances arises. In case that all diodes are blocking, the switched CM current generates an ac voltage at the junction capacitances. The unbalance of the junction capacitances leads to a resulting differential mode signal if the diodes are only conducting for a short period of time and are switched off right away afterwards. This shows that in topologies that feature a passive diode rectifier at the input a strict separation of the CM and DM noise cannot be performed.

Due to the large dc-link capacitor in the herein employed design (see section 2.3.7) only a small current ripple arises in the input current of the converter. Thus, the DM noise can be damped without the use of explicit DM inductors. In this design, three DM capacitors are placed towards the mains. In addition to that, a balancing C is placed in the dc-link as can be seen in Fig. 6.10. The effect of these capacitors is shown in Fig. 6.12. As can be seen there, the DM attenuation is sufficient with the use of capacitors only.

6.4 CM Filter Design

In the following, a CM model of the bearingless pump system is derived that serves as the base for the design of the CM filter stage.

6.4.1 Modeling of the Inverter

For an investigation of the CM disturbances arising in the converter the sources that cause these disturbances must be known. Furthermore, the distribution paths of these currents have to be investigated. For that, an equivalent CM noise propagation model must be developed in order to analyse these parameters. As the CM currents circulate through parasitic distributed capacitances, which are very complex to model as distributed parameters, simplified lumped elements are used to model the main current paths. However, this sets a restriction on the frequency range in which the model is valid. An analysis of the converter has led to the paths shown in figure 6.3. There, the path of the CM currents is closed through the parasitic capacitances C_{I-GND} and C_{O-GND} between the heat sink, the output capacitor and the elements of the power circuit.

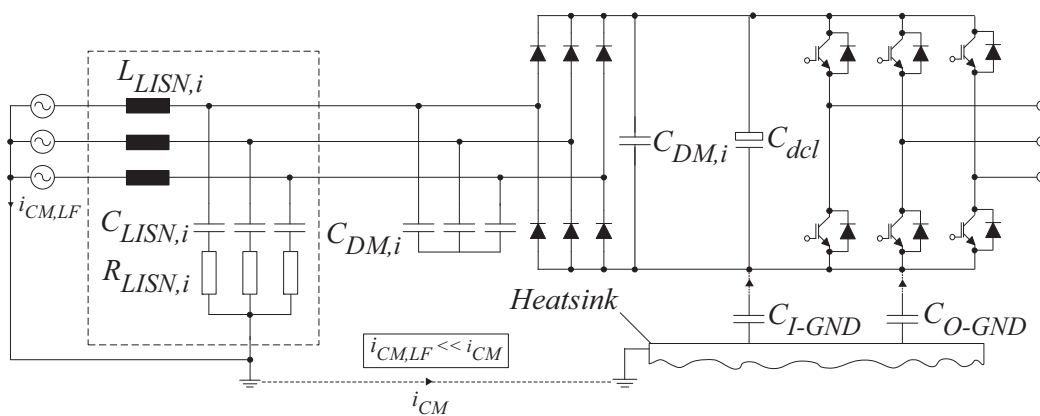


Figure 6.3: Distribution paths of the CM currents in the converter.

6.4.2 Estimation of Model Parameters

Assuming, due to $L_{LISN,i}$, at high frequencies an ideal decoupling of the EUT to the mains, and a perfect coupling with the test receiver through $C_{LISN,i}$ is achieved in a simplified consideration, the resulting high frequency equivalent circuit is shown in Fig. 6.4 where only

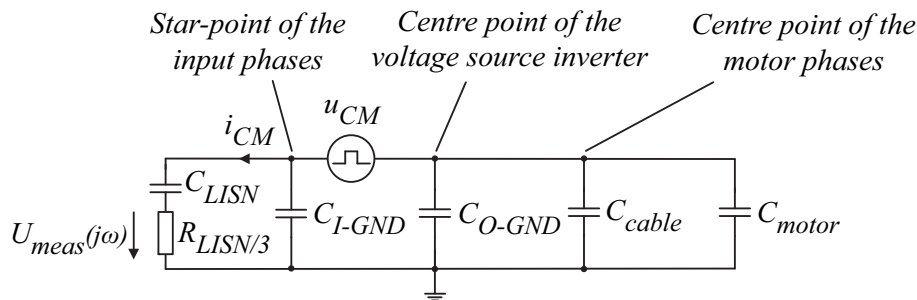


Figure 6.4: CM noise propagation model for the interleaved half-bridge topology converter: Component values: $R_{LISN} = 50 \Omega$, $C_{LISN} = 250 \mu\text{F}$, $C_{I-GND} = 2.28 \text{ nF}$, $C_{O-GND} = 1.61 \text{ nF}$, $C_{cable} = 11.34 \text{ nF}$, $C_{motor} = 450 \text{ pF}$.

low frequency components ($i_{CM,LF}$) circulate to the mains. The different emission sources are modeled as a single common mode disturbance source u_{CM} which shifts the potential between the parasitic input capacitor C_{I-GND} and the parasitic output capacitor C_{O-GND} according to the chosen modulation method. Thus, the CM current circulating in the system flows through both parasitic in- and output capacitors towards earth and by that causes the noise level measured at the input of the converter. The three resistors R_{LISN} of which each has a value of 50Ω are in series to the three input phases. Due to the fact that they are in parallel to each other, the resulting value seen by the common mode current is $R_{LISN}/3$. The modeling of the capacitance C_{cable} is discussed in the next section. The latter along with the parasitic motor capacitance C_{motor} completes the CM distribution path in the system. For the measurement and estimation of the relevant parasitic capacitances (C_{I-GND} and C_{O-GND}) a series of impedance measurements was performed with a precision impedance analyser Agilent 4294A. In order to evaluate the capacitance C_{I-GND} an impedance measurement is carried out with disconnected motor cables and short-circuited input connectors. This leads to a high frequency equivalent circuit representing a resistor, an inductor and a capacitor in series, from which only the capacitance value is used in this design procedure (cf. Fig. 6.5) in the chosen frequency range from 1 kHz to 60 MHz. It has a value of $C_{I-GND} = 2.28 \text{ nF}$. As explained in [78], the wiring, PCB parasitics and various component inductances (e.g. of the power module) can be neglected due to their low value and consequently their influence in the frequency range above 30 MHz that is not accounted in this work. For the measurement of the parasitic output capacitor C_{O-GND} (cf. Fig. 6.6) the six output terminals are short

circuited and the capacitance is then measured towards the heat sink. In this measurement, the capacitance C_{I-GND} is in series with C_{O-GND} and thus contributes to the measured value. The resulting values are $C_{C,O-GND} = 1.61$ nF, $R_{C,O-GND} = 1.16$ Ω and $L_{C,O-GND} = 162.5$ nH. Again, only the capacitor $C_{C,O-GND}$ is used in the analysis of the CM behaviour.

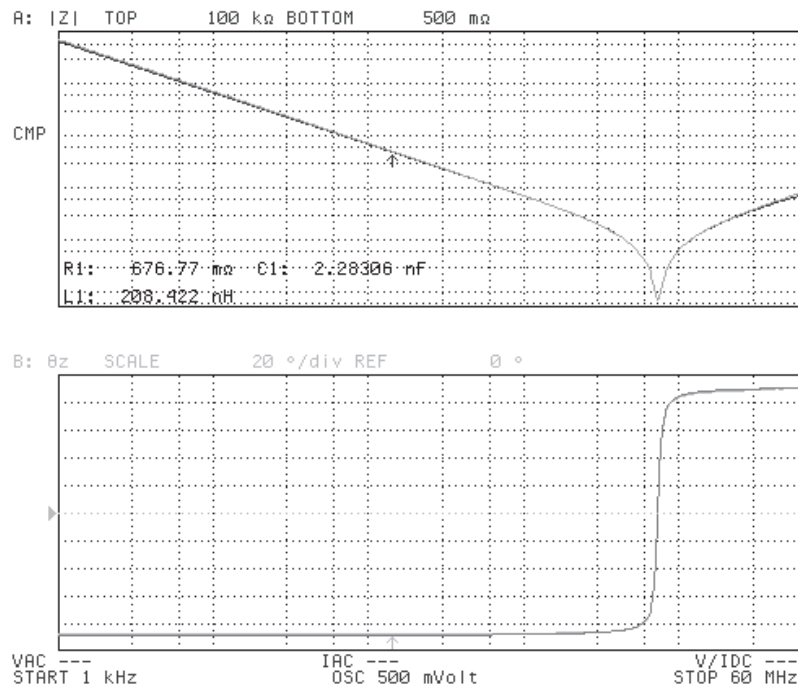


Figure 6.5: Absolute value of the impedance characteristic of the parasitic input capacitor C_{I-GND} .

6.4.3 Modeling of Motor Cable

In applications such as the ones described in section 1.1.3 the controller and the bearingless pump are generally not placed next to each other. Often, the controller has to be placed outside of the clean room cabinet due to very little space available inside. Thus it is common practice to locate the controller in the basement of the semiconductor fab. The distance between the controller and the pump can thereby become up to 20 m. Such long cables are a known source for the distribution of common mode noise that is responsible for the malfunction of the systems. The motor cable must therefore be included in the design process of the filter. As a consequence of this, this section deals with the modeling of

CONDUCTED EMISSIONS

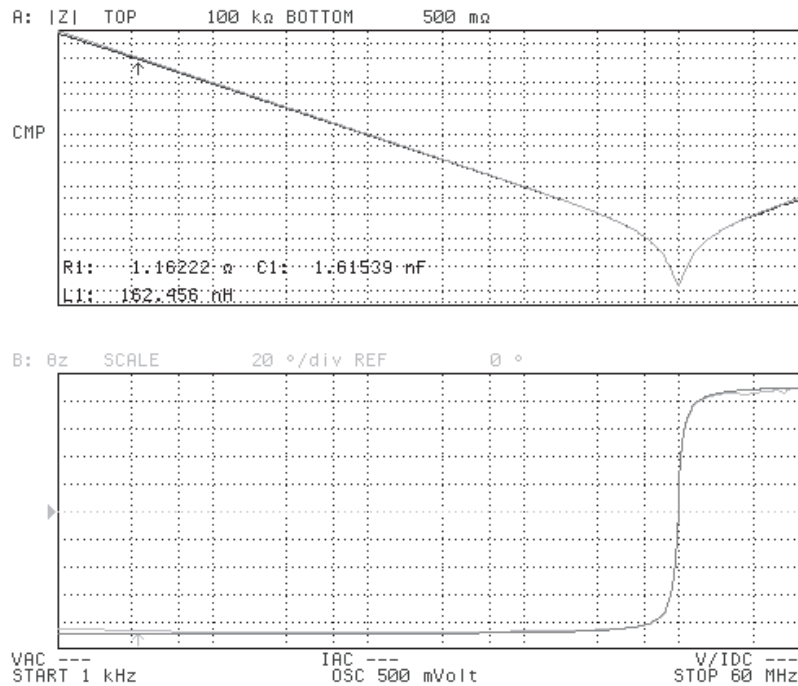
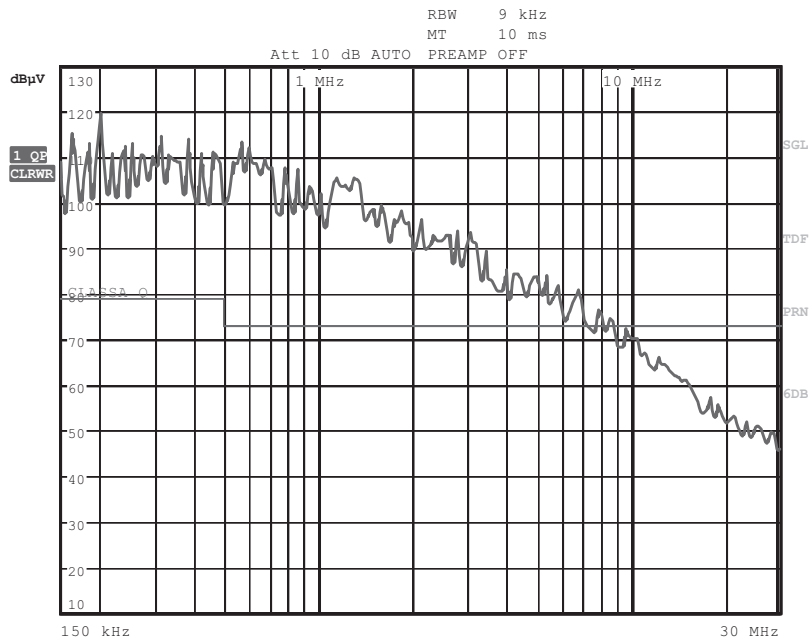


Figure 6.6: Absolute value of the impedance characteristic of the parasitic output capacitor C_{O-GND} .

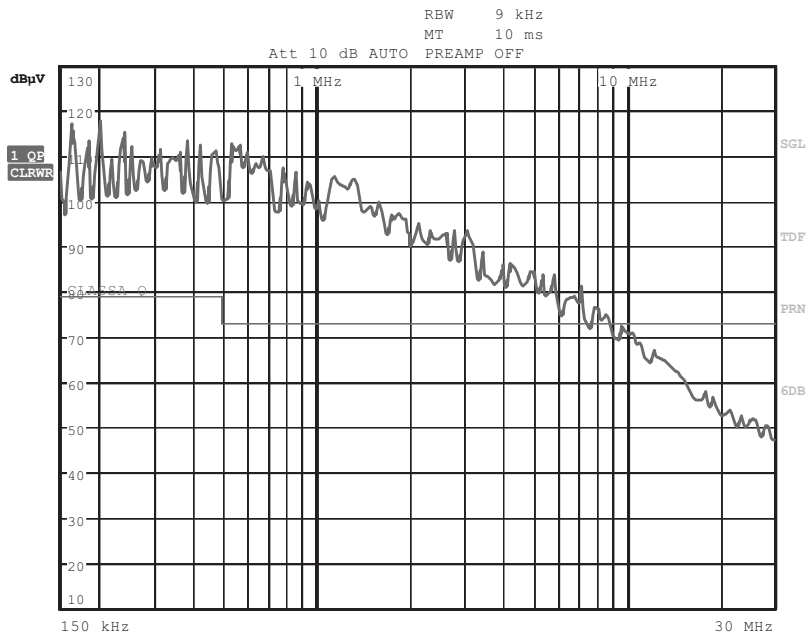
the motor cable. As a preliminary work one must first define how the eight winding leads of the motor are connected to the power stage of the controller. As described in 2.2.3 the interleaved half-bridge topology has three output connectors for the drive windings and additional three output connectors for the bearing windings.

Therefore, it shall be investigated if connecting the motor with an eight wire cable to the controller generates higher CM noise than employing a six wire cable. The latter requires that the junction of the drive and bearing phases is made in the motor and not at the output of the converter. Measurements investigating both configurations lead to the results shown in Fig. 6.7. As can be seen there, both configurations result in similar CM levels. Thus, in the following investigations, a six wire cable is employed for the connection of the motor to the controller. The measured lumped capacitance of this cable used in the following design is $C_{cable} = 11.34 \text{ nF}$.



(a)

Comment:
Date: 15.SEP.2008 11:18:23



(b)

Comment:
Date: 15.SEP.2008 11:39:15

Figure 6.7: (a) 8 wire cable with a junction of the two drive and bearing phases at the controller, (b) 6 wire cable with a junction for the two drive and bearing windings in the motor.

6.4.4 Modeling of Bearingless Slice Motor

The modeling of the high frequency behaviour of three phase asynchronous electric motors is widely discussed in literature [79]. In these machines, the windings are usually close to the housing due to the compact design. Similarly, this is also the case for bearingless slice motor pump systems, where high pressure is put on volume optimisation. However, this trend towards more compact designs increases the presence of distributed capacitances between the windings and the casing. Their value is significantly higher than that of the stray capacitances between the windings. The pulsed CM voltages that are applied to these capacitances then generate CM currents. These currents deteriorate the mechanical bearings through arcing currents and they also find their way through earthing connections. Furthermore, these currents might generate voltages induced in the shaft of conventional asynchronous or synchronous machines that, if the shaft is connected to other electrical devices, generate CM currents in them [80]. For this reason, a shielded cable is used to transmit the position and speed signals of the motor to the controller which prevents these signals from induced voltages and currents that often cause destructive voltage stress and safety hazards in non-shielded cables close to motor cables [81]. Due to the absence of ball bearings and the long connection cables between the motor and the power electronics in a magnetically levitated motor the exact knowledge of the small signal parameters of the motor is not of such high importance as it is the case for standard three-phase motors. Furthermore, the fluids to be pump are nonconducting and thus no dielectric coupling is present. Already for standard three-phase machines the geometrical complexity of the system limits the applicability of simple analytical models to describe the motor parameters. This is even more the case for bearingless slice motors where the standard two-phase configuration (see section 5.2.1) features two different winding systems with multiple coils. For solving such problems three dimensional electromagnet field simulations could be an option. Generally, this results in large computational effort and is therefore employed in rare cases. Impedance measurements [82], [83] are still the most widespread technique for the evaluation of motor parameters.

Most of these circuits are dealing with the mapping of high order resonances above 30 MHz as well as skin effect and bearing currents. In [79], [84], for example, higher frequency models for three-phase motors are proposed. Since the simulation of HF resonances does not fall into the

scope of this work a more simplified model can be chosen. An approach into that direction can be found in [85] where different models for the study of CM currents are presented.

Taking into account the – compared to the parasitic capacitances in the motor – relatively large value of the cable capacitance, the corresponding capacitances in the motor do not play a significant role in the frequency range of interest (up to 30 MHz). Generally, their values are in the pF range. However, for fully integrated drive systems, where the electronics is directly mounted on the motor housing, and thus no motor cables are present, the detailed modeling of the HF motor parameters is of higher importance than in the herein analysed configuration. Due to the long motor cable and the therefore resulting large capacitance value of the cable compared to the motor capacitance, the motor is modeled in the following with a lumped capacitance of $C_{motor} = 450$ pF that is obtained by measurements.

6.4.5 Modeling of CM Source

The remaining parameter in the equivalent circuit in Fig. 6.3 that is demanded for the prediction of the CM noise level is the spectrum of the voltage source u_{CM} . Before one can obtain this spectrum, the topology specific wiring of the converter and the motor depicted in Fig. 6.8 must be investigated in order to specify the voltages that contribute to the generation of u_{CM} . There, the converter together with the drive phases of the two-phase motor is depicted. The relevant voltage/current equations for this setup are

$$\begin{aligned}
 u_{SB,D,1} &= i_{D,1} (R_c + R_{D,1}) + \frac{d}{dt} i_{D,1} (L_c + L_{D,1}) + u_n \\
 u_{SB,D,2} &= i_{D,2} (R_c + R_{D,2}) + \frac{d}{dt} i_{D,2} (L_c + L_{D,2}) + u_n \\
 u_{CB,D} &= i_{CB} R_c + \frac{d}{dt} i_{CB} L_c + u_n.
 \end{aligned} \tag{6.1}$$

With $R_{D,1} = R_{D,2} = R_D$ and $L_{D,1} = L_{D,2} = L_D$ and since $i_{D,1} + i_{D,2} + i_{CB} = 0$, (6.4.5) can be written as

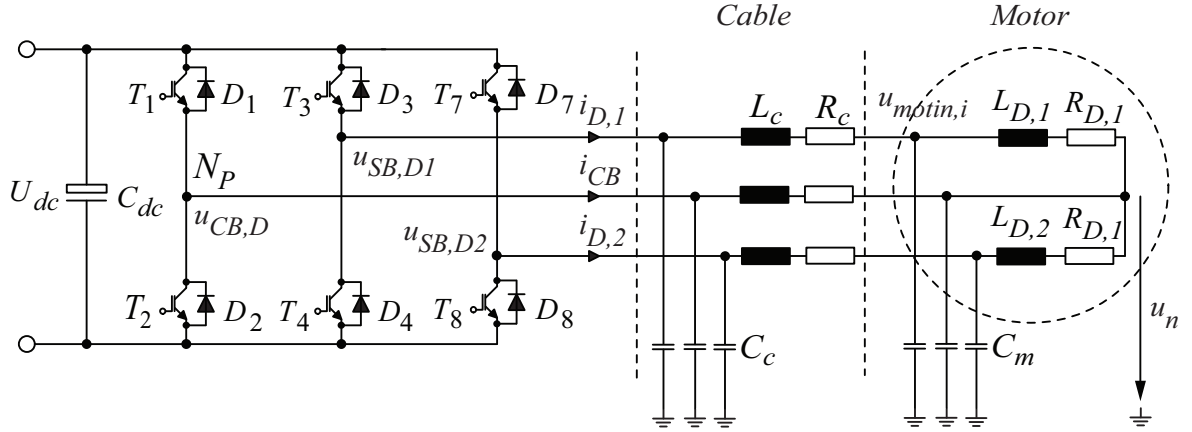


Figure 6.8: Three-phase voltage source inverter with two-phase motor drive winding configuration.

$$u_{SB,D,1} + u_{SB,D,2} + u_{CB,D} = - \left(i_{CB} R_D + \frac{d}{dt} i_{CB} L_D \right) + 3 u_n. \quad (6.2)$$

Thus, the neutral voltage results to

$$u_n = \frac{u_{SB,D,1} + u_{SB,D,1} + u_{CB}}{3} + \frac{1}{3} \left(i_{CB} R_D + \frac{d}{dt} i_{CB} L_D \right). \quad (6.3)$$

In order to find an adequate equation for the common mode voltage u_{CM} the next step is to simplify eq. 6.4. For that a closer look at the parasitic capacitances of the cable and the motor is required. The measured resulting common mode capacitance C_c of the cable is 12 nF, whereas the common mode capacitance of the motor equals only $C_m = 350$ pF. This results in a multiple of 30 between these two capacitors. Thus, this large difference in capacitance can be utilised for the desired simplification. The idea behind this simplification is that the resulting common mode current at the output of the converter is mainly determined by the cable capacitance towards PE. If that was the case only the part

$$u_{CMout} = \frac{u_{SB,D,1} + u_{SB,D,1} + u_{CB}}{3} \quad (6.4)$$

of eq. 6.4 needs to be considered for the approximation of the com-

mon mode voltage and the asymmetry caused by the two-phase motor configuration would only have a minor influence.

The voltage drop across one phase of the cable responsible for the generation of the common mode current can be neglected in view of the common mode voltage (6.4) at the output of the converter. This is also valid for the herein discussed two-phase motor topology with an unsymmetric winding configuration. Assuming a nominal load current of 10 A peak with a measured cable resistance per phase of 1.3Ω results in a resistive voltage drop of 13 V compared to the common mode voltage u_{CMout} of approximately 110 V. In order to prove this assumption a simulation of the three voltages (cf. Fig. 6.9) u_{CMout} , u_{motin} and u_n has been carried out.

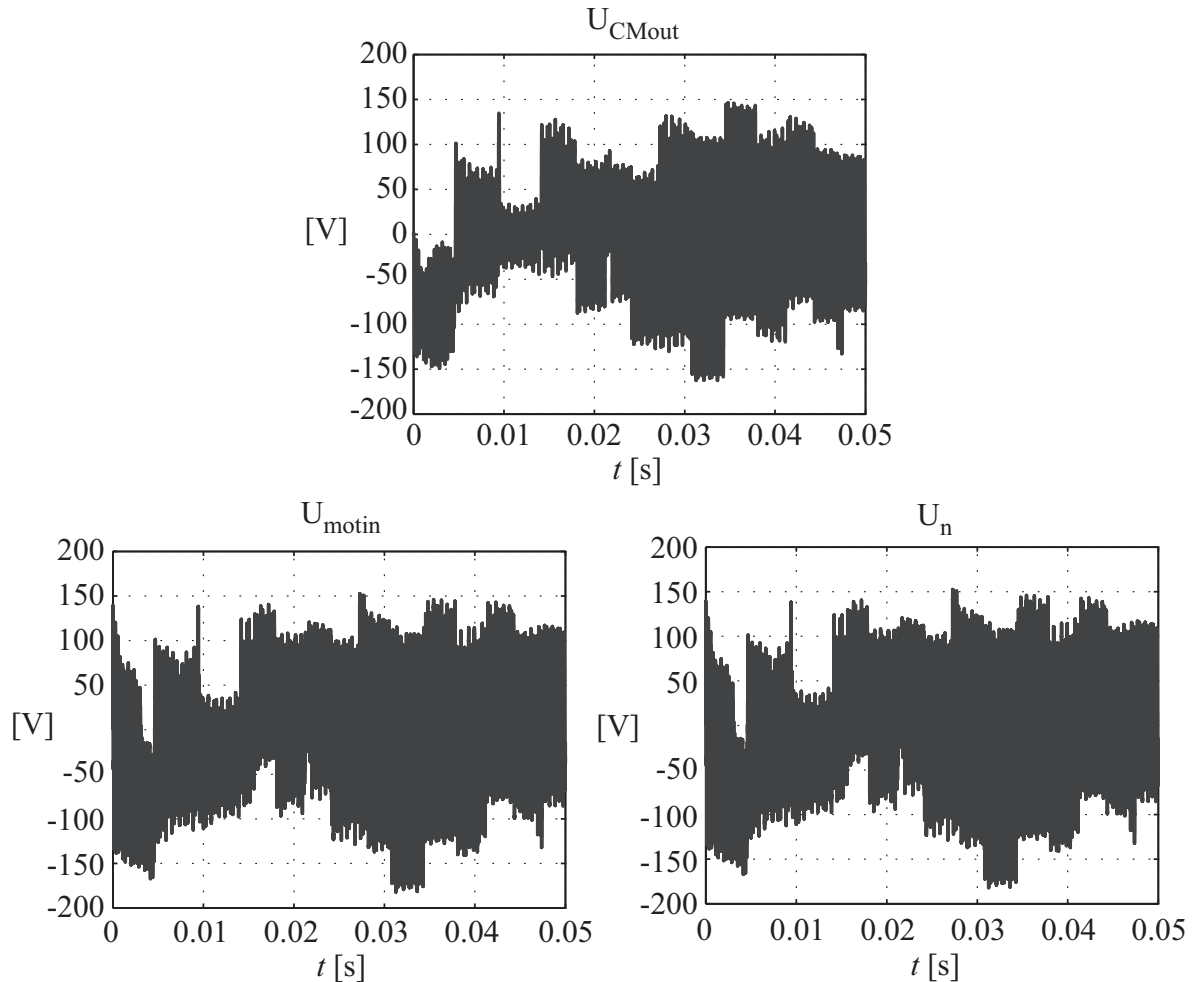


Figure 6.9: Common voltages U_{CMout} , U_{motin} and u_n

As can be seen in this figure, the common mode voltages u_{motin} and

u_n are virtually identical. Although, u_{cmotin} and u_n differ from u_{CMout} , the resulting common mode is mainly determined by the compared to the motor parasitics large cable PE capacitance. This is considered as a proof for the intended simplification and allows for defining the resulting common voltage of the bearing and drive system according to

$$u_{CM,tot} = \frac{u_{SB,D,1} + u_{SB,D,2} + u_{CB,D} + u_{SB,B,1} + u_{SB,B,2} + u_{CB,B}}{6}. \quad (6.5)$$

This shows, that the common mode voltage $u_{CM,tot}$ of the converter is the average value of the six switched phase voltages in the converter.

In case of different cable and machine parameters the beforehand suggested simplification approach needs being reconsidered and the effect of the two-phase motor configuration needs to be taken into consideration in more detail. The measurements prove for as much the above model as noise CE measurements at nominal voltage and connected output cable did not show any difference in the noise level on whether the machine was connected or not. In case no machine connected the asymmetric winding configuration is not present at all and thereby provides an additional proof of the model.

6.5 Filter Design

As mentioned in chapter 1 the available space in a clean room is already very limited and even more pressure will be put on that issue in the future. Thus, care must also be taken on the overall filter volume in the design process. Due to the required applicability of the converter at the single- and three-phase mains, the filter must be designed for three-phase operation.

Keeping this in mind, the design process is focused on the placement of the majority of the filter components in the dc-link and as a matter of fact, behind the diode rectifier as shown in Fig. 6.10. This allows for better utilising the filter volume since only one coil instead of three is needed for the same filter efficiency.

Different from DM filters, the CM filters employ relatively high inductance and low capacitance values. High inductances can be used due

to the characteristics of CM chokes, which employ high permeability materials, thus achieving high impedances with limited amount of magnetic material.

The total capacitance $C_{CM,total} = \sum C_{CM,i}$ with $i = 1,2$ between any of the input phases and the PE is restrained by the maximum allowable earth leakage current $I_{GND,rms}$ due to safety regulations. According to these regulations for IT equipment [86] – which also apply for semiconductor equipment – the amplitude of the current with mains frequency that flows through the CM capacitances towards PE at 110% mains voltage is limited to

$$I_{GND,rms} \leq 3.5 \text{ mA.} \quad (6.6)$$

With

$$I_{GND,rms} = 1.1 U_{N,rms} 2\pi f_N C_{CM,total} \quad (6.7)$$

the total capacitance results in

$$C_{CM,total} \leq 44 \text{ nF.} \quad (6.8)$$

For the design of the filter stage, this value has to be considered. Due to the high broadband noise level caused by the multi-phase motor connection, a high inductance with a large damping over the whole frequency range is preferred. For this reason, a one stage common mode filter is chosen for this design.

As mentioned earlier on, the filter components are placed in the dc-link in order to reduce the number of components needed. In a single stage filter, each phase possesses one capacitor towards PE. Thus, with 6.8 the following equation applies

$$C_{CM,1} + C_{CM,2} = 44 \text{ nF.} \quad (6.9)$$

This allows it to select the norm value of 22 nF for each CM capacitor.

$$C_{CM,1} = C_{CM,2} = 22 \text{ nF.} \quad (6.10)$$

With the capacitor values selected, the next step is the determination

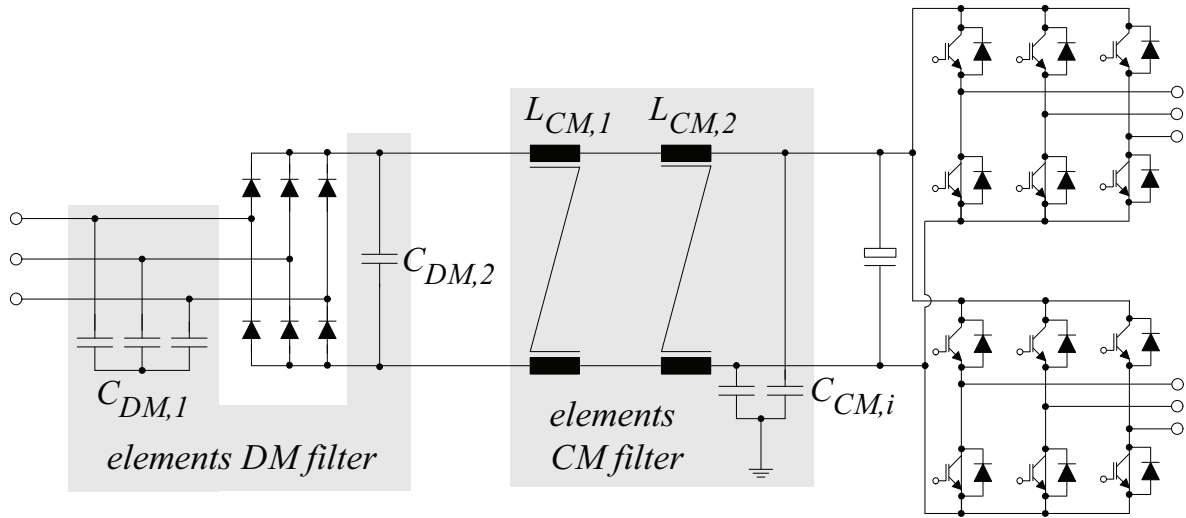


Figure 6.10: Circuit structure of the interleaved half-bridge converter including the designed filter components with $L_{CM,i} = 12$ mH, $C_{CM,i} = 22$ nF, $C_{DM,i} = 470$ nF.

of the inductors. At 150 kHz the required attenuation gained by simulation is -42 dB in order to fulfill Class A requirements (cf. Fig. 6.11). As mentioned in the introduction of this Thesis, the length of the power cable for the connection of the power electronics and the converter is expected to increase over the next years. Thus, a safety margin is provided in the design of the CM filter stage in order to provide enough margin for cable lengths of 20 m. For this, an additional attenuation of 10 dB is included in the design of the CM-inductor. With this, the required attenuation at 150 kHz is - 52 dB. This results in a relatively high inductance value of 20 mH. Thus, two CM inductors $L_{CM,1} = L_{CM,2} = 10$ mH are placed in series that built the CM stage along with the capacitors $C_{CM,1} = C_{CM,2}$.

Care must also be taken of a symmetrical placement of the components. Saturation of the cores has to be avoided. When choosing the core material, the following considerations must be applied. The permeability should not change with temperature. Furthermore, the insertion loss over the temperature is desired to be as broadband as possible. At low frequencies, a high permeability and thus a high damping is desirable. By that, the number of turn that are necessary for a given damping can be kept low. Lower winding capacitances are also achieved in this way. This circumstance then facilitates a better high-frequency behavior. Due to these considerations and the resulting compact volume the nanocrys-

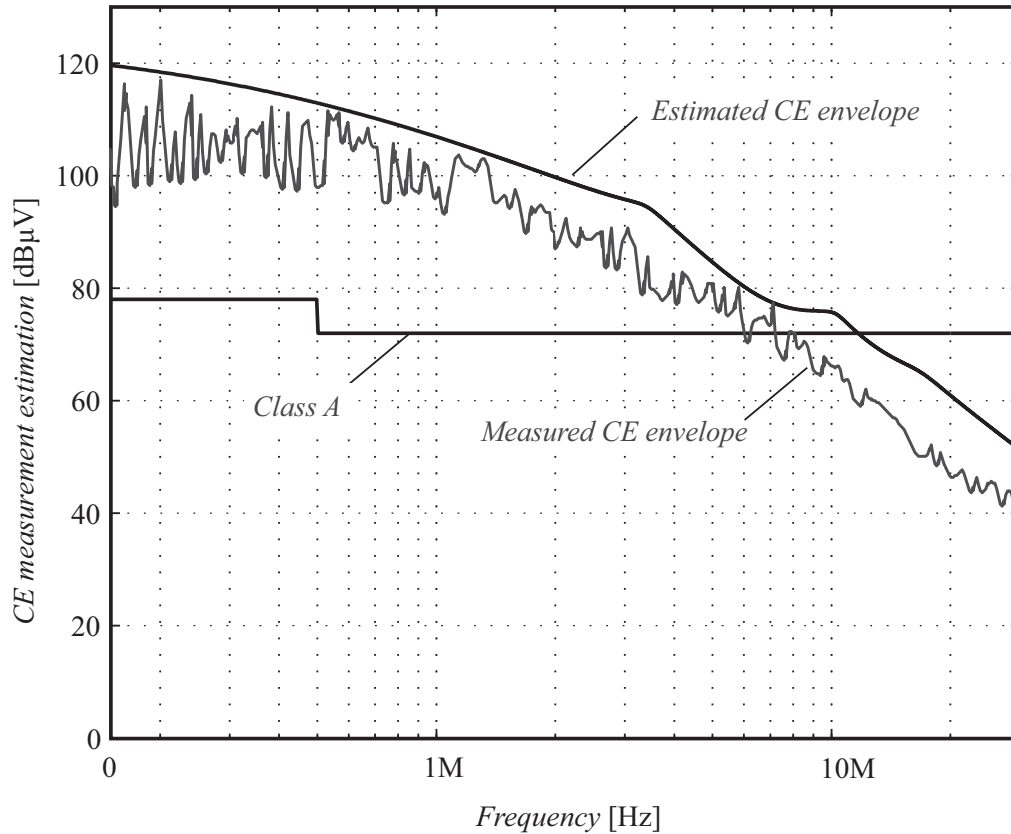


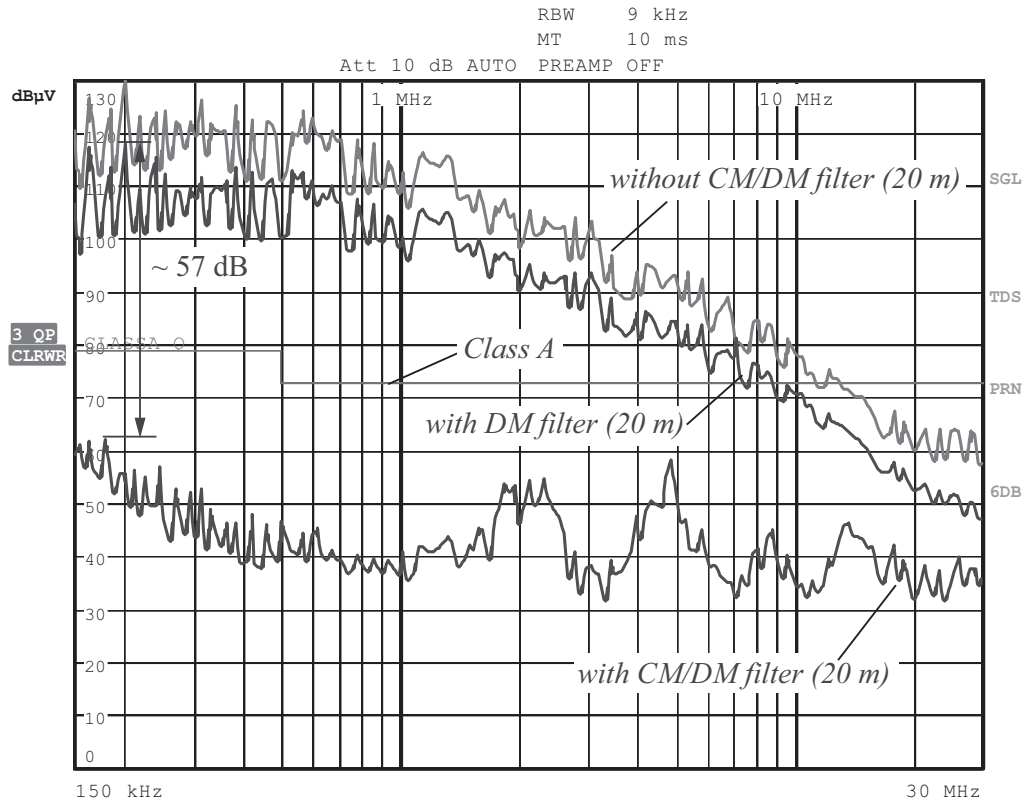
Figure 6.11: EM Emission levels at three-phase LISN. Depicted are the measured and predicted ones for a QP measurement as per CISPR 22.

talline core material VITROPERM 500F [87] is chosen. With this, the filter inductors are built as specified in Table 6.1, which also presents the specifications for the capacitors in the CM filter. Passive damping through resistors is not added due to the predominantly high frequency behaviour of the inductors.

The verification of the designed input filter shown in Fig. 6.10 connected to the three-phase mains is shown in Fig. 6.12 for drive currents of $I_{D,i} = 7.6$ Arms and bearing currents of $I_{B,i} = 1.2$ Arms and a cable length of 20 m.

Component	Parameter
$C_{DM,1}, C_{DM,2}$	X2 Capacitor, Evox Rifa PHE840M 470 nF – 250 Vac
$C_{CM,1}, C_{CM,2}$	Y2 Capacitor, Epcos MKP B81122 22 nF – 250 Vac
$L_{CM,1}, L_{CM,2}$	Vacuumschmelze VAC VITROPERM 500F W424 N = 2 x 26 turns, AWG17

Table 6.1: Selected components of the input filter.



Comment:
Date: 19.AUG.2008 13:49:10

Figure 6.12: Verification of the designed filter with a motor cable length of 20 m and drive currents of $I_{D,i} = 7.6$ Arms and bearing currents of $I_{B,i} = 1.2$ Arms.

Chapter 7

Realisation and Results

7.1 Power Electronics

The bearingless slice motor controller realised in this work comprises of a power board that contains the power electronics part with a rated power of 2 kW and the digital control board where the digital signal processing part of the system is located. Furthermore, this part also contains an auxiliary power supply that provides the demanded low voltage levels for the system. The whole converter system is depicted in Fig. 7.1. The outer dimensions are 200 x 95 x 135 mm which results in a volume of 2.565 dm³. With this, a power density of 0.78kW/l is achieved. Comparing this power density with the current state-of-the-art bearingless slice motor controller with a rated power of 1.5 kW and a power density of 0.34 kW/l [88] reveals that the power density is increased by 129% when a three-phase-topology is chosen as presented in this work.

7.1.1 DSP Board

All the control routines necessary for the operation of the bearingless pump system are implemented on a digital signal processor (DSP) of the type TMS320F2811 [89] from Texas Instruments. The analog digital converter of this device is used to read in the output values of the current sensors on the power board as well as the position sensors of

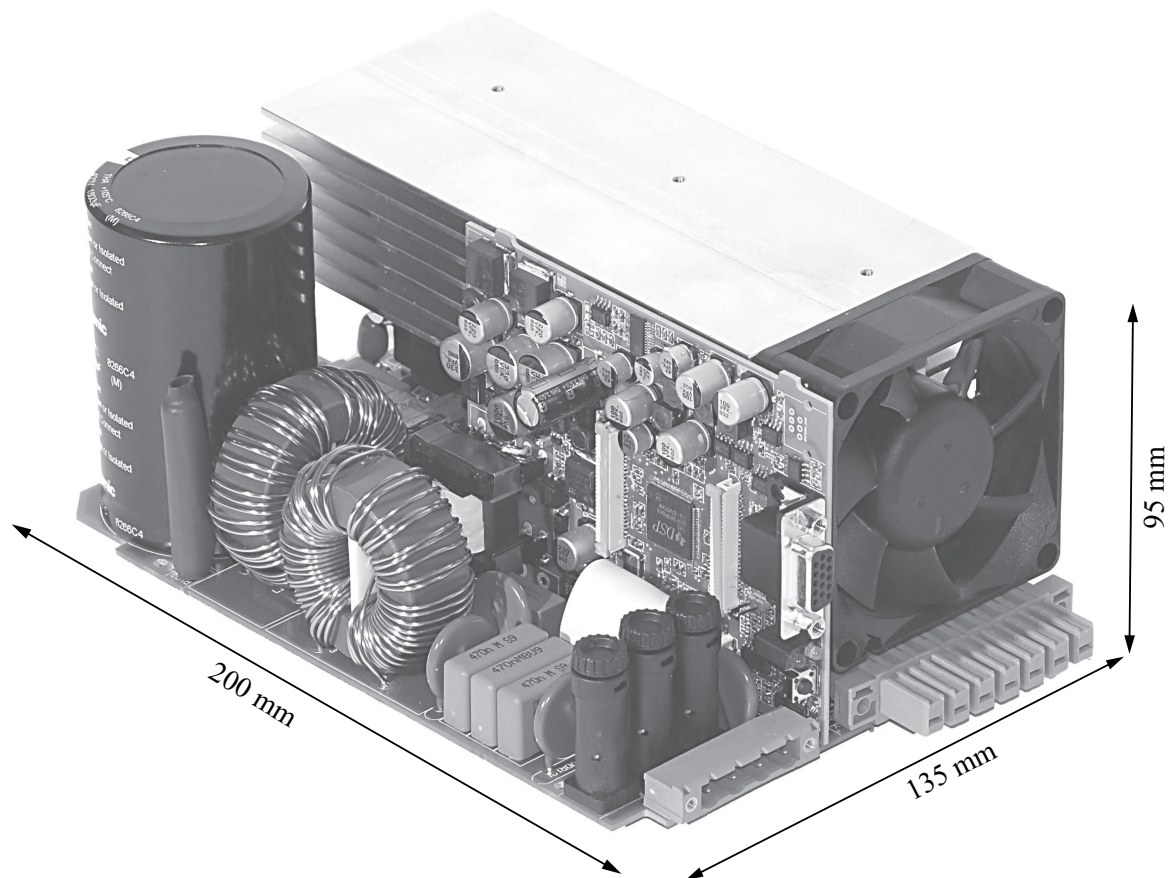


Figure 7.1: 2 kW bearingless slice motor controller.

the bearingless slice motor. All the necessary supply voltages of the controller, namely +15 V, +12 V and +5 V are generated with an auxiliary power supply which is located on the same board as the DSP. The output power levels of the respective voltages are listed in Table 7.1. A Flyback converter topology has been chosen for the realisation of this auxiliary power supply. The control is carried out with an integrated power MOSFET TOP243G [90]. The board is directly supplied by the dc-link voltage of the power stage.

7.1.2 Power Stage

In chapter 2, the necessity for a universally applicable power stage for bearingless pump systems is outlined. Considering the therein described application areas and based on the requirements for the power electronics derived in chapter 2.1 the power stage shown in Fig. 7.1 has been realised

Output voltage	Rated power
+5V	2.5 W
+12V	10 W
+15V	11 W

Table 7.1: Summary of output voltages and output power of the auxiliary power supply.

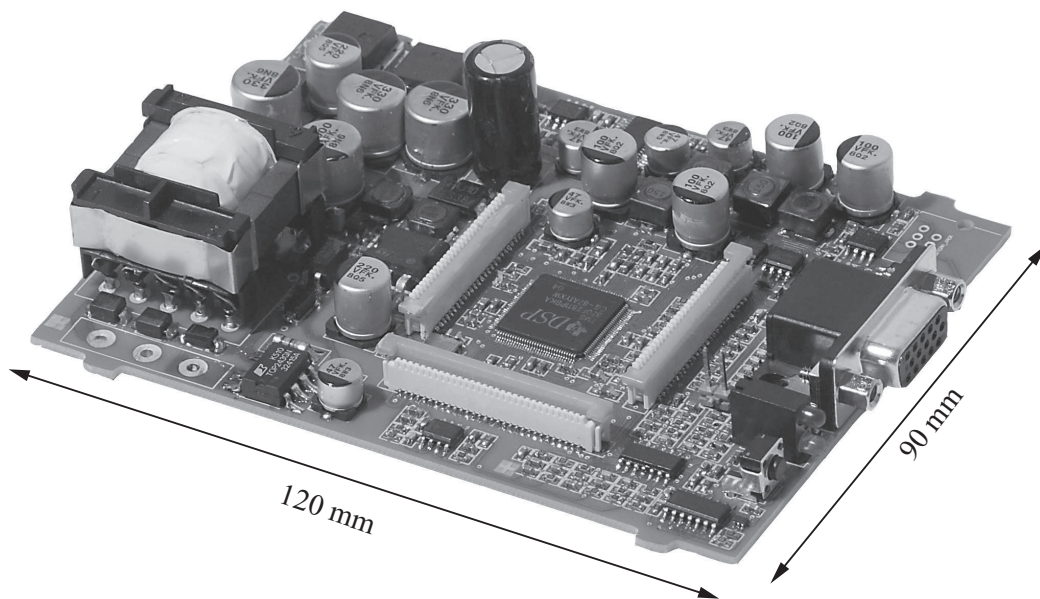


Figure 7.2: Digital signal processor board with an integrated Flyback converter.

by utilising the components specified in the previous chapters. The input filter stage derived in chapter is also integrated on this board, which is realised with a four layer PCB.

7.1.3 Efficiency

In a system that is composed of several components with strongly varying efficiencies over the operating range the overall efficiency is dominated by the weakest link in the chain. Meaning the component with the low-

est efficiency. This is very much the case in a bearingless pump system, where the hydraulic pump dominates the overall efficiency. According to manufacturers data [48], the hydraulic efficiency varies from 19% to 55% depending on the operating point of the pump as well as the media to be pumped. Thus, the efficiency of the power electronics has only a minor impact on the overall system efficiency. Contrary to power electronics converters in information technology, the solar industry or automotive applications where efficiencies above 95% are achieved a detailed analysis of the losses arising not only in the passive but also in the active components is mandatory for an exact definition of the system efficiency this is not of highest priority in a bearingless pump system. In these systems, the calculation of the losses arising in the power semiconductors give a good indication of the efficiency of the controller.

7.1.4 Verification of Modulation Methods

The modulation schemes that are derived in chapter 4 have been implemented on the DSP and tested with the laboratory prototype shown in Fig. 7.1. As an example, in Fig. 7.3 the current and voltage waveforms in the drive system generated by the modulation schemes CCM and TQM are presented. The measured shapes of the drive currents i_{D1} and i_{D2} are in good agreement with the simulation results presented in chapter 4.

Furthermore, tests with a bearingless pump system under load have been carried out in order to show the resulting maximum torque limits of the different modulation schemes. As an example, the result for the THM method is presented in Fig. 7.4. This allows it to rotate the impeller with a speed of 8500rpm while regulating the flow to 38 l/min. The resulting output pressure at this operating point is 4.5 bar. The current i_{B1} in the bearing phase L_{B1} , the drive current i_{D1} , the common bridge leg current i_{D0} , as well as the switched voltage u_{D1} across the drive coil L_{D1} are shown in the aforesaid figure. As can be seen, the bearing current i_{B1} which is controlled with CCM is relatively small compared to the drive current i_{D1} . The stable operation of the pump implies that the CCM method is sufficient to control the bearing currents. Not only in this operating point but even more over the whole operating range of the pump the CCM method still ensures a sufficient performance, while for the control of the drive system for higher power and/or rotation speeds

the presented more advanced modulation techniques have to be employed as discussed in chapter 4. The shown operating point in Fig. 7.4 could not be achieved by the CCM (see section 4.2) or SCM (see section 4.3) method.

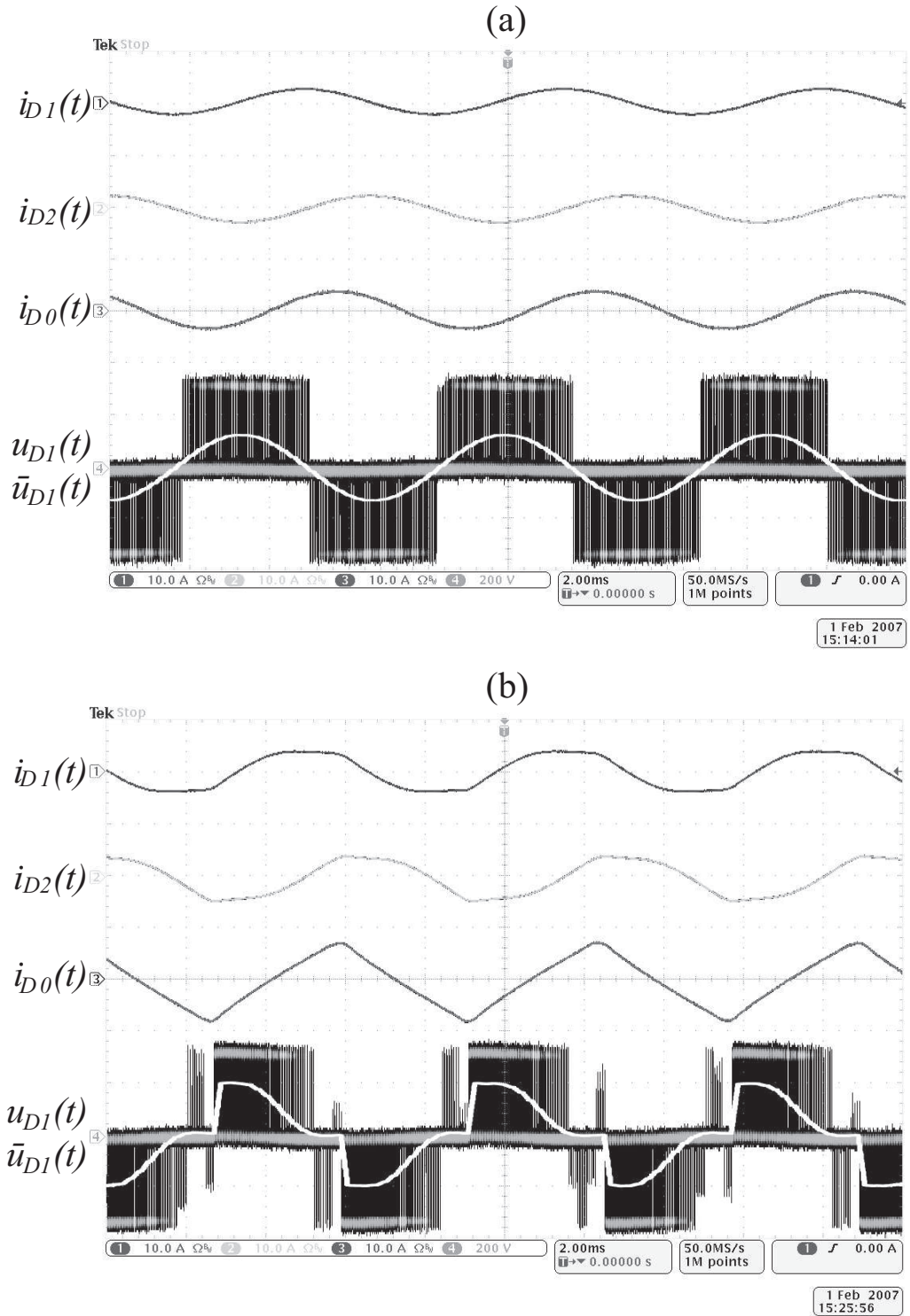


Figure 7.3: Experimental results of the modulation schemes presented in chapter 4. (a) CCM (b) TQM. Time behavior of drive currents i_{D1} and i_{D2} , common bridge leg current i_{D0} , switched voltage u_{D1} and average voltage $\bar{u}_{D1}(t)$ of drive coil L_{D1} . Current scales: i_{D0} , i_{D1} , i_{D2} : 10 A/div, voltage scale: U_{D1} : 200 V/div, time scale: 2 ms/div.

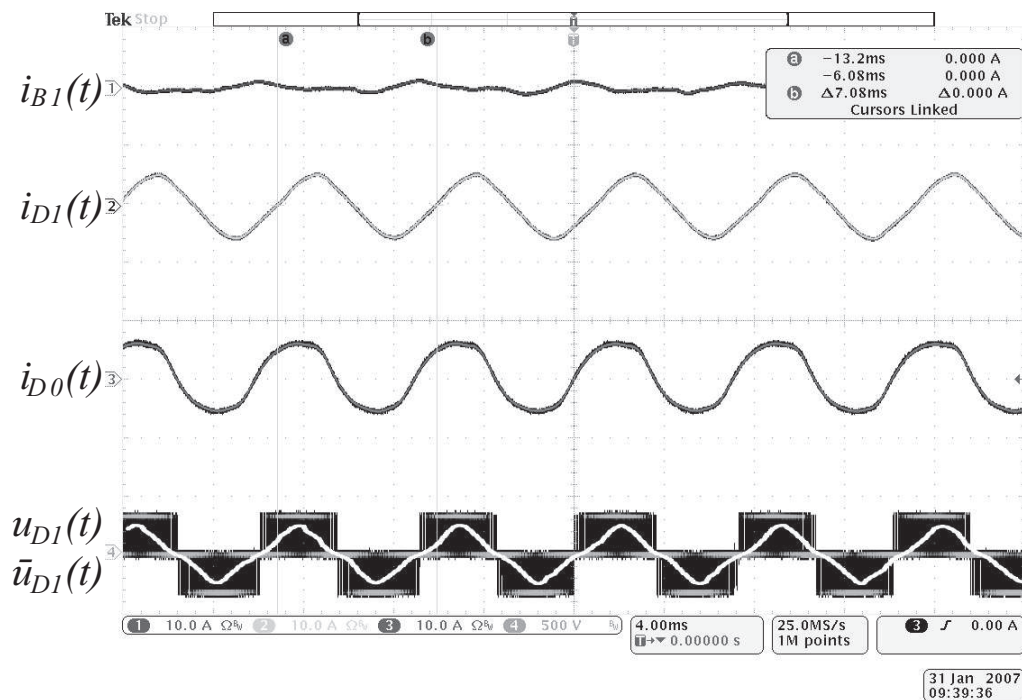


Figure 7.4: Experimental results for the pump under operation employing the THM method with an impeller speed of 8500 rpm, a flow of 38.5 l/min and resulting pressure of 4.5 bar. Time behavior of the bearing current i_{B1} , the drive current i_{D1} , the common bridge leg current i_{D0} , the switched voltage u_{D1} and the average voltage $\bar{u}_{D1}(t)$ of drive coil L_{D1} . Current scales: i_{D0} , i_{D1} , i_{D2} : 10 A/div, voltage scale: U_{D1} : 500 V/div, time scale: 4 ms/div.

Conclusion

In this work, the applicability of three-phase power modules for the control of a two-phase bearingless slice motor has been shown based on the background of reducing the overall cost of a bearingless slice motor pump system. All aspects necessary for the realisation of such a system have been analysed in this work. After an evaluation of the best suitable topology with a reduced number of semiconductor components compared to the state-of-the-art control electronics for bearingless slice motor pumps, an analysis of the utilised three-phase power module has been carried out along with the dimensioning of the heat sink and the dc-link capacitor. As a result of this, the power density of the controller is increased by more than a factor of two compared to a state-of-the-art design.

The theoretical considerations regarding the control of the system due to delay times in the generation of the duty-cycles as well as delays in the current measurement are analysed and the necessary measures regarding the control are carried out. The modulation methods required for the operation of the two-phase motor have been developed so that a similar performance as with today's systems can be achieved with the novel concept. The herein developed control methods have been implemented on a digital signal processor board which has also been developed in this work.

A comparison of motor topologies suitable for future bearingless pump systems with other than a two-phase motor has led to the conclusion that applying a four-phase motor concept with concentrated coils is the preferable concept for low speed applications e.g. in mixers for biotechnology applications. Regarding high torque applications the two-phase motor concepts still seems to be the preferable solution. The three-phase

temple motor design has emerged as the system with minimal losses in power electronics and the motor. However, using this concept, the maximum torque given a certain motor size is lower as compared to the standard two-phase configuration.

Utilising power cables up to 20 m between the power electronics and the bearingless slice motors results in an increase of the common mode noise in the system. In order to obtain a minimum input filter, a common model of the two-phase bearingless slice motor pump system including the motor and electronics is presented. This model serves as the base for the volume optimised input filter.

Outlook

In the course of this work, the fundamental issues arising in the design of future bearingless slice motor pump systems have been investigated and based on this, a laboratory prototype has been realised which allows the verification of the theoretical results obtained in this work. This analysis has led to several points which have been identified as research topics for future works:

- As mentioned in section 2.3.2 the employment of integrated power modules that are available off-the-shelf has the disadvantage that the latest semiconductor technologies are not utilised for the fabrication of these modules which affects the efficiency of the system. Research could be carried out in the direction of realising a customised power module using latest semiconductor technology and thereby increasing the efficiency and compactness of the system.
- In order to decrease the size of the extruded aluminum heat sink, the manufacturing process of it could be further investigated in order to minimise the thickness of the aluminum sheets. Thereby, the volume of the cooling part could be further minimised.
- In applications where it is not mandatory that the power electronics is placed a long distance away from the pump since the necessary space is available or forced air cooling is allowed, the concept of a fully integrated bearingless pump should be investigated. This would greatly reduce the cabling effort and thus lower the input filter volume as well.
- The cabling effort of the analog sensor signals between the motor and the controller could be reduced if a digital signal processor

would be implemented in the motor itself. This allows it to compute the position of the impeller directly in the motor. The position values can then be transferred to the controller via a bus system which significantly reduces the number of signal wires.

- The analysis of the motor concepts in chapter 5 has shown that the bearingless slice motor in disc shape is a promising concept for low speed applications, such as for mixers in biotechnology applications. Based on the results obtained in that chapter, the realisation of such a mixer system could be further investigated in future works. Especially the influence of the stainless steel tanks on the position detection concept offers great potential for further investigations.

Bibliography

- [1] J. Bichsel, “Beiträge zum lagerlosen Elektromotor,” Ph.D. dissertation, ETH Zurich, Zurich, 1990.
- [2] N. Barletta, “Der lagerlose Scheibenläufer,” Ph.D. dissertation, ETH Zurich, Zurich, 1998.
- [3] K. Raggl, T. Nussbaumer, and J. W. Kolar, “Comparison of winding concepts for bearingless pumps,” in *Proceedings of International Conference on Power Electronics (ICPE '07)*, 2007, pp. 1013–1020.
- [4] R. Schöb, “Beiträge zur lagerlosen Asynchronmaschine,” Ph.D. dissertation, ETH Zurich, Zurich, 1993.
- [5] C. Hüttner, “Regelungskonzepte magnetisch gelagerter Scheibenmotoren,” Ph.D. dissertation, ETH Zurich, Zurich, 2003.
- [6] T. Gempp, “Mechatronik einer lagerlosen Spaltrohrpumpe,” Ph.D. dissertation, ETH Zurich, Zurich, 1997.
- [7] P. Bösch, “Lagerlose Scheibenläufermotoren höherer Leistung,” Ph.D. dissertation, ETH Zurich, Zurich, 2004.
- [8] J. Zhang, “Power Amplifier for Active Magnetic Bearings,” Ph.D. dissertation, ETH Zurich, Zurich, 1995.
- [9] N. Mohan, T. Undeland, and W. Robbins, *Power Electronics: Converters, Applications and Design*. New York, USA: Wiley, 2003.
- [10] G. Schweitzer, H. Bleuler, and A. Traxler, *Active Magnetic Bearings*. Zurich, Switzerland: vdf Hochschulverlag ETH Zurich, 1994.

BIBLIOGRAPHY

- [11] S. M. Henderson, R. L. Perry, and J. H. Young, *Principles of Process Engineering*. St. Joseph, USA: American Society of Agricultural Engineers, 1997.
- [12] M. Neff, “Magnetgelagertes Pumpsystem für die Halbleiterfertigung,” Ph.D. dissertation, ETH Zurich, Zurich, 2003.
- [13] Chartered Semiconductor Manufacturing, “IBM, Chartered, Infineon and Samsung Announce Process and Design Readiness for Silicon Circuits on 45nm Low-Power Technology,” *Press release*, 29th August 2006.
- [14] Intel, “Intel Demonstrates Industry’s First 32nm Chip and Next-Generation Nehalem Microprocessor Architecture,” *Intel Developer Forum*, San Francisco, 18th September 2007.
- [15] L. M. C. Mhango and G. K. Creighton, “Novel Two-Phase Inverter Fed Induction-Motor Drive,” in *IEE Proceedings of Electric Power Applications*, vol. 131, no. 3, 1984, pp. 99–104.
- [16] I. R. Smith, G. Creighton, and L. M. C. Mhango, “Analysis and Performance of a Novel Two-Phase Drive for Fan and Water-Pumping Applications,” *IEEE Transactions on Industrial Electronics*, vol. 36, no. 4, pp. 530–538, 1989.
- [17] F. Blaabjerg, F. Lungeanu, K. Skaug, and M. Tonnes, “Evaluation of Low-Cost Topologies for Two Phase Induction Motor Drives in Industrial Applications,” in *Proceedings of IEEE Industry Applications Society Annual Meeting (IAS '02)*, vol. 4, 2002, pp. 2358–2365.
- [18] D. C. Lee and Y. S. Kim, “Control of Single-Phase-to-Three-Phase AC/DC/AC PWM Converters for Induction Motor Drives,” *IEEE Transactions on Industrial Electronics*, vol. 54, no. 2, pp. 797–804, 2007.
- [19] M. B. de Rossiter Correa, C. B. Jacobina, A. M. N. Lima, and E. R. C. da Silva, “A Three-Leg Voltage Source Inverter for Two-Phase AC Motor Drive Systems,” *IEEE Transactions on Power Electronics*, vol. 17, no. 4, pp. 517–523, 2002.

- [20] D.-H. Jang and J.-S. Won, "Voltage, Frequency and Phase-Difference Angle Control of PWM Inverters-Fed Two-Phase Induction Motors," *IEEE Transactions on Power Electronics*, vol. 9, pp. 377-383, 1994.
- [21] M. A. Jabbar, A. M. Khambadkone, and Y. Zhang, "Space-Vector Modulation in a Two-Phase Induction Motor Drive for Constant-Power Operation," *IEEE Transactions on Industrial Electronics*, vol. 51, no. 5, pp. 1081-1088, 2004.
- [22] H. Ertl, T. Wiesinger, J. W. Kolar, and F. C. Zach, "A Simple Active Method to Avoid the Balancing Losses of DC Link Capacitors," in *Proceedings of International Conference on Power Electronics (PCIM-PE '03)*, 2003.
- [23] B. Francois and A. Bouscayrol, "Design and Modelling of a Five-Phase Voltage-Source Inverter for Two Induction Motors," in *Proceedings of European Conference on Power Electronics and Applications (EPE '99)*, 1999, pp. CD-ROM paper 626.
- [24] C. B. Jacobina, O. I. da Silva, E. C. dos Santos, and A. M. N. Lima, "Reduced Switch Count Multi-Motor Drive Systems," in *Proceedings of IEEE International Electric Machines and Drives Conference (IEMDC '05)*, 2005, pp. 1858-1862.
- [25] C. B. Jacobina, M. B. de Rossiter Correa, A. M. N. Lima, and E. R. C. da Silva, "AC Motor Drive Systems with a Reduced-Switch-Count Converter," *IEEE Transactions on Industry Applications*, vol. 39, no. 5, pp. 1333-1342, 2003.
- [26] P. Delarue, A. Bouscayrol, and B. Francois, "Control Implementation of a Five-Leg Voltage-Source-Inverter Supplying Two Three-Phase Induction Machines," in *Proceedings of IEEE International Electric Machines and Drives Conference (IEMDC '03)*, vol. 3, 2003, pp. 1909-1915.
- [27] F. Blaabjerg, F. Lungeanu, K. Skaug, and M. Tonnes, "Two-Phase Induction Motor Drives," *IEEE Industry Applications Magazine*, vol. 10, no. 4, pp. 24-32, 2004.
- [28] C. B. Jacobina, E. C. dos Santos, E. R. C. da Silva and M. B. de Correa, A. M. N. Lima, and T. M. Oliveira, "Reduced Switch Count

- Multiple Three-Phase AC Machine Drive Systems,” *IEEE Transactions on Power Electronics*, vol. 23, no. 2, pp. 966–976, 2008.
- [29] D. G. Holmes and A. Kotsopoulos, “Variable Speed Control of Single and Two Phase Induction Motors Using a Three Phase Voltage Source Inverter,” in *Proceedings of IEEE Industry Applications Society Annual Meeting (IAS '93)*, 1993, pp. 613–620.
- [30] C.-M. Young, C.-C. Liu, and C.-H. Liu, “New Inverter Driven Design and Control Method for Two-Phase Induction Motor Drives,” in *Proceedings of IEEE Institute of Electrical and Electronics Engineers*, vol. 143, no. 6, 1996, pp. 458–466.
- [31] J. Jones, D. Dujicand, E. Levi, A. Batako, and O. Mgaloblishvili, “A novel five-leg inverter pwm technique for two-motor centre-driven winders,” in *Proceedings of IEEE International Electric Machines and Drives Conference (IEMDC '07)*, vol. 1, 2007, pp. 254–259.
- [32] International Rectifier: IRGP20B60KD-E, Preliminary Datasheet (2008), URL: <http://www.irf.com>.
- [33] J. W. Kolar, H. Ertl, and F. C. Zach, “A Comprehensive Design Approach for a Three-Phase High-Frequency Single-Switch Discontinuous-Mode Boost Power Factor Corrector Based on Analytically Derived Normalized Converter Component Ratings,” *IEEE Transactions on Industry Applications*, vol. 31, no. 3, pp. 569–582, 1995.
- [34] T. Schneeberger and J. W. Kolar, “Novel integrated bearingless hollow-shaft drive,” in *Proceedings of IEEE Industry Applications Society Annual Meeting (IAS '06)*, vol. 1, 2006, pp. 70–75.
- [35] International Rectifier: Integrated Hybrid IC IRAM136-3063B, Datasheet (2008), URL: <http://www.irf.com>.
- [36] G. Laimer, “Ultrakompaktes 10kW 500kHz Dreiphasen-Pulsgleichrichtermodul,” Ph.D. dissertation, ETH Zurich, Zurich, 2005.
- [37] T. Nussbaumer, “Netzrückwirkungsarmes Dreiphasen-Pulsgleichrichtersystem mit weitem Eingangsspannungsbereich,” Ph.D. dissertation, ETH Zurich, Zurich, 2004.

- [38] D. J. de Kock and J. A. Visser, “Trade-off Design of Extruded Heat Sinks Using Mathematical Optimization,” *Journal of Electronic Packaging*.
- [39] J. A. Visser, D. J. de Kock, and F. D. Conradie, “Minimisation of heat sink mass using mathematical optimisation,” in *Proceedings of IEEE Semiconductor Thermal Measurement and Management Symposium (SEMI-THERM '00)*, 2000, pp. 252–259.
- [40] DELTA GROUP: <http://www.deltaww.com>.
- [41] U. Drofenik and J. W. Kolar, “Sub-Optimum Design of a Forced Air Cooled Heat Sink for Simple Manufacturing,” in *Proceedings of IEEE Power Conversion Conference (PCC '07)*, 2007, pp. 1189–1194.
- [42] ANSYS Icepak, URL: <http://www.ansys.com>.
- [43] SEMI, *Specification for Semiconductor Processing Equipment Voltage Sag Immunity – SEMI F47-0200*. San Jose, CA, USA: URL: <http://www.semi.org>, 2000.
- [44] C. Xiao, L. Zhao, T. Asada, W. G. Odendaal, and J. D. van Wyk, “An overview of integratable current sensor technologies,” in *Proceedings of IEEE Industry Applications Society Annual Meeting (IAS '03)*, vol. 2, 2003, pp. 1251–1258.
- [45] R. S. Popovic, “Hall devices for magnetic sensor microsystems,” in *Proceedings of International Conference on Solid State Sensors and Actuators (TRANSDUCERS '97)*, vol. 1, 1997, pp. 377–380.
- [46] Allegro Current Sensor ACS712, URL: <http://www.allegromicro.com>.
- [47] C. F. Golub, G. H. Van Loan, *Matrix Computations*. Baltimore, USA: John Hopkins University Press, 1996.
- [48] Levitronix BPS4 bearingless pump system: <http://www.levitronix.com>.
- [49] P. Karutz, T. Nussbaumer, W. Gruber, and J. W. Kolar, “Novel Magnetically Levitated 2-Level Motor,” *IEEE Transactions on Mechatronics*, vol. 13, pp. 658–668, 2008.

- [50] T. Nussbaumer, M. L. Heldwein, G. Guanghai, S. D. Round, and J. W. Kolar, “Comparison of prediction techniques to compensate time delays caused by digital control of a three-phase buck-type pwm rectifier system.”
- [51] A. Weinemann, *Regelungen I. Analyse und technischer Entwurf*. Wien, Austria: Springer, 1998.
- [52] R. Fischer, *Elektrische Maschinen*. Berlin, Deutschland: Verlag Technik, 2001.
- [53] M. J. Meco-Gutierrez, F. Perez-Hidalgo, F. Vargas-Merino, and J. R. Heredia-Larrubia, “Pulse Width Modulation Technique with Harmonic Injection and Frequency Modulated Carrier: Formulation and Application to an Induction Motor,” *IET Electric Power Applications*, vol. 1, no. 5, pp. 714–726, 2007.
- [54] S. R. Bowes and D. Holliday, “Comparison of Pulse-Width-Modulation Control Strategies for Three-Phase Inverter Systems,” vol. 153, no. 4, 2006, pp. 575–584.
- [55] S. R. Bowes, D. Holliday, and S. Grewal, “Comparison of Single-Phase Three-Level Pulse Width Modulation Strategies,” vol. 151, no. 2, 2004, pp. 205–214.
- [56] K. C. Wilson, *Slurry Transport Using Centrifugal Pumps*. New York, USA: Springer, 1996.
- [57] I. J. Karassik, *Pump Handbook*, 3rd ed. McGraw-Hill, 2000.
- [58] B. K. Gandhi, “Effect of Speed on the Performance Characteristics of a Centrifugal Slurry Pump,” in *Journal of Hydraulic Engineering*, vol. 128, 2002, pp. 225–233.
- [59] C. Pfeiderer and H. Petermann, *Strömungsmaschinen*. Berlin: Springer, 1996.
- [60] *Sulzer Pumps, Sulzer Centrifugal Pump Handbook*. Oxford, UK: Elsevier Advanced Technology, 1998.
- [61] S. Silber, “Beiträge zum lagerlosen Einphasenmotor,” Ph.D. dissertation, Johannes Kepler Universität, Linz, 2000.

- [62] S. Silber, W. Amrhein, P. Bosch, R. Schob, and N. Barletta, "Design aspects of bearingless slice motors," *IEEE Transactions on Mechatronics*, vol. 10, no. 6, pp. 611–617, 2005.
- [63] D. Schröder, *Elektrische Antriebe – Grundlagen*. Berlin, Germany: Springer, 2000.
- [64] K. Simonyi, *Theoretische Elektrotechnik*. Leipzig, Germany: Barth Verlagsgesellschaft GmbH, 1993.
- [65] Maxwell 3D, URL: <http://www.ansoft.com>.
- [66] W. Baran, *Magnetische Kreise und ihre Berechnung, Feinwerktechnik & Messtechnik*. Munich, Germany: Carl Hanser Verlag, 1989.
- [67] C. P. Steinmetz, "On the Law of Hysteresis," in *Proceedings of IEEE*, vol. 72, 1984, pp. 196–221.
- [68] R. Q. P. Kallenbach, E. Eick, *Elektromagnete: Grundlagen, Berechnung, Konstruktion, Anwendung*. Stuttgart, Germany: B.G. Teubner, 1996.
- [69] M. Barnes and C. Pollock, "Power electronic converters for switched reluctance drives," *IEEE Transactions on Power Electronics*, vol. 13, no. 6, pp. 1100–1111, 1998.
- [70] T. Miller, *Switched Reluctance Motors and Their Control*. Oxford, UK: Magna Physics/Clarendon, 1993.
- [71] K. Vogt, *Elektrische Maschinen: Berechnung rotierender elektrischer Maschinen*. Berlin, Germany: Verlag Technik, 1988.
- [72] T. Williams, *EMC for Product Engineers*. Oxford, UK: Newnes, 2001.
- [73] B. R. Archambeault, *PCB Design for Real-World EMI Control*. Massachusetts, USA: Kluwer Academic Publishers, 2002.
- [74] F. Lin and D. Y. Chen, "Reduction of Power Supply EMI Emission by Switching Frequency Modulation," *IEEE Transactions on Power Electronics*, vol. 9, no. 1, pp. 132–137, Jan. 1994.

- [75] A. M. Stankovic. and H. Lev-Ari, “Randomized Modulation in Power Electronic Converters,” *Proceedings of IEEE*, vol. 90, no. 5, pp. 782–799, 2002.
- [76] A. M. Trzynadlowski, F. Blaabjerg, J. K. Pedersen, R. L. Kirlin, and S. Legowski, “Random Pulse Width Modulation Techniques for Converter–Fed Drive Systems – a Review,” *IEEE Transactions on Industry Applications*, vol. 30, no. 5, pp. 1166–1175, 1994.
- [77] A. Nagel, “Leitungsgebundene Störungen in der Leistungselektronik: Entstehung, Ausbreitung und Filterung.” Ph.D. dissertation, RWTH Aachen, Aachen, 1999.
- [78] M. L. Heldwein, “EMC Filtering of Three-Phase PWM Converters,” Ph.D. dissertation, ETH Zürich, Zürich, 2008.
- [79] E. Zhong and T. A. Lipo, “Improvements in EMC Performance of Inverter–Fed Motor Drives,” *IEEE Transactions on Industry Applications*, vol. 31, no. 6, pp. 1247–1256, 1995.
- [80] C. D. Mercier and D. A. Cooper, “Selection of Power Cables for PWM AC Adjustable–Speed Drives,” in *Proceedings of IEEE Annual Textile, Fiber and Film Industry Technical Conference (TEXCON '99)*, 1999, pp. pp. 1–7.
- [81] J. M. Bentley and P. J. Link, “Evaluation of Motor Power Cables for PWM AC Drives,” *IEEE Transactions on Industry Applications*, vol. 33, no. 2, pp. 342–358, 1997.
- [82] J. Ahola, T. Lindh, and J. Partanen, “Simulation Model for Input Impedance of Low Voltage Electric Motor at Frequency Band 10 kHz – 30 MHz,” in *Proceedings of IEEE International Electric Machines and Drives Conference (IEMDC '03)*, vol. 2, June 2003, pp. 1127–1132.
- [83] M. Schinkel, S. Weber, S. Guttowski, W. John, and H. Reichl, “Efficient HF Modeling and Model Parameterization of Induction Machines for Time and Frequency Domain Simulations,” in *Proceedings of IEEE Applied Power Electronics Conference and Exposition (APEC '06)*, 2006, pp. pp. 1181–1186.

- [84] A. Boglietti and E. Carpaneto, “An Accurate High Frequency Model of AC PWM Drive Systems for EMC Analysis,” in *Proceedings of IEEE Industry Applications Society Annual Meeting (IAS '01)*, vol. 2, 2001, pp. 1111–1117.
- [85] S. Ogasawara and H. Akagi, “Modeling and Damping of High-Frequency Leakage Currents in PWM Inverter-Fed AC Motor Drive Systems,” *IEEE Transactions on Industry Applications*, vol. 32, no. 5, pp. 1105–1114, 1996.
- [86] IEC, *Safety of Information Technology Equipment – IEC 60950*. Brussels, Belgium: International Electrotechnical Commission – IEC, 1999.
- [87] Vacuumschmelze VITROPERM 500F, URL: <http://www.vacuumschmelze.com>.
- [88] Levitronix pump controller LC325, URL: <http://www.levitronix.com>.
- [89] Texas Instruments Digital Signal Processor TMS320F2811, URL: <http://www.texasinstruments.com>.
- [90] Power Integrations TOP243G, Datasheet 2008, URL: www.powerint.com.

BIBLIOGRAPHY

Vita

Name	Martin Thomas Bartholet
Date of birth	26. January 1978
Place of birth	Uznach, SG (Switzerland)
Citizen of	Flums, SG (Switzerland)
Marital state	unmarried
Father	Josef Linus Bartholet
Mother	Maria Agnes Bartholet née Lehmann
Education	1985—1991 Primary School (Primarschule), Eschenbach, SG 1991—1993 Secondary School (Sekundarschule), Eschenbach, SG 1993—1998 Gymnasium in natural sciences (Kantonsschule Typus C), Wattwil, SG
University	1998—2004 M. Sc. in Electrical Engineering, ETH Zurich 2004 Master Theses at Chalmers University, Gothenburg, Sweden
Doctorate	2005—2008 Doctoral studies at the Power Electronic Systems Laboratory (PES), ETH Zurich